UNIVERSITEIT VAN PRETORIA
UNIVERSITY OF PRETORIA
YUNIBESITHI YA PRETORIA

CORROSION FATIGUE BEHAVIOUR OF 5083-H111 AND 6061-T651 ALUMINIUM ALLOY WELDS

by

Faustin Kalenda Mutombo

Submitted in partial fulfilment of the requirements for the degree

MSc (Applied Science) (Metallurgy)

in the Faculty of Engineering, Built Environment and Information Technology, University of Pretoria

April 2011

ACKNOWLEDGEMENTS

My sincere thanks to the Light Metals Development Network and the THRIP programme for financial support during this investigation and to the Aluminium Federation of South Africa (AFSA) and Dr Tony Paterson for technical assistance and guidance.

I would also like to express my appreciation to my supervisor, Professor Madeleine du Toit, for her support, guidance and comments during the course of this project. The contributions and technical advice of Professor Waldo Stumpf and Professor Chris Pistorius are also gratefully acknowledged.

Finally, the technical support of Willie Du Preez, Sagren Govender, Chris McDuling and Erich Guldenpfennig from the Council for Scientific and Industrial Research (CSIR) is gratefully acknowledged.

DEDICATION

This work is dedicated to

- the Lord Jesus Christ, the cornerstone of any major construction and source of all innovation,
- my wife, Mary Claire Kamuanga, for her spiritual and moral support, especially during difficult times,
- my children, Jesse, Greg and Bert Kalenda,
- my parents, and
- my brothers, sisters, friends and colleagues.

ABSTRACT

In addition to being one of the highest strength non-heat treatable aluminium alloys, magnesium-alloyed wrought aluminium 5083 displays excellent corrosion resistance and good weldability. Aluminium alloy 6061, alloyed with magnesium and silicon, displays high strength, excellent formability, adequate weldability and good corrosion resistance. These aluminium alloys find application in the ship building and transport industries where 5083 is often joined to 6061 to produce welded structures such as complex I-beams and semi-hollow or hollow channels. This project aimed at characterizing the hardness, tensile properties, corrosion behaviour and fatigue properties (in air and in a 3.5% NaCl solution) of aluminium 5083 and 6061 in the as-received and welded conditions. Plates of 5083-H111 and 6061-T651 aluminium, prepared with double-V or square butt joint preparations, were joined using semi-automatic or fully automatic pulsed gas metal arc welding (GMAW). The pulsed GMAW process allows close control over the welding arc and facilitates the use of lower average heat inputs, thereby improving the bead appearance and mechanical properties. During this investigation, three filler wires were evaluated, namely magnesium-alloyed ER5183 and ER5356 aluminium, and silicon-alloyed ER4043.

Hardness measurements revealed a decrease in hardness in the weld metal of the 5083-H111 welds. Dressed welds failed in the weld metal during transverse tensile testing, whereas undressed (as-welded) specimens failed at the weld toe or weld root due to the stress concentration introduced by the weld geometry. Significant softening, attributed to the partial dissolution and coarsening of strengthening precipitates and recrystallization during welding, was observed in the heat-affected zones of the 6061-T651 welds. During tensile testing, failure occurred in the heat-affected zone of all 6061 welds.

Welding reduced the room temperature fatigue life of all specimens tested. In the 5083 welds, fatigue cracks initiated preferentially at gas pores, lack-of-fusion type defects and second phase particles in dressed welds, and at the stress concentration presented by the weld toes or the weld root in undressed welds. In 6061 welds, failure occurred preferentially in the softened heat-affected zone of the welds. As a result of improved control over the weld profile and a lower incidence of weld defects, fully automatic welds consistently outperformed semi-automatic welds during fatigue testing. The presence of a corrosive environment (a 3.5% NaCl solution in this investigation) during fatigue testing reduced the fatigue properties of all the samples tested. Corrosion pits formed preferentially at second phase particles or weld defects, and reduced the overall fatigue life by accelerating fatigue crack initiation.

TABLE OF CONTENTS

LIST OF TABLES

LIST OF FIGURES

CHAPTER 1. INTRODUCTION

Aluminium and its alloys are widely used as engineering materials on account of their low density, high strength-to-weight ratios, excellent formability and good corrosion resistance in many environments. One of the major drawbacks of commercially pure aluminium is its low strength, but significant improvements in strength, hardness and wear resistance can be obtained through solid solution strengthening, cold work and precipitation hardening. This investigation focused on two popular wrought aluminium alloys, namely magnesium-alloyed 5083 (in the strain hardened -H111 temper state) and 6061, alloyed with magnesium and silicon (in the precipitation hardened -T651 temper condition).

Alloy 5083 is one of the highest strength non-heat treatable aluminium alloys, with excellent corrosion resistance, good weldability and reduced sensitivity to hot cracking when welded with near-matching magnesium-alloyed filler metal. This alloy finds applications in ship building, automobile and aircraft structures, tank containers, unfired welded pressure vessels, cryogenic applications, transmission towers, drilling rigs, transportation equipment, missile components and armour plate. Alloy 6061 combines medium strength levels with excellent formability, moderate weldability, good machinability and average corrosion resistance. It is widely used in road and rail transport for truck bodies, bridge railings, rail cars and tank containers, as well as in canoes, towers, furniture, pipelines and various structural applications. Both aluminium alloys find widespread application in ship building, architectural structures and transport equipment, where alloy 5083 is often joined to 6061 to produce welded structures such as complex I-beams and semi-hollow or hollow channels. In many of these applications the aluminium structures are exposed to aqueous environments throughout their lifetimes.

The fatigue properties of welded aluminium structures under dynamic loading conditions have been studied extensively. Welding is known to create tensile residual stresses, to promote grain growth, recrystallization and softening in the heat-affected zone, and to introduce weld defects that act as stress concentrations and preferential fatigue crack initiation sites. Several fatigue studies of aluminium welds emphasised the role of precipitates, second phase particles and inclusions in initiating fatigue cracks. When simultaneously subjected to a corrosive environment and dynamic loading, the fatigue properties are often adversely affected and even alloys with good corrosion resistance may fail prematurely under conditions promoting fatigue failure.

The good corrosion resistance of the aluminium alloys studied in this investigation is attributed to the spontaneous formation of a thin, compact and adherent aluminium oxide film on the surface on exposure to water or air. This hydrated aluminium oxide layer may, however, dissolve in some chemical solutions (such as strong acids or alkaline solutions), leading to rapid corrosion. Damage to the passive layer in chloride-containing environments (such as sea water or NaCl solutions) may result in localized corrosive attack such as pitting corrosion. Pitting is the most commonly observed form of corrosion in aluminium and its alloys. The presence of corrosion pits affects the fatigue properties of the aluminium alloys by creating sharp surface stress concentrations which promote fatigue crack initiation. In welded structures, pits are often associated with coarse second phase particles or welding defects. Inclusions or precipitates may promote the dissolution of the adjacent aluminium matrix through galvanic interactions.

A review of available literature on the corrosion fatigue properties of aluminium 5083 and 6061 welds revealed limited information. Although the mechanical properties, corrosion behaviour and fatigue properties of these alloys have been studied in depth, the influence of filler wire composition and weld geometry on the fatigue behaviour of fully automatic and semi-automatic welds, and the behaviour of similar and dissimilar metal joints when simultaneously subjected to a chloride-containing corrosive environment and fatigue loading, have not been investigated in any detail.

This investigation therefore aimed at studying the mechanical properties and corrosion fatigue performance of 5083-H111 and 6061-T651 aluminium welded using semi-automatic and fully automatic pulsed gas metal arc welding, with ER4043, ER5183 and ER5356 filler wires. The influence of the weld metal and heat-affected zone microstructure, weld defects and the weld geometry on the mechanical properties and corrosion fatigue resistance was evaluated. The project also determined the fatigue damage ratio (the ratio of the fatigue life in a NaCl solution to the fatigue life in air) by comparing the S-N curves measured in NaCl and in air for 5083 and 6061 aluminium in the as-supplied and as-welded conditions.

This thesis contains six main chapters. Chapter 2 reviews the relevant literature pertaining to this investigation. The welding of alloys 5083 and 6061, their corrosion behaviour in chloride-containing solutions, mechanical properties and fatigue behaviour are discussed. Chapter 3 describes the experimental procedure followed during the course of this investigation to characterize the microstructure, mechanical properties, corrosion behaviour and fatigue properties (in air and in a 3.5% NaCl solution) of 5083-H111 and 6061-T651 in the as-supplied and as-welded conditions. The results obtained in this investigation, including weld metal microstructures, hardness profiles, tensile properties, fatigue performance, corrosion behaviour and corrosion fatigue properties in NaCl, are discussed in Chapter 4. Finally, Chapter 5 provides conclusions and recommendations regarding the corrosion fatigue performance of 5083-H111 and 6061-T651 aluminium alloy welds.

CHAPTER 2. LITERATURE SURVEY

2.1 Introduction

Aluminium and its alloys represent an important family of light-weight and corrosion resistant engineering materials. Pure aluminium has a density of only 2.70 g/cm^3, about one third that of steel or copper. As a result, certain aluminium alloys have better strength-to-weight ratios than high-strength steels. Some of the most important characteristics of aluminium are its good formability, machinability and workability. It can be cast by any known method, rolled to any desired thickness, stamped, drawn, spun, hammered, forged and extruded to almost any conceivable shape. It displays excellent thermal and electrical conductivity, and is non-magnetic, non-sparking and non-toxic [1,2].

Commercially pure aluminium (with a minimum aluminium content of 99.0%) is suitable for use in applications where excellent formability, high conductivity or very good corrosion resistance is required and where high strength is not essential. It has been used extensively in cookware, foil, wire and as paint pigment. One of the major drawbacks of aluminium, however, is its low strength. Pure aluminium has a tensile strength of only about 83 MPa, but it is possible to obtain substantial increases in strength through:

- strain hardening from cold work,
- solid solution strengthening due to alloying, and
- precipitation hardening (in heat treatable alloys).

These mechanisms can be used individually or in combination to achieve wide ranging mechanical property levels. This project focused exclusively on the fatigue resistance of two wrought aluminium alloys, AA5083 and AA6061. The fatigue resistance of these alloys in the as-received plate form, as well as welded using various filler materials, was investigated in air and in a 3.5% NaCl solution to characterize their corrosion fatigue resistance and susceptibility to pitting corrosion.

2.2 Aluminium alloys investigated during the course of this project

Wrought aluminium alloys are defined as those alloys that are plastically deformed by hot and/or cold working processes to transform a cast aluminium ingot into the desired product form. Individual wrought aluminium alloys are distinguished on the basis of the major alloying element(s) used to improve the properties of the alloy, and the four-digit system of numerical designations designed by the American Aluminum Association is widely used to identify wrought aluminium and wrought aluminium alloys [1,2]. Alloys can also be broadly divided into those that are hardenable through strain hardening only, and those that respond to precipitation hardening.

Aluminium alloys with the number “5” as first digit in the alloy designation are alloyed with magnesium as primary alloying element. Most commercial wrought alloys in this group contain less than 5% magnesium, and do not respond well to precipitation strengthening. As a result, these alloys are strain hardened to increase strength, hardness and wear resistance, and the applicable strengthening mechanism is the interaction between dislocations and solute atoms, second phase particles or grain boundaries. Magnesium-alloyed 5083 aluminium is characterized by good weldability, excellent corrosion resistance and moderate strength. It displays excellent performance in harsh environments and high resistance to attack in both seawater and industrial process streams. Aluminium alloy 5083, with the typical chemical

composition shown in Table 2.1, has the highest strength of the aluminium alloys that do not respond to precipitation heat treatment. It is used extensively for marine and welded structural applications, and finds application in shipbuilding, the aerospace industry, missile components, cryogenic tanks, tip truck bodies, unfired welded pressure vessels, armour plate, architectural, ornamental and decorative trim, in household appliances, vehicle bodies, beverage cans and can ends [1,3].

Table 2.1. Typical compositions of aluminium alloys 5083 and 6061 (percentage by mass) [2].

Alloy	*Al*	*Mg*	*Mn*	*Fe*	*Si*	*Cr*	*Cu*	*Zn*	*Ti*
5083	Balance	4.0-4.9	0.4-1.0	0.4	0.4	0.25	0.1	0.25	0.15
6061	Balance	0.8-1.2	≤ 0.15	≤ 0.7	0.4-0.8	0.04-0.35	0.15-0.40	≤ 0.25	≤ 0.15

Aluminium alloys with the number "6" as first digit in the alloy designation are alloyed with a combination of magnesium and silicon. Magnesium and silicon combine to form magnesium silicate (Mg_2Si), which in turn forms a simple eutectic system with aluminium. The precipitation of very fine needle-like precipitates of Mg_2Si (or β') homogeneously distributed throughout the aluminium matrix through artificial ageing (the -T6 temper condition) allows these alloys to reach their full strength. Magnesium and silicon are usually present in the correct ratio to form magnesium silicate. Hardenable 6061 aluminium (with a typical composition shown in Table 2.1) is characterized by excellent corrosion resistance, good weldability and good machinability, and is considered to be more workable than other heat-treatable alloys. Typical applications include tip truck bodies, ship building, piping, bicycle frames, canoes, furniture, vacuum-cleaner tubing, auto-body sheets, bridge railings and architectural trim. Al-Mg-Si casting alloys provide a desirable combination of castability, pressure-tightness, strength and corrosion resistance [1,2].

Aluminium alloys 5083 and 6061 are welded extensively in industry and both alloys are considered to possess good weldability. Although welding processes such as laser beam welding and friction stir welding are gaining popularity for joining aluminium and its alloys, arc welding is still the most widely used joining process in the shipbuilding, aerospace, pipeline, pressure vessel, automotive and structural industries. The mechanical properties of the welded joint, the weld geometry, occurrence of flaws and level of residual stress after welding depend mainly on the joining process, welding consumable and procedure employed. During the course of this investigation, semi-automatic and fully automatic pulsed gas metal arc welding (GMAW) was used to produce welded joints using various filler metals. This process is considered in more detail below.

2.3 Welding of 5083 and 6061 aluminium

2.3.1 Pulsed Gas Metal Arc Welding (P-GMAW)

In gas metal arc welding (GMAW), the heat required to fuse the metals is generated by an electric arc established between a consumable electrode wire and the workpiece. The electric arc and the molten weld pool are shielded from atmospheric contamination by an externally supplied shielding gas or gas mixture. Removal of the oxide layer from the aluminium surface through cathodic cleaning is possible if argon-rich shielding gas is used. No flux is required, therefore the weld is not obscured by slag during welding. Gas metal arc welding may be used in the semi-automatic mode, i.e. the filler wire is fed at a constant speed by a wire feeder, while the welder manipulates the welding torch manually, or in the fully automatic mode, i.e. the filler wire is fed continuously at a constant speed, while the torch is manipulated automatically. High deposition rates and high welding speeds can be maintained with this process [4].

With a pulsed power supply, the metal transfer from the tip of the electrode wire to the workpiece during GMAW is controlled. Pulsed current transfer is a spray-type transfer that occurs in pulses at regularly spaced intervals rather than at random intervals. The current is pulsed between two current levels. The lower level serves as a background current to preheat the electrode (no metal transfer takes place), while the peak current forces the drop from the electrode tip to the weld pool. The size of the droplets is approximately equal to the wire diameter. Drops are transferred at a fixed frequency of approximately 60 to 120 per second. As a result, spray transfer can take place at lower average current levels than would normally be the case. The pulsed mode of transfer is suited to all welding positions, as the weld pool is smaller and easily controlled. Due to the lower average heat input, thinner plates can be welded, distortion is minimized and spatter is greatly reduced. The pulsed GMAW process is often preferred for welding aluminium and aluminium alloys as the lower average heat input reduces the grain size of the weld and adjacent material and decreases the width of the heat-affected zone (HAZ) [5-8].

High welding currents generally produce the highest quality welds in aluminium alloys and, when combined with high welding speeds, minimize distortion and reduce the effect of welding on the mechanical properties of the heat-affected zone (HAZ). High welding currents also allow welds to be completed in fewer passes with little or no edge preparation. Higher welding currents (up to 500 A with argon shielding gas, and more than 500 A with helium shielding) are normally used with automatic welding than with semi-automatic welding. Automatic welding therefore usually requires fewer weld passes and less edge preparation, eliminates back chipping and reduces labour costs. When higher welding currents are combined with faster welding speeds, lower heat input levels may be achieved during automatic welding (compared to those achieved during semi-automatic welding). Automatic GMAW typically utilizes shorter arc lengths, higher welding currents and faster travel speeds to achieve deeper penetration than semi-automatic welding. Contamination from dirty joint edges or burrs may appear as voids in the weld [5,6].

The weld penetration, bead geometry, deposition rate and overall quality of the weld are also affected to a significant extent by the welding current, arc voltage (as determined by the arc length), travel speed, electrode extension, electrode orientation (or gun angle) and the electrode diameter. Excessive arc voltages or high arc lengths promote porosity, undercut and spatter, whereas low voltages favour narrow weld beads with higher crowns. The travel speed affects the weld geometry, with lower travel speeds favouring increased penetration and deposition rates. Excessively high travel speeds reduce penetration and deposition rate, and may promote the occurrence of undercut at the weld toes [4].

The welding current, arc voltage and travel speed determine the heat input (HI) during welding. This relationship is shown in equation (2.1).

$$\mathrm{HI} = \eta \frac{VI}{v} \qquad \ldots(2.1)$$

where: V is the arc voltage (V), I is the welding current (A), v is the travel speed, and η is the arc efficiency factor (typically in the region of 0.7 to 0.8 for GMAW).

2.3.2 Structure of the welds

A typical arc weld in aluminium forms when the heat generated by the arc (as quantified by the heat input) melts the filler metal and the base metal in the region of the joint. The filler metal and the melted-back base metal form an admixture, with the level of mixing determined by the contribution of the melted-back base metal to the total volume of the fused metal (or the level of dilution in the weld). The properties of the weld, such as strength, ductility,

resistance to cracking and corrosion resistance, are strongly affected by the level of dilution. The dilution, in turn, depends on the joint design, welding process and the welding parameters used. A more open joint preparation during welding (for example a larger weld flank angle, φ, in Figure 2.1(a) or a wider root gap, *B*, in Figure 2.1(b)) increases the amount of filler metal used, reducing the effect of dilution. The precipitation-hardenable aluminium alloys (such as 6061) are usually welded with non-matching consumables to reduce susceptibility to solidification cracking. High dilution levels should be avoided when welding these materials to prevent excessive dilution of the crack resistant filler metal with the more crack susceptible base metal. For this reason joint preparations such as single V-grooves or double V-grooves are often preferred to square edge preparations when welding crack susceptible material with non-matching filler metal [6].

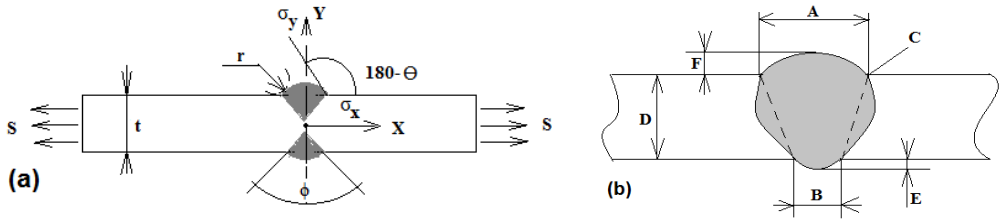

Figure 2.1. (a) Schematic illustration of the geometrical parameters relevant to a typical butt weld with a double V edge preparation, where r is the weld toe radius, φ the weld flank angle and t the plate thickness; and (b) the geometrical structure of a weld, where A is the weld face, B the root of the weld, C the weld toe, D the plate thickness or weld penetration, E the root reinforcement, and F the face reinforcement.

The thermal cycle experienced by the metal during welding results in various zones that display different microstructures and chemical compositions (shown schematically in Figure 2.2). The fusion zone (also referred to as the composite zone or weld metal) melts during welding and experiences mixing to produce a weld with a composition intermediate between that of the melted-back base metal and the deposited filler metal. The unmixed zone cools too fast to allow mixing of the filler metal and molten base metal during welding, and displays a composition almost identical to that of the base metal. The partially melted zone experiences peak temperatures that fall between the liquidus and solidus temperatures of the base metal, and therefore partially melts during welding. The heat-affected zone (HAZ) represents base metal heated to high enough temperatures to induce solid-state metallurgical transformations, without any melting [4].

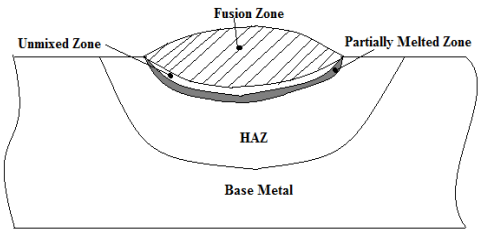

Figure 2.2. Schematic illustration of the compositional structure of a typical fusion weld.

Most welds contain discontinuities or flaws which may lead to ultimate failure of the component. These flaws need to be removed or repaired if there is a likelihood of such a defect growing to critical size within the design life of the component. Defects or flaws may be design or weld related, with the latter group including defects such as undercut, slag or oxide inclusions, porosity, overlap, shrinkage voids, lack of fusion, lack of penetration,

craters, spatter, arc strikes and underfill. Metallurgical imperfections such as cracks, fissures, chemical segregation and lamellar tearing may also be present. Geometrical discontinuities, mostly related to imperfect shape or unacceptable bead contour, are often associated with the welding procedure and include features such as undercut, underfill, overlap, excessive reinforcement and mismatch. Some of these defects are illustrated schematically in Figure 2.3 [4].

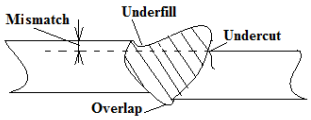

Figure 2.3. Schematic illustration of geometric weld discontinuities.

Weld related discontinuities are often caused by excessive heat input or slow welding speeds, high levels of dilution caused by the joint design, high induced stresses and incorrect filler metal selection (often leading to solidification cracking in the form of crater cracks or centreline fissures). Incomplete penetration or poor fusion may be caused by low current levels, long arc lengths and excessive welding speeds. Unstable welding arcs and excessive current levels may promote the formation of inclusions, whereas the occurrence of undercut is usually associated with the use of incorrect welding techniques. Aluminium welds are also very susceptible to hydrogen-induced porosity. The molten weld pool may dissolve large amount of hydrogen from the arc atmosphere. On solidification, the solubility of hydrogen decreases and the trapped hydrogen forms gas porosity or blow holes. Typical sources of hydrogen contamination are lubricant residues, moisture and the hydrated surface oxide on the base metal or filler wire surface. These defects act as stress concentrations and may lead to rapid fatigue crack initiation if the weld is exposed to fluctuating stresses of sufficient magnitude [5,6].

Most weld flaws can be removed by grinding, machining and/or flush polishing, thereby improving the mechanical properties, corrosion resistance and fatigue properties of the joint. Subsurface flaws, which are more prevalent during semi-automatic welding than fully-automatic welding, are more difficult to detect and correct.

2.3.3 Weldability of aluminium 5083 and 6061 aluminium

Aluminium alloys are readily weldable using various welding processes (including friction stir welding, resistance welding, arc welding and laser welding) provided the properties of aluminium are taken into account and precautions taken where necessary (see Table 2.2 for a summary of the physical properties of 6061 and 5083 aluminium). The weld may be affected by the presence of a naturally occurring surface oxide layer, the high solubility of hydrogen in molten aluminium, the high thermal and electrical conductivity, the lack of colour change when heated and the wide range of physical properties that result from the presence of alloying elements (such as changes in melting range and coefficient of expansion differences) [4-6].

Table 2.2. Typical chemical composition, physical properties and weldability of wrought aluminium alloys 6061 and 5083 [4].

Base metal	*Chemical composition, wt %*						*Melting point, ºC*	*TC at 25ºC, W/m.K*	*EC, % IACS*	*GMAW W*
	Al	*Mg*	*Si*	*Mn*	*Cr*	*Cu*				
5083	Bal.	4.4	-	0.7	0.15	-	574-638	117	29	A
6061	Bal.	1.0	0.6	-	0.2	0.28	582-652	167	43	A

where: TC is the thermal conductivity, EC the electrical conductivity and W the weldability. A indicates that the alloy is readily weldable.

Pure aluminium exhibits high electrical conductivity, about 62% that of pure copper. Very little resistance heating occurs during welding, and high heat inputs are therefore required when joining aluminium and its alloys to ensure complete fusion. Incomplete fusion may also result from the presence of the hydrated aluminium oxide layer that forms spontaneously on exposure to air or water due to the strong chemical affinity of aluminium for oxygen. This layer melts at about 2050ºC, significantly above the melting range of aluminium. In order to prevent poor fusion, the aluminium oxide layer needs to be removed prior to or during welding. Suitable fluxes, chemical or mechanical cleaning methods, or the cleaning action of the welding arc in an inert argon atmosphere (cathodic cleaning) can be used to remove the oxide [5]. The high thermal expansion coefficient of aluminium (about twice that of steel) may result in distortion and high levels of residual stress in the welds, and precautions need to be taken to control distortion to within acceptable limits.

The weldability of aluminium, defined as the resistance of the material to the formation of cracks during welding, is affected by the physical properties, chemical composition and prior temper state of the material. Heat treatable aluminium alloys (or those alloys that respond to precipitation strengthening) are prone to solidification cracking during welding. These alloys exhibit a wide solidification temperature range. If such an alloy is cooled from the liquidus temperature, the growing crystals are at first separated by liquid and the alloy has no strength. As the temperature decreases, the volume of solid increases relative to that of the liquid, and at some point (the coherence temperature) the growing crystals meet and cohere. However, a limited amount of liquid remains down to the eutectic temperature, causing the metal to be brittle. At the same time, the solid phase contracts and is subjected to tensile stresses which may be high enough (depending on the level of restraint) to cause failure of the weak, brittle matrix. The risk of cracking is greatest when a critically small volume of liquid is present below the coherence temperature. Solidification cracking is severe in the magnesium-silicon type aluminium alloys, such as 6061, and fusion welding of this alloy with matching filler metal is only practicable under conditions of very low restraint [5].

As long as dilution is controlled to a minimum, these alloys can, however, be welded successfully using non-matching filler metal. A dissimilar filler metal with a lower solidus temperature than the base metal is generally employed so that the hardenable base metal is allowed to completely solidify and develop some strength along the fusion line before weld solidification stresses develop. Many of the filler metals used are non-hardenable and depend on dilution with the base metal to give a weld metal composition responsive to postweld heat treatment. Filler wires containing approximately 5% silicon, such as ER4043, aluminium-magnesium alloys or aluminium-magnesium-manganese consumables may be used. ER4043 filler wire solidifies and melts at temperatures lower than the solidification temperature range of the base metal. Contraction stresses, which could cause cracking, are relieved by the plasticity of the still liquid filler metal, preventing the formation of cracks. The Al-Mg and Al-Mg-Mn alloys, such as ER5356 and ER5183, are often employed as welding consumables since these materials provide an optimum combination of mechanical properties, corrosion resistance and crack resistance. The chemical compositions of the filler wires employed during the course of this project are shown in Table 2.3 [5].

The magnesium-alloyed non-hardenable grades of aluminium, such as 5083, are normally welded with near-matching filler metal. Consumables with slightly higher magnesium contents, such as ER5356 and ER5183, increase the strength of the weld and reduce the crack sensitivity. Small amounts of grain refiners, such as titanium, may be added to reduce the

grain size and improve crack resistance during welding, as shown in Table 2.3. High silicon consumables, such as ER4043, should be avoided when welding 5083 since excessive volumes of Mg-Si eutectic component may develop in the weld, reducing ductility and increasing crack sensitivity [5].

Table 2.3. Chemical composition and melting point of filler metals typically used in joining aluminium alloys [4,5]

Filler metal	*Chemical composition, wt %*						*Melting range, °C*
	Al	*Mg*	*Si*	*Mn*	*Cr*	*Ti*	
ER4043	Balance	-	5.25	-	-	-	574-632
ER5183	Balance	4.75	-	0.75	0.15	-	579-638
ER5356	Balance	0.12	-	0.12	0.12	0.13	571-635

The mechanical properties, fatigue performance and corrosion resistance of the welded joint depend on the filler metal used, and an optimal filler wire for a specific application needs to be selected. The filler metal selected should lead to ease of welding, freedom from cracking, moderate weld tensile and shear strengths, good ductility, good corrosion resistance and an acceptable colour match with the base metal after anodizing [5]. Tables 2.4 and 2.5 provide guidance on the selection of filler metals for 5083 and 6061 aluminium.

Table 2.4. Recommended filler metals for welding 5083 and 6061 (based on strength, corrosion resistance, colour match and cracking tendency) [4].

Base metal	*Strength*	*Ductility*	*Colour match*	*NaCl corrosion resistance*	*Least cracking tendency*
5083	ER5183	ER5356 ER5556	ER5183 ER5356	ER5183	ER5356 ER5183
6061	ER5356 ER4043	ER5356 ER4043	ER5356 ER4043	ER5356 ER4043	ER5356 ER4043

Table 2.5. Filler metal selection for 5083 and 6061 welds [4].

Base alloys to join	*Filler alloys*	*Filler characteristics*				
		Ease of welding	*As-welded strength*	*Ductility*	*Corrosion resistance*	*Colour match*
6061-5083	ER4043	A	D	C	A	-
	ER5183	A	A	B	A	A
	ER5356	A	B	A	A	A
6061-6061	ER4043	A	C	B	A	-
	ER5183	B	A	A	C	B
	ER5356	B	B	A	C	A
5083-5083	ER5183	A	A	B	A	A
	ER5356	A	-	A	A	A

where: A, B, C and D are relative ratings, with A: best and D: worst.

As shown in Tables 2.4 and 2.5, filler metal selection plays a major role in determining the corrosion resistance of the welded joint. The corrosion resistance is also affected by the prior heat treatment condition (or temper state) of the aluminium, the cleanliness of the alloys, the chemical and physical environment and the welding process. In the as-welded condition, however, the weld metal and heat-affected zone, and any welding defects, are most likely to

become preferential corrosion sites. A more detailed discussion of the corrosion resistance of 5083 and 6061 aluminium is provided in the next section.

2.4 Corrosion resistance of 5083 and 6061 aluminium

Aluminium and its alloys generally exhibit good corrosion resistance in a wide range of environments. The corrosion resistance of aluminium is derived from a thin, hard and compact film of adherent aluminium oxide that forms spontaneously on the surface of the material. This thin hydrated oxide film, only about 5 nm (or 50 Å) in thickness, grows rapidly whenever a fresh aluminium surface is exposed to air or water. Aluminium oxide is dissolved in some chemical solutions, such as strong acids and alkalis, leading to rapid corrosion. As shown by the Pourbaix diagram in Figure 2.4, the oxide film is usually stable over a range of pH values between 4.0 and 9.0, with water soluble species forming in low pH (Al^{3+}) and high pH (AlO_2^-) in aqueous solutions [9,10].

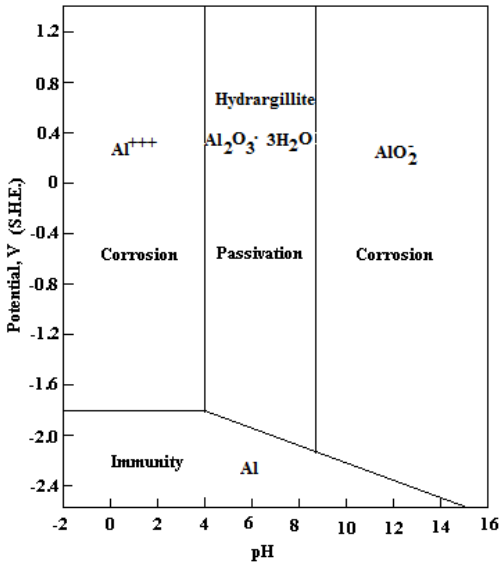

Figure 2.4. Pourbaix diagram for aluminium with stability regions representing the hydrated oxide film of hydrargillite ($Al_2O_3.3H_2O$), and the dissolved species Al^{3+} and AlO_2^- at 25°C (potential values are given relative to the standard hydrogen electrode) [10].

The corrosion resistance of 5083 and 6061 aluminium is normally reduced by welding. A band of material on either side of the weld tends to exhibit lower corrosion resistance [11,12]. This is considered in more detail below.

2.4.1 Corrosion of 5083 and 6061 aluminium welds

The thin oxide layer formed spontaneously on aluminium alloy surfaces renders these alloys resistant to corrosion in many environments. These passive films are, however, susceptible to localised breakdown at the exposed surface or at discontinuities, which result in high dissolution rates of the underlying metal (most frequently presented as pitting corrosion). The corrosion resistance of 5083 and 6061 is not altered significantly by the heat input during welding. The chemical composition of the weld metal and heat-affected zone and the presence of inclusions, precipitates and second phases in the welded joint, however, produce slightly different electrode potentials in the presence of an electrolyte, as illustrated schematically in Figure 2.5. Selective localized corrosion is therefore possible when the base metal and the weld metal or second phases possess significantly different electrode potentials. A galvanic effect may occur, with the more active region corroding preferentially to protect the more noble region with which it is in contact. When aluminium 6061-T6 is welded with ER5356

filler alloy, for example, the weld is attacked preferentially to protect the 6061 base metal. Optimal corrosion resistance is obtained when the electrode potential of the filler metal is the same as that of the base metal [13,14].

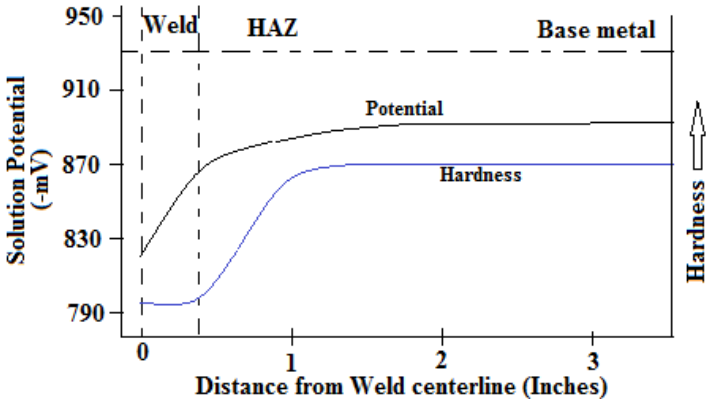

Figure 2.5. Schematic illustration of the change in solution potential and hardness in the weld metal and heat-affected zone of alloy 5083 [9].

Welds produced by the GMAW process appear to be less resistant to pitting corrosion in salt water solutions than solid state friction stir welds of 6060-T5 and 6082-T6, as reported by Moggiolino and Schmid [11]. Preferential attack occurs in the narrow interface between the weld bead and the HAZ, or between the HAZ and the base metal. As a result of the high peak temperatures experienced by the high temperature HAZ adjacent to the fusion line, grain coarsening, recrystallization and partial dissolution of intermetallic strengthening precipitates occur during welding. On cooling, uncontrolled reprecipitation at grain boundaries can occur if the cooling rate is not too fast. Inclusions, precipitates, gas pores and grain boundaries in 5083 and 6061 can create localized galvanic cells between these discontinuities and the bulk metal matrix, resulting in the preferential initiation of corrosion pits in aggressive environments.

2.4.2 Mechanism of pitting corrosion in 5083 and 6061 aluminium welds

Pitting corrosion is a form of localized corrosion that occurs in environments in which a passive surface oxide film is stable. Pits initiate due to local rupture of the passive film or the presence of pre-existing defects, and then propagate in a self-sustaining manner. Localized corrosion can initiate as a result of the difference in corrosion potential within a localized galvanic cell at the alloysurface. These micro-galvanic cells can form at phase boundaries, inclusion/matrix interface areas and at insoluble intermetallic compounds [10]. The most widely mechanism for pitting corrosion in aluminium alloys is described below.

The aluminium oxide passive film consists of two superimposed layers with a combined thickness between approximately 4 and 10 nm. The first compact and amorphous layer in contact with the alloy forms as soon as the material comes into contact with air or water. It forms quickly, within a few milliseconds, according to the reaction shown in equation (2.2):

$$2Al + 3/2\ O_2 \rightarrow Al_2O_3 \quad (\Delta G = -1675\ kJ) \qquad \ldots(2.2)$$

The second layer grows over the initial film due to a reaction with the corrosive environment, likely by hydration (reaction with water or moisture). The second layer is less compact and more porous, and may react with the corrosive environment (as illustrated in Figure 2.6). The rate of formation and the surface properties of the second oxide layer depend on the chemical composition of the layer itself, and not on that of the underlying metal. Certain elements, such

as magnesium, strengthen the protective properties of the oxide film, whereas copper tends to weaken the corrosion resistance of the passive layer [9].

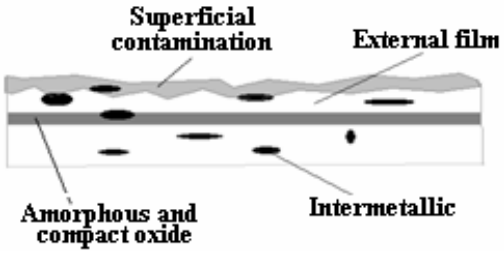

Figure 2.6. Schematic illustration of the typical structure of the aluminium oxide passive layer [9].

The breakdown of the passive film (leading to pit initiation) is usually associated with the presence of inclusions or second-phase particles in the aluminium matrix, scratches, residual welding slag and impurities. As shown in Figure 2.7, localized breakdown of the passive film initiates above the critical pitting potential (E_{pit}). The pitting potential is often stated to quantify the resistance of a material to pitting corrosion, and represents the potential in a particular solution above which stable pits may form. More noble pitting potential values (E_{pit}) signify increased resistance to pitting corrosion. The presence of aggressive anionic species, such as chloride ions (which increase the potentiostatic anodic current at all potentials), increases the likelihood of pitting corrosion [10].

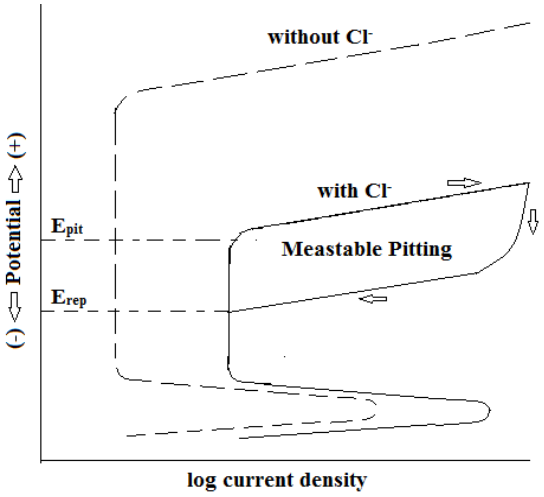

Figure 2.7. Schematic illustration of a polarization diagram, illustrating the position of the critical pitting potential, E_{pit}, and the repassivation potential (or protection potential), E_{rep} [10].

The value of E_{pit} in NaCl solutions remains unaffected by the dissolved oxygen concentration in the solution and moderate temperature variations (0°C to 30°C). At temperatures above 30°C, the pitting corrosion rate increases considerably. A rough surface finish increases susceptibility to pitting corrosion and reduces the pitting potential. Conversely, the presence of oxidizing agents, such as chromium, increases E_{pit} and the alloy becomes more noble and more resistant to pitting attack. The repassivation or protection potential shown in Figure 2.7 represents the minimum potential at which existing pits can propagate, but new pits cannot form.

As described above, pitting corrosion typically develops in the presence of chloride ions (Cl^-). The chloride ions are adsorbed on the aluminium oxide layer, followed by rupture of the oxide film at weak points and formation of micro-cracks that are a few nanometres wide. At the same time, oxygen is reduced at cathodic sites and rapidly oxidizes the aluminium by

forming an intermediate complex chloride, $AlCl^{4-}$, in areas associated with cracks in the oxide film. In aluminium and its alloys, chloride activity appears to be more important than acidity in controlling pit initiation and growth [13-16].
As the pit deepens, the rate of transport of ions out of the pit decreases. The pit current density therefore tends to decrease with time, owing to an increase in the pit depth and ohmic potential drop. Depending on the alloy composition and microstructure and the chemistry of the environment, pits can be shallow, elliptical, narrow and deep, undercut, vertical, horizontal or sub-surface. Repassivation may also occur if the dissolution rate at the bottom of the pit is insufficient to replenish the loss of aggressive environment due to reaction, and the pit may stop growing after few days. Pitting can continue on fresh sites [9,10].

A small fraction of initiated pits will propagate according to the reactions shown below in equations (2.3) to (2.10) [9]:

$$2Al \rightarrow 2Al^{3+} + 6e^{-} \quad \text{(anodic oxidation of Al, dissolution)} \quad \ldots(2.3)$$

$$3/2\ O_2 + 3H_2O + 6e^{-} \rightarrow 2(OH)_3^{-} \quad \text{(cathodic reduction in alkaline/neutral media)} \quad \ldots(2.4)$$

$$H_2O \leftrightarrow H^{+} + OH^{-} \quad \text{(dissociation of water)} \quad \ldots(2.5)$$

$$6H^{+} + 6e^{-} \rightarrow 3H_2 \quad \text{(cathodic reduction of } H^{+} \text{ in acidic media)} \quad \ldots(2.6)$$

$$O_2 + 4H^{+} + 4e^{-} \rightarrow 2H_2O \quad \text{(oxygen reduction in acidic media)} \quad \ldots(2.7)$$

$$2Al + 3H_2O + 3/2\ O_2 \rightarrow 2Al\ (OH)_3 \quad \text{(in alkaline or neutral media)} \quad \ldots(2.8)$$

$$2Al + 6H^{+} \rightarrow 2Al^{3+} + 3H_2 \quad \text{(in alkaline or neutral media)} \quad \ldots(2.9)$$

$$2Al + 6H_2O \rightarrow 2Al\ (OH)_3 + 3H_2 \quad \text{(in alkaline or neutral media)} \quad \ldots(2.10)$$

Al^{3+} ions, highly concentrated in the bottom of the pit, diffuse towards the pit opening and react with the more alkaline solution on the plate surface, facilitating the formation of $Al(OH)_3$. Hydrogen micro-bubbles formed in the pit may transport the $Al(OH)_3$ to the pit opening where it forms an insoluble deposit that appears as white eruptions around the pit surface. The formation of positively charged Al^{3+} ions in the bottom of the pit may also attract Cl^{-} ions towards the underside of the pit, encouraging the formation of the complex chloride $AlCl^{4-}$ (through the reaction $Al^{3+}+Cl^{-}+6e^{-}\rightarrow AlCl^{4-}$), as shown in Figure 2.8. The accumulation of $Al(OH)_3$ forms a dome at the pit surface which progressively blocks the pit opening. This can hinder the exchange of Cl^{-} ions which may gradually retard or even arrest pit growth. A corrosion pit may therefore be considered as a local anode surrounded by a matrix cathode. Once pitting corrosion has initiated, pit growth becomes sustainable at lower potentials than the pitting potential. As the hydrolysis reaction of dissolved cations acidifies the solution at the bottom of the pit and the medium becomes increasingly aggressive, pit growth becomes an autocatalytic process [9,10,13-16].

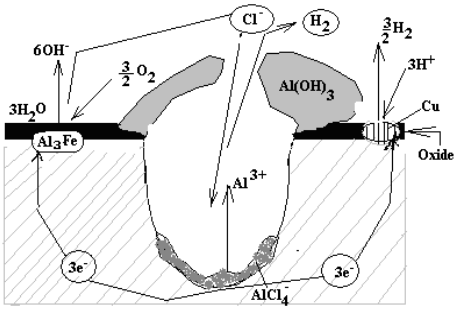

Figure 2.8. Schematic illustration of the mechanism of pitting corrosion in aluminium [9].

As described earlier, the final mechanical properties and corrosion resistance of aluminium alloys are related to the chemical composition, fabrication process and heat treatment received. Alloying elements have been shown to affect the dissolution potentials of aluminium alloys (see Figure 2.9). Silicon, manganese and copper increase the dissolution

potential. The addition of magnesium to aluminium, even though it lowers the potential of the alloy, improves the corrosion resistance because magnesium stabilizes and thickens the aluminium oxide film. Cold working, on the other hand, generally reduces the corrosion resistance of the magnesium-alloyed grades, as the β-Al_3Mg_2 phase may precipitate on grain boundaries and dislocations, increasing susceptibility to stress corrosion cracking. Inclusions, impurities, pores, vacancies, dislocation walls and grain boundaries may generate galvanic cells in 5083 and 6061 alloys. Cored structures (non-uniform chemical composition from the grain boundary region to the interior of a grain) promote galvanic interaction and point defects are usually more anodic than the surroundings. The corrosion resistance of an alloy with more than one phase is usually less than that of an equivalent single-phase alloy [15-16].

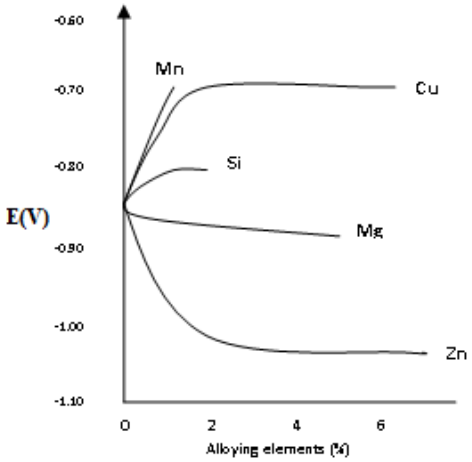

Figure 2.9. Influence of alloying elements on the dissolution potential of aluminium alloys [14] .

Wrought Al-Mg alloys (such as 5083) are more resistant to seawater corrosion than the Al-Mg-Si alloys, with 6061 being prone to pitting corrosion on immersion in chloride-containing seawater at a pH around 7. As shown in Table 2.6, intermetallic phases such as Al_3Mg_2, $MgZn_2$ and Mg_2Si, are anodic with respect to the alloy matrix (5083 or 6061), and promote rapid localized attack through galvanic interaction. Less electronegative intermetallic phases, such as Al_3Fe, Al_2Cu and Si, are cathodic with respect to the aluminium matrix, leading to preferential dissolution of the alloy matrix. The area ratio (small cathodic area and large anodic area) is, however, beneficial in this case, leading to low corrosion rates in the bulk matrix [9,15,16].

Table 2.6. Relative electrochemical potentials for aluminium, its alloys and typical intermetallic phases in a NaCl solution [9,15,16]. (Potential given relative to the saturated calomel electrode).

Metal, alloy or intermetallic phase	*Potential, (V)*
Al_8Mg_5	-1.24
Mg_2Si (intermetallic phase)	-1.19
Al_3Mg_2 (intermetallic phase)	-1.15
$MgZn_2$ (intermetallic phase)	-0.96
Al_2CuMg (intermetallic phase)	-0.91
Mg	-0.85
Al_6Mn (intermetallic phase)	-0.80
Al5083, Al5183	-0.78
Al5454	-0.77
Al1060, Al1050	-0.75
Al6061, Al6063	-0.74
Al_2Cu (intermetallic phase)	-0.64

Al_3Fe (intermetallic phase)	-0.51
Al_3Ni (intermetallic phase)	-0.43
Si (second phase)	-0.20

The pit density (spacing), size of the pit opening and pit depth can be used to evaluate the pitting corrosion resistance of alloys, although the required evaluation procedure is time consuming and tedious for large numbers of specimens. A pit depth measurement using an optical microscope is often the preferred way of evaluating pitting corrosion. The pitting factor (p/d) may also be used, where p is the maximum pit penetration depth and d is the average pit penetration depth. The pit depth increases, not only with time, but also with surface area, and can be estimated using equation (2.11):

$$d_1 = K t_1^{1/3} \quad \ldots(2.11)$$

where: d_1 is the pit depth at time t_1 and k is a constant.

The time to perforation (t_2) can be estimated by equation (2.12):

$$t_2 = t_1 \left(\frac{d_2}{d_1}\right)^3 \quad \ldots(2.12)$$

where: d_2 is wall thickness of the component at time t_2 [10].

Pitting corrosion often acts as a precursor to more aggressive modes of corrosion, such as stress corrosion cracking and corrosion fatigue cracking. Pits form severe stress concentrations at the metal surface and often act as preferential crack initiation sites [14,15].

As shown in the preceding discussion, the presence of a weld often promotes corrosion due to changes in local microstructure and precipitate distribution, and the increased likelihood of defects. Welding also affects the mechanical properties of the aluminium alloy in the vicinity of the joint. Any localized change in mechanical properties can, in turn, influence the corrosion behaviour and the fatigue properties of the material. The influence of the weld thermal cycle on the mechanical properties of the weld is considered below.

2.5 Mechanical properties of welded 5083 and 6061 aluminium

Aluminium alloys 5083 and 6061, produced via ingot casting, cold working and/or heat treatment, contain precipitates that interact with moving dislocations, thus increasing strength at room temperature. When these alloys are welded, however, the precipitates dissolve and/or coarsen, reducing the mechanical strength significantly. This effect is more pronounced in the precipitation hardenable aluminium alloys, such as 6061. It is estimated that the typical mechanical strength of the weld metal and HAZ is reduced to about half that in the parent metal. This reduction in mechanical properties can be attributed to grain growth, precipitate dissolution or coarsening, recrystallization and uncontrolled grain boundary precipitation on cooling. The HAZ may extend up to 38 mm from the weld fusion line, depending on the heat input and weld thermal cycle. Welds are therefore often the weakest links in fabricated components due to changes in local microstructure and chemical composition, and the introduction of tensile residual stresses [18-20]

In most butt welds, the properties of the weld metal and HAZ control the mechanical performance of the alloy, whether in the heat treated or cold worked condition. The HAZ of cold worked non-hardenable aluminium alloys, such as 5083, is completely annealed and recrystallized during welding. The effect of any prior work hardening is lost when such an alloy is exposed to a temperature above 343ºC for even a few seconds [18,19]. A significant reduction in hardness is therefore observed in the HAZ of cold worked alloys during welding.

The annealing effect described above is not normally observed in precipitation hardenable alloys, such as 6061, during welding. In these alloys annealing times of two to three hours, followed by slow cooling, are usually required for full annealing. On welding, the partial or full dissolution of β" strengthening precipitates and the uncontrolled precipitation of β'-$Mg_{1.7}Si$ (associated with less strengthening than β") result in significant softening in the high temperature heat-affected zone adjacent to the fusion line. Stringer bead techniques need to be used when maximum tensile properties are required. In this technique a higher number of low heat input passes are used, with the joint being cooled to room temperature between passes. This technique minimizes the time at temperature and ensures a narrower HAZ [5].

The degree of softening in aluminium alloys is mainly affected by the preheat temperature, the peak temperature reached during welding, the time at peak temperature, the amount of interpass cooling, the heat input, the welding technique, the size of the workpiece and the rate of cooling. Low heat input levels reduce the time at temperature and increase the cooling rate, thereby minimizing the degree of softening in the HAZ. Low heat input processes and techniques are therefore recommended for improved mechanical properties in the HAZ [5]. Pulsed GMAW has the advantage of ensuring good penetration and adequate fusion at lower average heat input levels [6-8]. The amount of grain growth is reduced and the width of the HAZ minimized.

As shown in Table 2.7, welds in 5083 aluminium generally display reasonable ductility and high strength when near-matching filler metals such as ER5183 and ER5356 are used. Aluminium alloy 6061, welded with non-matching Al-Mg (ER5356) or Al-Si (ER4043) filler metal, performs less well during tensile testing, exhibiting low ductility and strength in the as-welded condition.

Table 2.7. Mechanical properties of butt joints in aluminium 5083 and 6061 welded using various filler metals [4,5].

Base alloy	*Filler metal*	*Ultimate tensile strength, MPa*	*Minimum. yield stress, MPa*	*Tensile elongation, % (50.8 mm gauge)*	*Free bending elongation, %*
5083	5183	276-296	165	16	34
5083	5356	262-241	117	17	38
6061-T6	5356	207	131	11	25
6061-T6	4043	186	124	8	16

The hardness is usually significantly lower in the weld metal and HAZ than in the base alloy. This is attributed to annealing and recrystallization (in cold worked alloys), grain growth and precipitate dissolution and/or overageing. Heat treated and artificially aged 6061-T651 contains fine, dispersed metastable precipitates of β". During welding, the high peak temperatures experienced during the weld thermal cycle may cause the fine precipitate particles to go into solution, resulting in a low hardness in the high temperature heat-affected zone adjacent to the fusion line (region 1 in Figure 2.10). Uncontrolled reprecipitation may occur at grain boundaries during cooling. At locations 2 and 3 in Figure 2.10, the precipitate particles partially dissolve and coarsen, resulting in intermediate hardness values. Within region 4, the peak temperature during welding is not high enough to cause dissolution or significant coarsening and the hardness approaches that of the unaffected base metal [5].

The mechanical strength of a typical gas metal arc weld in 6061-T6 is reduced to such an extent by overageing within the HAZ adjacent to the fusion line that failure tends to take place in the HAZ. The weld thermal cycle in this region induces the transformation of coherent β" to incoherent β' in the α matrix. This transformation, as well as partial dissolution

of precipitates and grain growth, is responsible for the loss of mechanical strength in the HAZ of 6061-T6. Postweld ageing can improve the strength of the high temperature HAZ to a limited extent, but has little effect on the overaged region [5-8].

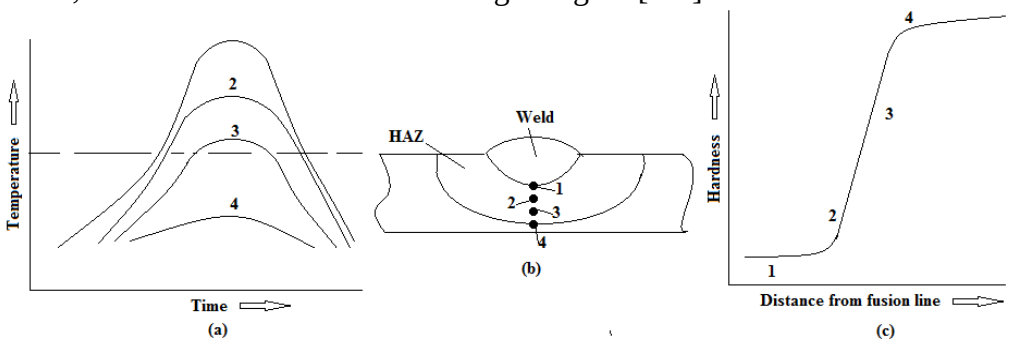

Figure 2.10. Schematic hardness profiles at various locations in the HAZ of a heat treatable alloy after welding.

As indicated above, both 5083 and 6061 display a reduction in strength and hardness in the heat-affected zone (HAZ). Furthermore, these alloys do not show a clear endurance limit during fatigue testing. The reduction in strength and hardness in the heat-affected zone, the presence of welding defects and the incidence of pitting corrosion are likely to negatively affect the fatigue properties of welded joints. This is considered in more detail below.

2.6 Fatigue behaviour of welds

Fatigue is a highly localized and permanent structural change involving the initiation and propagation of a crack under the influence of fluctuating stresses at levels well below the static yield stress required to produce plastic deformation. Under these conditions, fatigue cracks can initiate near or at discontinuities on or just below the free surface. These discontinuities may be present as a result of mechanical forming, heat treatment or welding and cause stress concentrations in the form of inclusions, second phases, porosity, lack of fusion, lack of penetration, weld toe geometry, shape changes in cross section, corrosion pits and grain boundaries. A typical fatigue fracture surface appears smooth and matt on a macroscopic level and displays concentric ‘beach marks’ radiating out from the fatigue initiation poin [21-23].

The fluctuating applied stress (represented as amplitude stress, (S_a), in this investigation) leads to plastic deformation (long-range dislocation motion) that produces slip steps on the surface. The dislocations may concentrate around obstacles, such as inclusions or grains boundaries, promoting fracture of inclusions or second phase particles, decohesion between the particles and the matrix, or decohesion along grain boundaries. These microcracks then grow and link up to form one or more macrocracks, which in turn grow until the fracture toughness is exceeded. Fatigue failure therefore typically occurs in five distinct steps: (1) cyclic plastic deformation prior to fatigue crack initiation, (2) initiation of one or more microcracks from slip bands, (3) propagation or coalescence of microcracks to form macrocracks, (4) propagation of macrocracks, and finally (5) catastrophic failure. Crack nucleation is strongly influenced by the fluctuating stress amplitude, the component shape, the environment, the temperature, mechanical properties of the alloy (in unwelded components), residual stress state and the surface condition of the component (in most cases cracks nucleate from the free surface) [19]. The presence of sharp notches or stress concentrations at the surface of the component facilitates crack initiation and reduces the time required to form a stable, propagating fatigue crack [21,23].

The lowest fatigue strength is usually associated with the highest stress concentration at the metal surface. The weld toe represents a sharp stress concentration in transversely loaded welds (see Figure 2.11) and fatigue cracks often initiate at the weld toe, followed by propagation into the base metal. Uneven root profiles can cause crack initiation at the weld root, followed by propagation into the weld metal. Stop/start positions and weld ripples can act as stress concentrations in longitudinal welds. Lack of penetration and undercut are severe stress raisers and can accelerate fatigue crack initiation, whereas internal defects (such as porosity and slag inclusions) usually only initiate fatigue cracks if surface stress concentrations are removed. Geoffroy *et al.* [24] confirmed that poor weld quality causes a significant reduction in fatigue life.

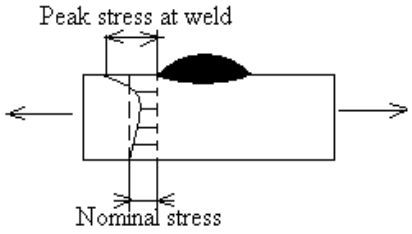

Figure 2.11. Stress concentration caused by the weld toe geometry.

The presence of inherent stress concentrations due to weld geometry or surface defects reduces the time required for fatigue crack initiation in welds. As a result, most of the fatigue life of welded samples is taken up by fatigue crack propagation (as shown by Figure 2.12) [21].

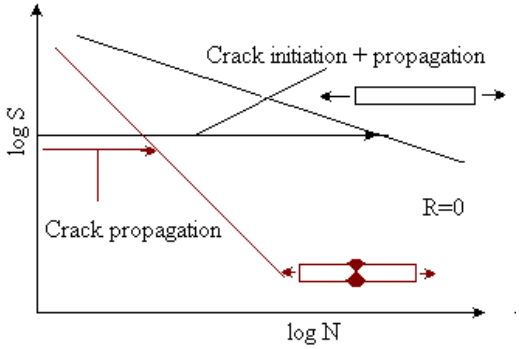

Figure 2.12. Comparison of schematic S-N curves of unwelded and welded samples illustrating the effect of fatigue crack initiation and propagation on total fatigue life [21].

The formation of residual stresses in welds is a consequence of the expansion and contraction of the weld metal and base metal close to the heat source and the restraining effect of the adjacent base alloy at lower temperatures. On cooling, high tensile residual stresses in the weld metal and HAZ are balanced by compressive residual stresses in the adjacent plate material. The magnitude of the residual stress introduced in the weld metal after welding depends on the tensile strengths of the weld and the base metal. In steels, these strengths are usually closely matched, but in heat-treatable aluminium alloys, the as-deposited weld can have lower strength than the parent metal and, consequently, residual stresses are not as high as the yield strength of the parent metal [21,25].

The presence of high tensile residual stresses in the weld metal and HAZ has two important consequences. First, fatigue failure can occur under loading conditions that, nominally, introduce compressive stresses, and second, the fatigue strength of welded joints is often governed by the applied stress range regardless of the nominal applied stress ratio. Due to the lower tensile strength of welds in the heat-treatable aluminium alloys, the applied stress ratio

may influence the fatigue strength of the joint to a limited extent, but fatigue design is usually based on the stress range and a single S-N curve represents the performance of a given welded joint for any minimum/maximum ratio of load input [21].

2.7 Corrosion fatigue performance of 5083 and 6061 aluminium

The fatigue behaviour of magnesium-alloyed or silicon-magnesium-alloyed aluminium after welding is determined by the weld microstructure and mechanical properties. Any stress concentration caused by a second phase particle of identifiable size and shape can nucleate a crack in a non-corrosive environment [26-28]. This effect is enhanced in a corrosive environment where corrosion pits are often associated with second phase particles in the matrix. Such a combination of a pit and a second phase particle may present a larger stress concentration than a pit or particle alone. Precipitates, second-phase particles, pores and grain boundaries within the matrix facilitate the nucleation and growth of corrosion pits in aggressive media and promote fatigue crack initiation and growth.

Under corrosion fatigue conditions, the shape of the fatigue loading cycle, the frequency and any periods of rest have a considerable influence on the fatigue life. The growth rate of corrosion pits increases with increasing stress amplitude and cyclic stress frequency [29-31]. As described below, the corrosive environment, the applied stress, the appearance of the fracture surface and the crack morphology can be used to characterize corrosion fatigue failure in aluminium alloy welds.

2.7.1 Features of corrosion fatigue fracture surfaces

Characterization and understanding of the kinetics and mechanisms of corrosion fatigue are indispensable to service life prediction, fracture control and development of fatigue resistant alloys. Corrosion fatigue is characterized by brittle failure caused by the combined effect of a fluctuating stress and a corrosive environment. The principal feature of this fracture mode is the presence of corrosion products and beach marks on the fracture surface. Corrosion fatigue can be distinguished from other environmentally induced crack mechanisms using the characteristics of the failure, described in Table 2.8 [10].

Table 2.8. Characteristics of environmentally induced cracking (SCC: stress corrosion cracking; CFC: corrosion fatigue cracking; and HIC: hydrogen-induced cracking).

Characteristics	*SCC*	*CFC*	*HIC*
Stress	Static tensile	Cyclic with tensile	Static tensile
Aqueous corrosive environment	Specific to the alloy	Any	Any
Temperature increase	Accelerates	Accelerates	Increases to room temperature, then decreases
Crack morphology	Transgranular or intergranular, branched, sharp tip	Transgranular, unbranched, blunt tip	Transgranular or intergranular, unbranched, sharp tip
Corrosion products in the crack	Absent (usually)	Present	Absent (usually)
Crack surface appearance	Cleavage, brittle like	Beach marks and/ or striations	Cleavage like
Near maximum strength level	Susceptible, but HIC often predominates	Accelerates	Accelerates

In corrosion fatigue cracking (CFC), anodic dissolution at the root of the crack is facilitated by repeated rupture of the passive film at the crack tip by fatigue processes and the

subsequent repassivation of the newly exposed metal surface. The mechanism of anodic dissolution may involve rupture of the brittle oxide layer, selective dissolution or dealloying, and/or corrosion tunnelling. The growth rate of a crack during environmentally-assisted corrosion fatigue is therefore controlled by the rate of anodic dissolution, the rupture of the oxide film, the rate of repassivation, the mass transport rate of the reactant to the dissolving surface and the flux of dissolved metal cations away from the surface. Anodic dissolution (commonly referred to as active path dissolution, slip dissolution, stress/strain enhanced dissolution or surface film rupture/metal dissolution) is defined as the CFC mechanism through which the crack growth rate is enhanced by anodic dissolution along susceptible paths that are anodic to the surrounding matrix. Such susceptible paths can include grain boundaries, strained metal at the crack tip and the interface between second-phase particles and the matrix [32-34].

In this mechanism, a slip step forms at the crack tip under fatigue loading conditions and fractures the protective surface oxide film. The freshly exposed metal surface at the crack tip reacts with the aggressive solution and partially dissolves until the crack tip repassivates and the oxide layer is restored. This process repeats during successive fatigue loading cycles as slip-steps break the oxide layer and fresh material is exposed to the corrosive environment. Factors affecting this process are mechanical variables (frequency, stress and waveform of the loading cycle), geometrical variables (crack size, weld geometry and specimen thickness), metallurgical variables (alloy chemical composition, microstructure and the strength and toughness of the material) and environmental variables (electrolyte, corrosion species concentration and temperature) [32-34].

One of the most important parameters affecting susceptibility to corrosion fatigue cracking is the loading frequency. The lower the frequency of the applied loading cycle, the higher the crack propagation rate per cycle (da/dN). Very high frequencies can completely eliminate the effect of the corrosive environment on fatigue by minimizing the interaction time between the environment and the crack tip [31,32].

As described earlier, the presence of corrosion pits induces stress concentrations responsible for promoting crack initiation. As the pit depth increases, the stress levels in the surrounding material increase. When the stress level reaches a threshold value (determined by the alloy microstructure and the corrosive environment), a crack is initiated. Closely spaced pits and longer exposure times increase the stress levels in the material surrounding the corrosion pits, promoting crack initiation [31,32]

The influence of corrosion pits on fatigue crack initiation has been reported by a number of authors for various aluminium alloys. Chlistovsky *et al.* [33] showed that the fatigue life of 7075-T651 aluminium is reduced significantly in the presence of a 3.5% NaCl corrosive environment compared to that observed in air. This reduction is attributed to the initiation of cracks from stress concentrations caused by pit formation and a combination of anodic dissolution at the crack tip and hydrogen embrittlement. A similar observation was made by Chen *et al.* [34] who studied the corrosion fatigue behaviour of aluminium 2024-T3. Their fractographic study revealed that fatigue cracks nucleated preferentially from some of the larger pits observed on the surface of the samples.

In order to study the fatigue behaviour of aluminium alloys in air and in a corrosive environment, fatigue testing has to be performed. Fatigue test results can be influenced to a significant extent by the microstructure and chemical composition of the alloy, the fabrication process, the prior heat treatment condition of the alloy, the specimen preparation, the testing machine and the procedure employed to generate fatigue and corrosion fatigue data. The following section briefly considers fatigue testing techniques.

2.7.2 Corrosion fatigue testing

Laboratory fatigue testing can be categorized as crack initiation (fatigue life) testing or crack propagation testing. During fatigue life testing, the specimen is subjected to the number of stress cycles (stress controlled, S-N) or the number of strain cycles (strain controlled, ε-N) required to initiate and subsequently grow a fatigue crack to failure. The loading mode can be direct or axial, plane bending, rotating beam, alternating torsion or a combination of these modes.

Conventionally, a fluctuating stress cycle is represented as a series of peaks and troughs connected by a sine wave (as shown schematically in Figure 2.13). The diagram in Figure 2.13 shows what is termed constant amplitude loading, with each cycle having identical values of S_{max} and S_{min}. This simple form of cyclic stress is often used in testing. A number of important parameters in fatigue testing are described in equations (2.13) to (2.17):

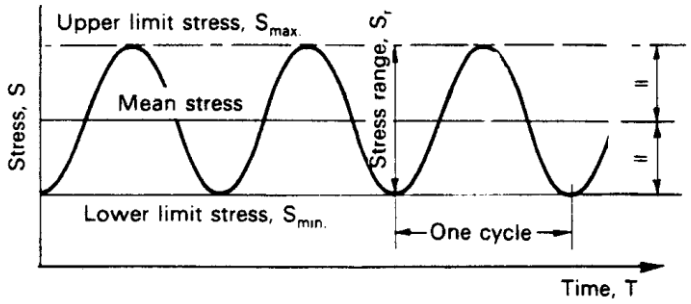

Figure 2.13. Terminology used to describe constant amplitude fluctuating stress [21].

Upper limit stress:	S_{max}	…(2.13)
Lower limit stress:	S_{min}	…(2.14)
Mean stress:	$S_m = ½ (S_{max} + S_{min})$	…(2.15)
Stress range:	$S_r = S_{max} - S_{min}$	…(2.16)
Stress amplitude:	$S_a = ½$ (stress range) $= ½ (S_{max} - S_{min})$	…(2.17)

It is necessary for general design purposes to have fatigue data for positive and negative values of S_{max}, S_{min} and S_m to cater for varying stress conditions. In this respect, a characterizing parameter known as the stress ratio, R, is often used in presenting fatigue data (equation (2.18)) [21].

$$R = \frac{\text{minimum stress}}{\text{maximum stress}} \qquad \ldots(2.18)$$

Fatigue test data is usually presented in the form of a S_a-log N_f curve, known as Wöhler's curve. A typical S_a-log N_f plot can be linearized with full log coordinates, thereby establishing the exponential law of fatigue shown in equation (2.19).

$$N (S_a)^{p} = C \qquad \ldots(2.19)$$

where: N is the number of cycles, S_a is the stress amplitude, and C and p are empirical constants.

To perform corrosion fatigue testing, an environmental chamber of glass or plastic containing the electrolyte is introduced during fatigue testing. To minimize galvanic effects, the specimen must be gripped outside of the test solution. The solution is circulated through the corrosion chamber, which is sealed to the specimen. By circulating the solution, the dissolved oxygen content, the potential, pH, temperature, and the stress and/or strain can be controlled. In this testing method, factors that influence the number of cycles to failure include the stress

amplitude (S_a), the stress ratio (R), chemical concentration of dissolved species (such H^+, O^{2-}, and other ions), the alloy properties (such as yield stress, hardness and microstructure), the waveform of the loading cycle, the test temperature and the electrolyte flow rate [33]. The effect of the corrosive environment may be eliminated at higher loading frequencies, as not enough time is allowed for the chemical reactions and mass transport kinetics required.

The weld joint geometry, the presence of weld discontinuities and the corrosion environment can significantly accelerate fatigue damage and reduce the fatigue life. The introduction of sharp stress concentrations (such as the weld toe, an uneven root profile or weld defects), the presence of tensile residual stresses associated with the weld thermal cycle and the presence of corrosion pits all contribute to the observed reduction in the fatigue life of welded samples in corrosive environments.

Based on the above discussion, the fatigue life testing method was selected for determining the effect of the weld geometry, filler metal and welding technique on the mechanical and fatigue properties and the corrosion resistance of 5083-H111 and 6061-T651 aluminium.

More detail on the experimental procedure followed during the course of this project to characterize the fatigue properties of welded and unwelded 5083-H111 and 6061-T651 aluminium is given in Chapter 3.

CHAPTER 3. EXPERIMENTAL PROCEDURE

In order to evaluate the fatigue properties of aluminium 5083-H111 and 6061-T651 in the welded and unwelded condition in the ambient atmosphere and in a 3.5% NaCl solution, the experimental procedure described below was followed during the course of this investigation.

3.1 Welding procedure

Flat aluminium plates (with initial dimensions of 2000 mm long, 120 mm wide and 6.35 mm thick) of aluminium alloys 5083-H111 and 6061-T651 (with chemical compositions as given in Table 3.1) were supplied for examination. The -H111 temper designation in the case of the non-hardenable 5083 aluminium alloy refers to material strain-hardened to a level below that required for a controlled -H11 temper (corresponding to one eighth of the full-hard condition). The -T651 temper designation refers to material solution heat treated, stress relieved by stretching and artificially aged to induce precipitation hardening. These samples were joined using semi-automatic pulsed gas metal arc welding (SA-GMAW) or fully-automatic pulsed gas metal arc welding (FA-GMAW), as shown schematically in Figure 3.1. During semi-automatic welding, the welding torch is manipulated manually by an operator, whereas in fully automatic mode, the welding torch is moved automatically using a manipulator. Prior to welding, the plates for semi-automatic welding were prepared with a double-V edge preparation, degreased with acetone and preheated to approximately 100ºC. The fully automatic welds were performed with a square edge preparation. Three different aluminium filler wires were used, namely ER4043 (Al-Si), ER5183 (Al-Mg) and ER5356 (Al-Mg). These filler wires are widely used for arc welding of aluminium alloys and were selected to provide optimal levels of deoxidation, weld metal mechanical properties and resistance to solidification cracking during welding. The typical chemical compositions of these filler metals are given in Table 3.2.

Table 3.1. Chemical compositions of the 5083-H111 and 6061-T651 aluminium plate material used in this investigation (percentage by mass).

Element %	*Al*	*Mg*	*Mn*	*Fe*	*Si*	*Cr*	*Cu*	*Zn*	*Ti*	*Others total*
5083-H111	Balance	3.66	0.39	0.40	0.22	0.14	0.04	0.03	0.02	<0.001
6061-T651	Balance	0.96	0.09	0.40	0.80	0.21	0.27	0.00	0.02	<0.01

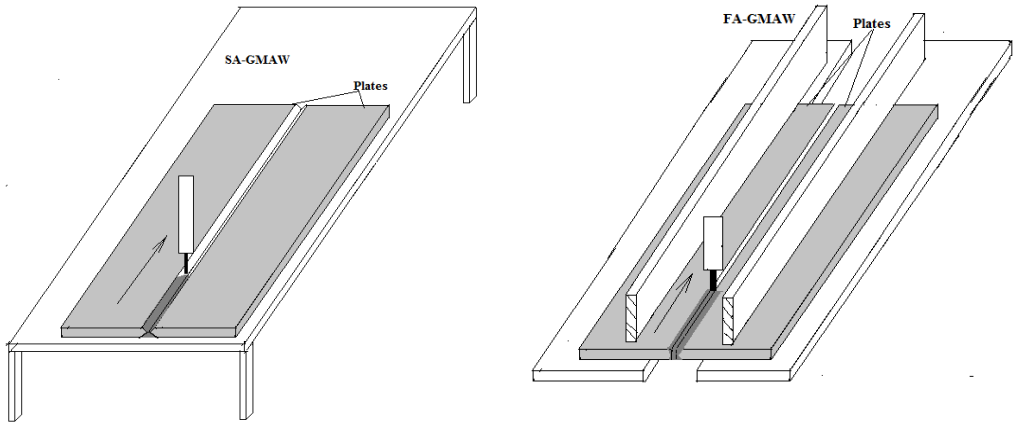

Figure 3.1. Schematic illustration of the pulsed GMAW process used in this investigation: (a) semi-automatic GMAW; and (b) fully automatic GMAW.

Table 3.2. Typical chemical compositions of the ER4043 (Al-Si), ER5183 (Al-Mg) and ER5356 (Al-Mg) filler wires used in this investigation (percentage by mass, single values represent minimum levels).

Element %	*Al*	*Mg*	*Mn*	*Fe*	*Si*	*Cr*	*Cu*	*Zn*	*Ti*	*Others total*
ER4043	Balance	0.05	0.05	0.80	4.5-6.0	Not specified	0.30	0.10	0.20	Be 0.0008%
ER5183	Balance	4.3-5.2	0.50-1.0	0.40	0.40	0.05-0.25	0.10	0.25	0.15	Not specified
ER5356	Balance	4.5-5.5	0.05-0.2	0.40	0.25	0.05-0.20	0.10	0.10	0.06-0.20	Be 0.0008%

The 5083-H111 and 6061-T651 aluminium plates were welded in the horizontal position using argon shielding gas. The welding parameters were selected to ensure pulsed spray transfer for all welds, and are given in Table 3.3. As shown in Table 3.4, similar (groups 1&2) and dissimilar (group 3) welds were produced with each of the three filler alloys.

Table 3.3. Measured pulsed gas metal arc welding process parameters.

Parameters	*Arc voltage*	*Welding current*	*Wire feed rate*	*Wire diameter*	*Nozzle to plate distance*	*Travel speed*	*Torch angle*	*Gas flow rate*
Unit	V	A	m/min	mm	mm	m/min	Degrees	l/min
SA-GMAW	24-29	133-148	6.1-7.6	1.2-1.6	15-20	0.8-1	60-80	18-33
FA-GMAW	20-23	133-148	6.1-7.6	1.2-1.6	15-20	0.4-0.6	60-80	19-28

Table 3.4. Similar and dissimilar weld metal combinations.

Group	*Base Metal*	*Filler Wire*	*Base Metal*
1	5083-H111	5356 5183 4043	5083-H111
2	6061-T651	5356 5183 4043	6061-T651
3	5083-H111	5356 5183 4043	6061-T651

3.2 Material characterization

In order to analyse the aluminium samples in the as-supplied and as-welded conditions and to quantify the material properties that may influence fatigue resistance, the microstructures of the as-received and as-welded 5083-H111 and 6061-T651 aluminium alloys were analysed, the hardness of each specimen was measured and tensile tests were performed. The corrosion resistance in a 3.5% NaCl solution was evaluated using immersion testing. More detail on these characterization tests is supplied below.

3.2.1 Microstructural analysis

The as-supplied and as-welded aluminium samples were sectioned and machined to produce rectangular fatigue and tensile specimens, with dimensions shown schematically in Figure 3.2. Samples were removed for microstructural examination in the long transverse (LT) direction, longitudinal (LD) direction and short transverse (ST) direction, as illustrated in Figure 3.2. These samples were prepared for microstructural analysis according to the requirements of ASTM standard E3-01 [35] and etched using Keller's reagent as described in ASTM standard E340-00 [36]. The metallographic samples were examined with an inverted optical microscope (with automatic image analysis using Image-Pro PLUS 5.1™ and IMAGEJ™), and a scanning electron microscope (SEM) equipped with energy dispersive X-

ray spectroscopy (EDS) capabilities. Metallographic examination was carried out on the as-supplied and welded material, and on unfatigued and fatigued specimens, to reveal the alloy and weld microstructure, to study the fracture surfaces and to detect any discontinuities (such as inclusions, microsegregation, porosity, lack of fusion and undercut). The grain sizes of the as-supplied and as-welded samples were determined using the line intercept method.

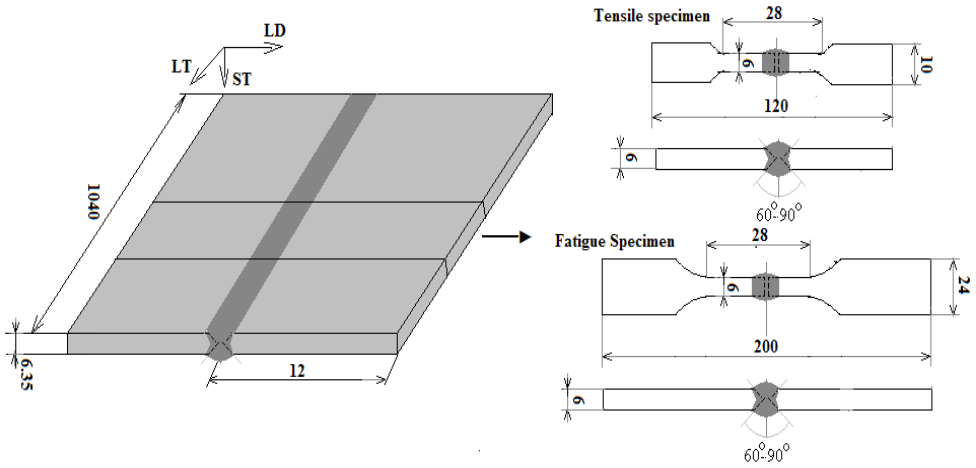

Figure 3.2. Dimensions of the tensile and fatigue specimens machined from the welded plates.

3.2.2 Hardness measurements

In order to perform hardness measurements, machined specimens (in the as-supplied and welded condition) were ground and polished using 1 µm diamond suspension, followed by final polishing using 50 nm colloidal silica, as described in ASTM standard E340-00 [36]. As-welded specimens were ground flush and polished to allow hardness measurements on the LT-LD plane (see Figure 3.2).

Vickers hardness and Vickers micro-hardness tests were performed according to the requirements of ASTM standards E384-10 [37] and E340-00 [36]. An applied load of 100 grams and a holding time of 10 seconds were employed for the micro-hardness measurements. Hardness profiles from the centreline of the weld, through the heat-affected zone (HAZ) to the unaffected base metal were measured at 0.05 to 0.1 mm intervals for welded specimens of 5083-H111 and 6061-T651 aluminium. These hardness profiles assisted in the interpretation of the weld microstructures and mechanical properties.

3.2.3 Tensile testing

Tensile tests were performed according to ASTM standard E8/E8M-09 [38], on unwelded, as-welded and dressed welded specimens. The machined specimens (as shown in Figure 3.2) were ground flush in the longitudinal direction (LD) to remove all machining marks from the unwelded specimens and to remove the weld reinforcing for the dressed weld samples. Undressed welded specimens were wet-ground without changing the weld toe geometry. An Instron™ testing machine equipped with FASTTRACK2™ software was used to axially stress specimens at a cross head speed of 3.0 mm/min. The 0.2% offset proof stress, ultimate tensile strength and percentage elongation of unwelded and welded specimens of 5083-H111 and 6061-T651 aluminium were determined for comparison and evaluation.

3.2.4 Corrosion testing

Machined specimens for corrosion testing, in the as-supplied and as-welded conditions, were ground and polished using 1 µm diamond suspension, followed by final polishing using 50

nm colloidal silica, as described in ASTM standard E340-00 [36]. These specimens were cleaned and dried to remove dirt, oil and other residues from the surfaces (as described in ASTM standard G1-03 [39]). Immersion tests were then performed in a NaCl solution using a Plexiglas corrosion cell (shown schematically in Figure 3.3) with an internal volume of 25 litres of salt water (3.5% NaCl by weight), according to the requirements of ASTM standards G31-72 [40], G44-99 [41], and G46-94 [42]. The 3.5% NaCl simulated sea water solution was prepared by dissolving 3.5±0.1 parts by weight of NaCl in 96.5 parts of distilled water. The pH of the freshly prepared solution was within the range 6.9 to 7.2. Dilute hydrochloric acid (HCl) or sodium hydroxide (NaOH) was used to adjust the pH during testing. The ambient test temperature varied from 16ºC to 27ºC. Fresh solution was prepared weekly.

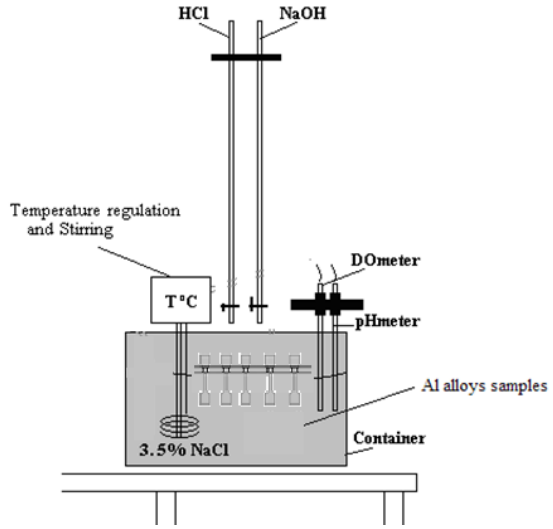

Figure 3.3. Schematic illustration of the immersion test in a 3.5% NaCl solution.

After the specified exposure time the specimens were gently rinsed with distilled water and then cleaned immediately to prevent corrosion from the accumulated salt on the specimen surface. Loose products were removed by light brushing in alcohol. As prescribed in ASTM standard G1-03 [39], the specimens were then immersed in a 50% nitric acid solution for 2 to 4 minutes, followed by immersion in concentrated phosphoric acid for another 5 minutes, to remove bulky corrosion products without dislodging any of the underlying metal. The specimens were then cleaned ultrasonically and dried.

After cleaning, the corroded specimens were examined to identify the type of corrosion that occurred and to determine the extent of pitting of the unwelded and welded 5083-H111 and 6061-T651 aluminium samples. The samples were inspected visually and microstructurally using an optical microscope and the SEM. One of the parameters used to quantify the pitting susceptibility of the samples was the pit depth, measured using the microscopic method described in ASTM standard G46-94 [42]. A single pit was located on the sample surface and centred under the objective lens of the microscope at low magnification. The magnification was increased until most of the viewing field was taken up by the pit. The focus was adjusted to bring the lip of the pit into sharp focus and the initial reading was recorded from the fine-focus adjustment. The focus was then readjusted to bring the bottom of the pit into sharp focus and the second reading taken. The difference between the initial and the final readings represents the pit depth.

For comparison purposes, photographs of the corroded surfaces and data on the pit sizes and depths were collected to evaluate the pitting susceptibility of the unwelded and welded 5083-H111 and 6061-T651 aluminium samples.

3.3 Fatigue life assessment

Specimens were fatigue tested in air and in a 3.5% NaCl simulated seawater environment using the crack initiation or fatigue life testing method. The specimen was subjected to the number of stress cycles (stress controlled, S-N) required to initiate and subsequently grow the fatigue crack to failure at various stress amplitudes.

3.3.1 Fatigue testing in air

The axial fatigue life testing method was used to determine the fatigue properties of the samples, as it takes into account the effect of variations in microstructure, weld geometry, residual stress and the presence of discontinuities.

The machined fatigue specimens (shown schematically in Figure 3.2) were ground flush and polished in the longitudinal direction to dress some of the welds and to remove all machining marks from the unwelded samples. This negated the effect of the weld geometry on the fatigue resistance of the dressed welds. Undressed welded specimens were wet-ground in such a way that the weld toe geometry was not changed. The fatigue tests were performed using a symmetrical tension-tension cycle (with a stress ratio of R = 0.125) to keep the crack open during testing. A constant frequency of 1 Hz was used for all fatigue tests and the number of cycles to failure (N_f) was recorded for each specimen. To ensure repeatability, between three and six tests were performed at each stress amplitude depending on the quality of the weld, as recommended by ASTM standard E466-07 [43]. The number of cycles recorded to failure was then statistically analysed according the recommendations of ASTM standard E739-10 [44]. The fatigue tests in ambient air were performed at temperatures ranging between 17ºC and 21°C and at relative humidity levels between 35.7 and 70.6% RH (relative humidity). INSTRON™ testing machines, equipped with calibrated load transducers, data recording systems and FASTTRACK™ software, were used to fatigue specimens to failure under amplitude stress control, as required by ASTM standard E467-08 [45]. Welded specimens were inspected before testing and any specimens with visual welding defects, such as large pores, underfill or excessive undercut, were discarded. The fatigue specimens were cleaned with ethyl alcohol prior to testing to remove any surface oil, grease and fingerprints. Care was taken to avoid scratching the finished specimen surfaces.

Following testing, the S-N_f curves (represented as stress amplitude-log N_f) were determined from the median number of cycles to failure at each stress level.

3.3.2 Corrosion fatigue testing in 3.5% NaCl simulated seawater

A corrosion environment consisting of 3.5% NaCl (by weight) in distilled water was used with the axial fatigue life testing method to investigate the effect of pitting corrosion on fatigue life. The corrosion chamber was designed and manufactured from Plexiglas (as shown in Figures 3.4 and 3.5) in such a way that the specimen was gripped outside the chamber (to prevent galvanic effects) and the chamber was sealed by rectangular rings away from the high-stress gauge section. The NaCl solution was re-circulated from 25 litre storage containers at a constant flow rate by means of a peristaltic pump.

The dissolved oxygen (DO) content, NaCl solution flow rate, pH, temperature, stress amplitude (maximum and minimum stress) and frequency were controlled, as shown in Figures 3.6 and 3.7. A frequency of 1 Hz was used to increase the interaction time between the specimen and the solution. The measured DO content varied between 7 and 8 ppm (parts per million) and the temperature between 17°C and 21°C during testing. The number of cycles to failure (N_f) was recorded for each stress amplitude (S_a) at the end of the test.

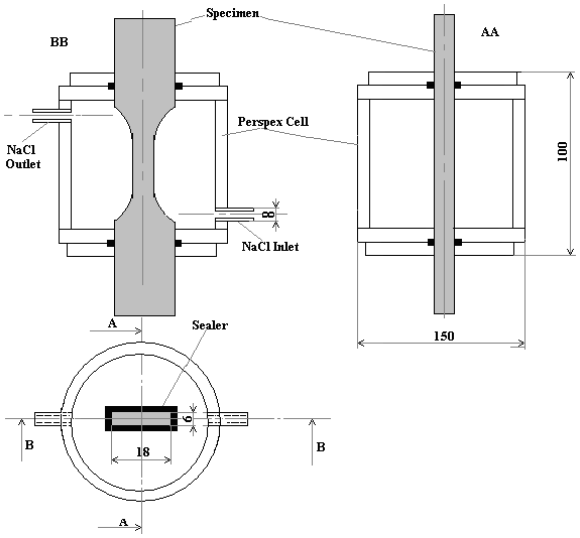

Figure 3.4. Schematic illustration of the corrosion chamber design.

Figure 3.5. The Plexiglas corrosion fatigue chamber.

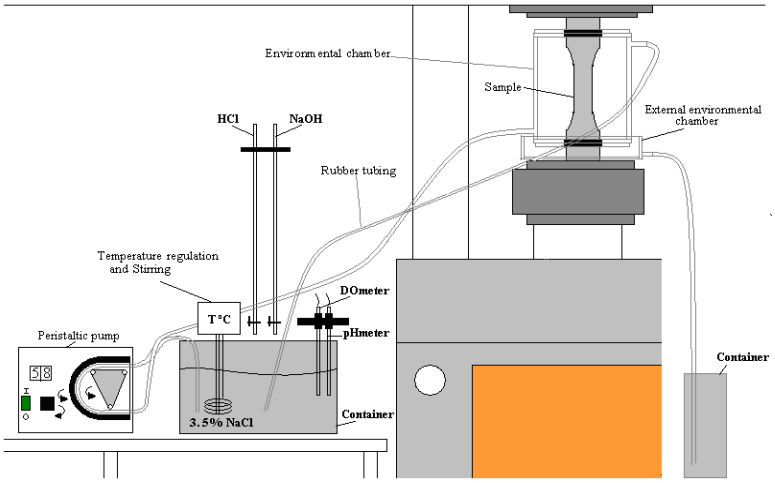

Figure 3.6. Schematic illustration of the experimental set-up used for corrosion fatigue testing in a NaCl solution.

Following testing, the S-N_f curve (represented as stress amplitude-log N_f) was determined from the median number of cycles to failure at each stress level. In order to compare the fatigue resistance in air to that in NaCl, the fatigue damage ratio, which is the ratio of the fatigue life in the 3.5% NaCl solution to the fatigue life in air ($N_{f\ NaCl}/N_{f\ Air}$), was calculated and presented as a curve of stress amplitude against $N_{f\ NaCl}/N_{f\ Air}$.

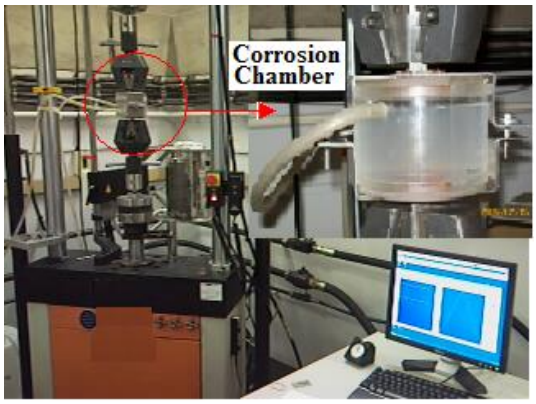

Figure 3.7. The experimental set-up used for corrosion fatigue testing in a NaCl solution.

3.4 Fractography and failure analysis

After fatigue testing, the fracture surfaces were examined using a low magnification stereo microscope and a scanning electron microscope to reveal the primary crack initiation sites and mode of fracture. This was done to correlate the fatigue and corrosion fatigue crack behaviour to the fracture features, and to compare the failure modes and cracking mechanisms in ambient air and in a NaCl environment.

The results of these experiments are considered in more detail in Chapter 4.

CHAPTER 4. RESULTS AND DISCUSSION

The major findings of this investigation are discussed below.

4.1 Metallographic examination of 5083-H111 and 6061-T651 aluminium

In order to study the microstructures of the aluminium alloys used in this investigation in the as-supplied and as-welded conditions, samples were sectioned and prepared for metallographic examination using the methods described in Chapter 3. These samples were examined using an optical microscope and a scanning electron microscope.

The microstructures of the alloys in the as-supplied condition are shown in Figures 4.1(a) and 4.1(b) for 6061-T651 and 5083-H111, respectively. Microstructural analysis revealed a coarse, elongated grain structure in the 6061-T651 base metal, as shown in Figure 4.1(a), with average grain dimensions of 141.1 µm in length (standard deviation of 70.3 µm) and 29.2 µm in width (standard deviation of 17.5 µm). Coarse second-phase particles and fine grain boundary precipitates are evident. With an average grain diameter of 24.0 µm (standard deviation of 4.19 µm), the microstructure of the 5083-H111 (see Figures 4.1(b) plate material appears more equiaxed and considerably finer than that of the 6061-T651 alloy. Coarse second-phase particles and finer grain boundary precipitates are also evident in the microstructure of 5083-H111.

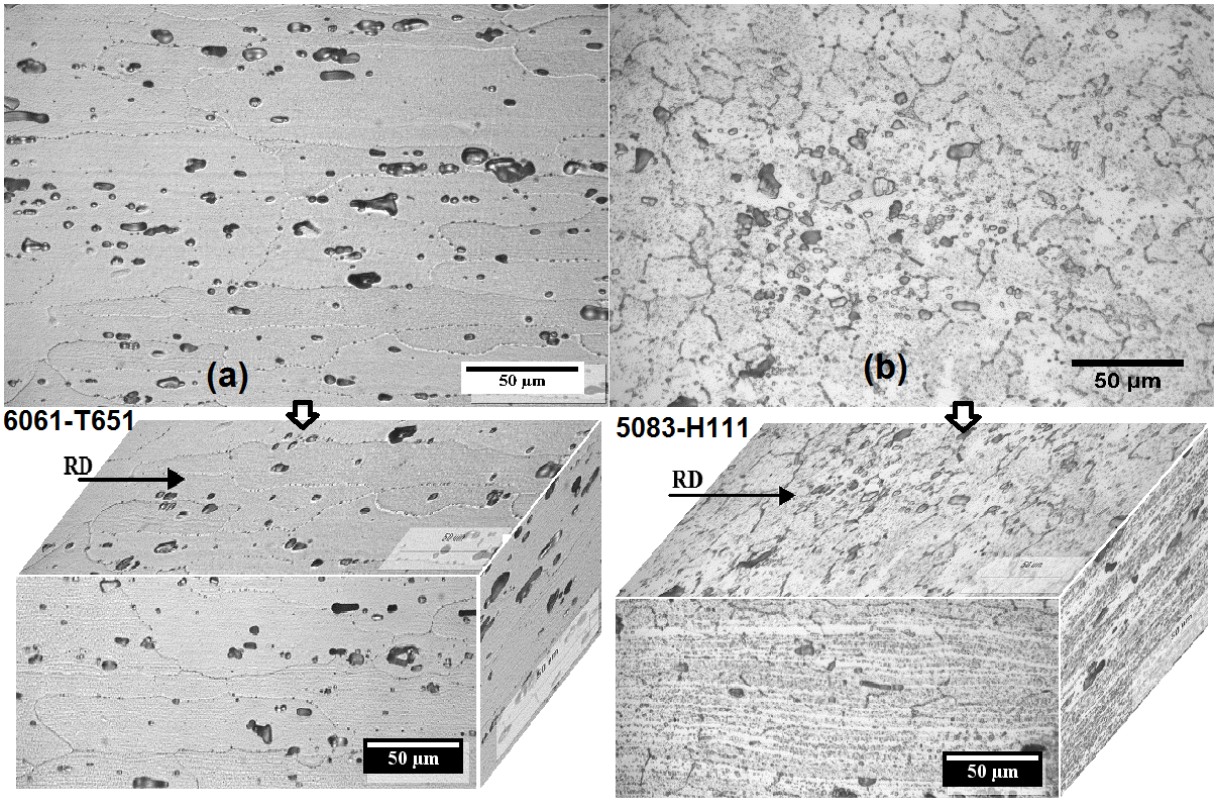

Figure 4.1. Microstructures of the aluminium alloys relative to the rolling direction (RD) in the as-supplied condition: (a) 6061-T651 aluminium; and (b) 5083-H111 aluminium.

In order to identify the second phase particles observed in the microstructures of 6061-T651 and 5083-H111 aluminium, the samples were examined using the EDS facility of a scanning

electron microscope and elemental maps were constructed in the vicinity of a number of these particles. Representative examples of these elemental maps and EDS analyses of the second-phase particles are shown in Figures 4.2 and 4.3 for 6061-T651 and 5083-H111, respectively.

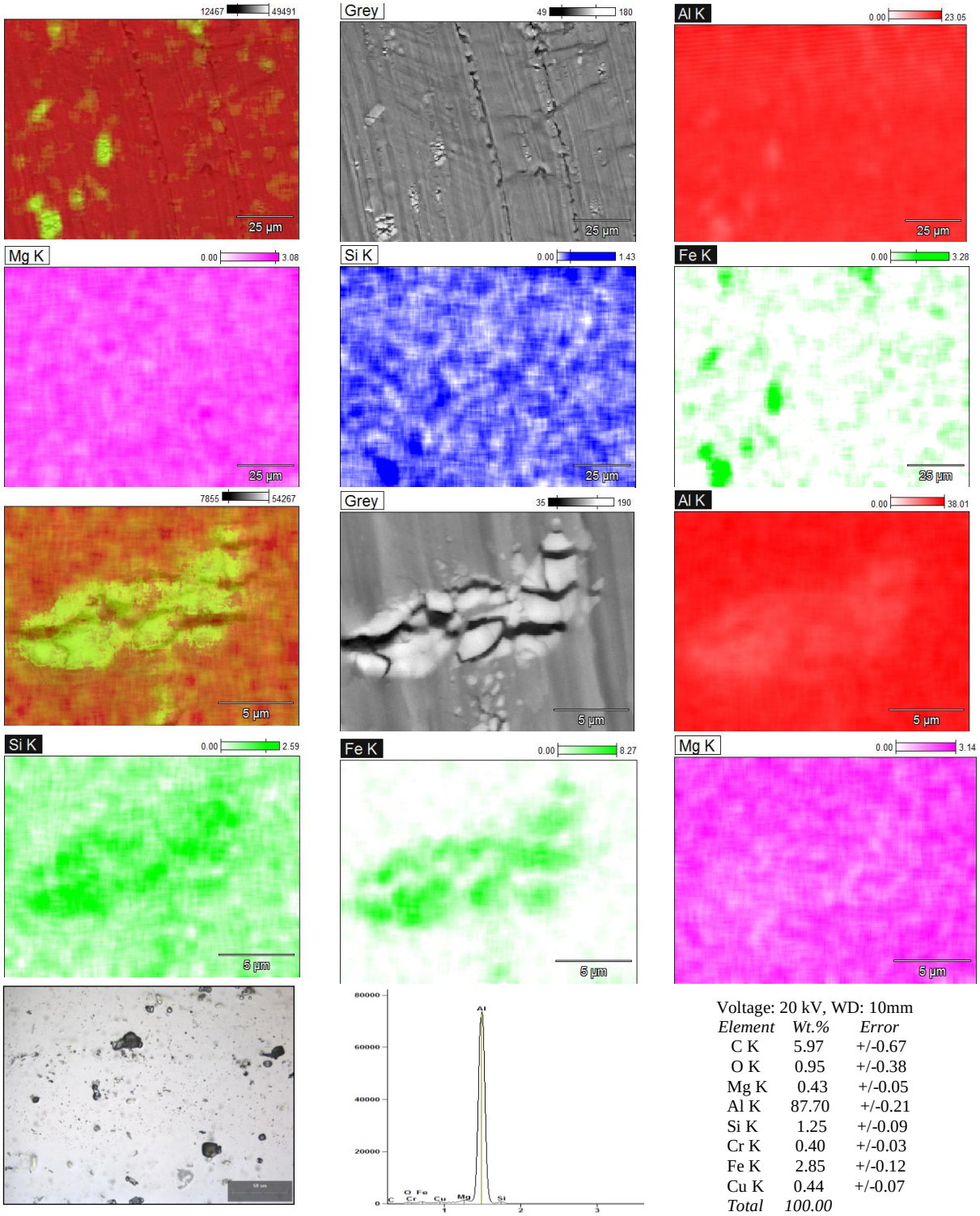

Figure 4.2. SEM-EDS analysis of second phase particles observed in the 6061-T651 matrix.

SEM-EDS analysis of the second phase particles in 6061-T651 revealed enrichment in silicon and iron (and some depletion in magnesium and aluminium). Since the strengthening Mg-Si precipitates in correctly heat treated 6061 are unlikely to be visible at the magnifications used,

the presence of these coarse precipitates may suggest incomplete dissolution during the solution annealing stage of the precipitation heat treatment. The SEM-EDS elemental maps in Figure 4.3 suggest the presence of two types of precipitates in 5083-H111. Coarse manganese-rich particles (depleted in magnesium and aluminium and slightly enriched in silicon) were identified as the Al_6Mn intermetallic phase, whereas smaller particles that appear to be enriched in magnesium and silicon were identified as an Al-Mg-Si intermetallic phase.

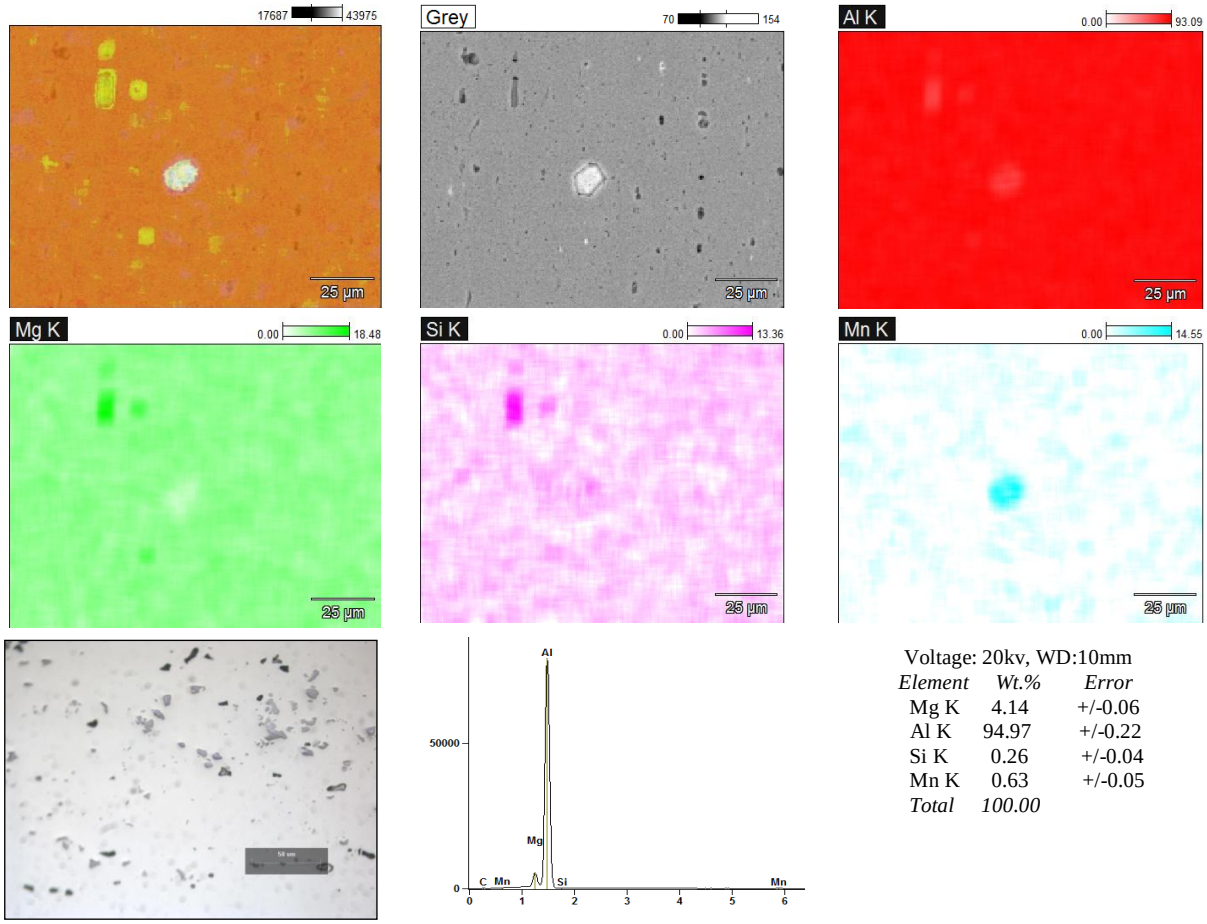

Figure 4.3. SEM-EDS analysis of second phase particles observed in 5083-H111 in the as-supplied condition.

Typical macrostructures of welded cross-sections are shown in Figures 4.4(a) to (d). The semi-automatic gas metal arc welds, Figure 4.4(a) and (b), are full penetration joints welded from both sides. Considerable weld reinforcement, gas porosity and some lack-of-fusion type defects are evident in the macrographs. The fully automatic welds, Figure 4.4 (c) and (d), are full penetration joints welded from one side only, with smooth cap profiles and some evidence of misalignment, undercut and overfill (Figure 4.4(d)) at the weld root. Microstructural examination of the welds confirmed the presence of porosity in the semi-automatic welds of 5083-H111 aluminium alloy, and also revealed some lack-of-fusion type defects and microcracks in the weld metal, as shown in Figure 4.5(a) to (d). Micrographs of a fully automatic pulsed gas metal arc weld in 6061-T651 aluminium, shown in Figures 4.6(a) to (d), reveal some gas pores (although generally smaller than the pores observed in the semi-automatic welds) and a number of small microcracks. Although all samples with visual welding defects were omitted from further mechanical testing, samples with internal flaws

and defects were not excluded. It is therefore likely that any internal defects in the tested samples may have affected the tensile and fatigue behaviour of the samples.

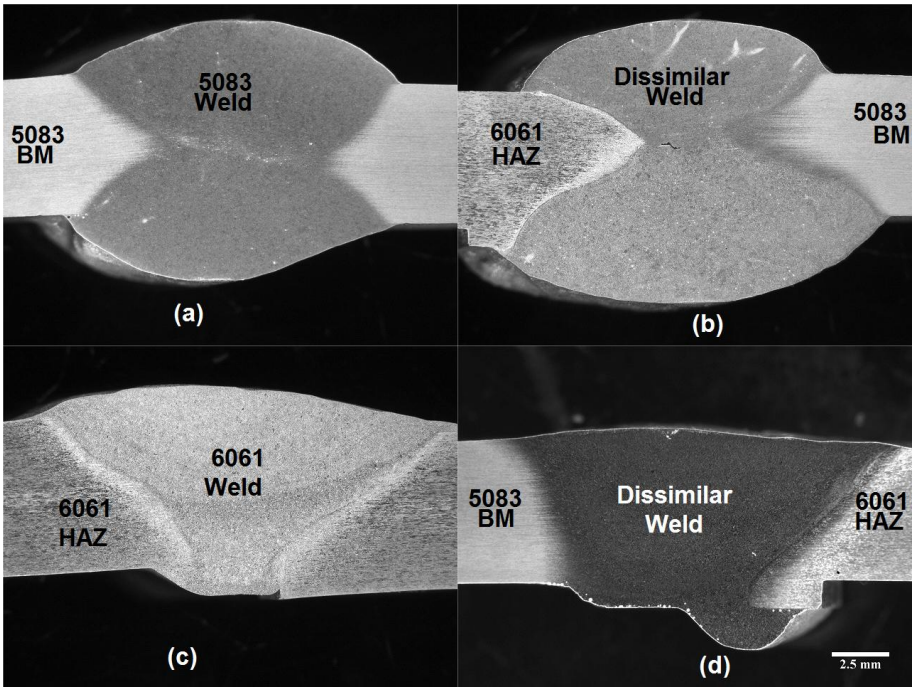

Figure 4.4. Representative weld macrographs: (a) Semi-automatic weld in 5083-H111; (b) semi-automatic dissimilar weld joining 5083-H111 and 6061-T651; (c) fully automatic weld in 6061-T651; and (d) fully automatic dissimilar weld joining 5083-H111 and 6061-T651 aluminium.

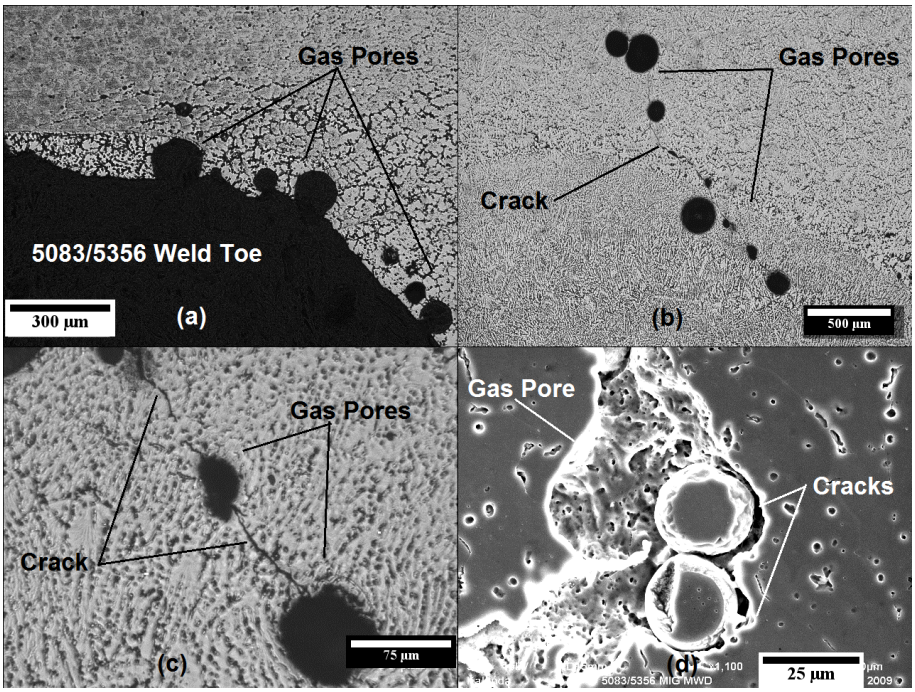

Figure 4.5. Discontinuities observed in a semi-automatic pulsed gas metal arc weld (5083/ER5356): (a) gas pores, (b)-(d) gas pores and cracks in the weld metal.

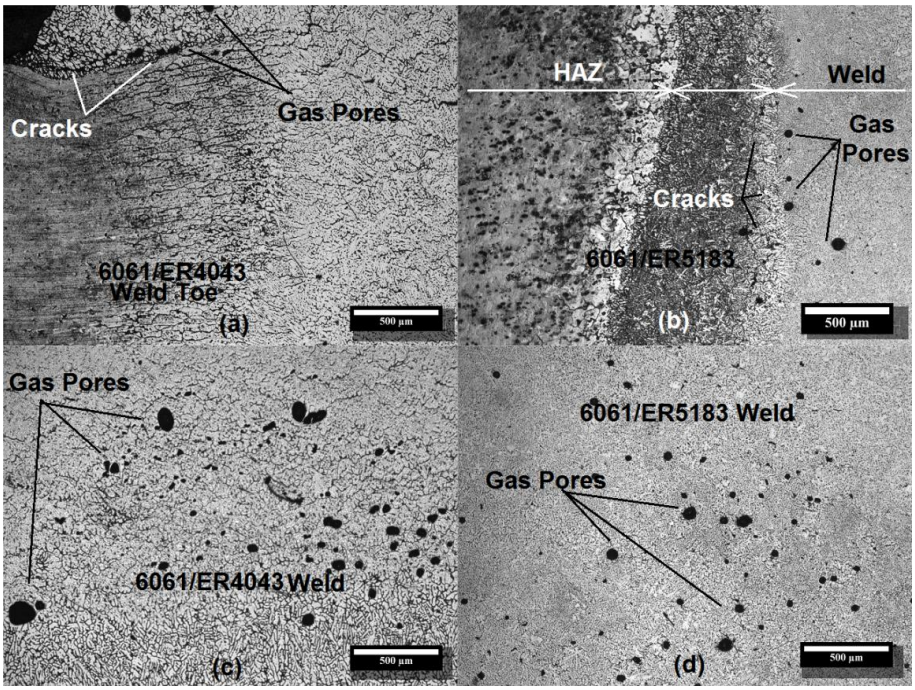

Figure 4.6. Discontinuities observed in a fully automatic pulsed gas metal arc weld (representative of 6061/ER4043 and 6061/ER5183 welds).

The heat-affected zone (HAZ) adjacent to the weld fusion line in 6061-T651 was found to consist of coarse, equiaxed grains with an average grain diameter of 100.0 µm (standard deviation of 42.5 µm) close to the fusion line (as shown in Figure 4.7(a)). Grain boundary films of second phase particles, as well as the presence of several coarse, isolated precipitates, signify uncontrolled precipitation and overageing during the weld thermal cycle. The HAZ of the 5083-H111 welds (shown in Figure 4.7(b)) has a finer grain size than the 6061-T651 HAZ, with coarse second-phase particles, predominantly on grain boundaries. The HAZ grain structures of the semi-automatic welds appear coarser than those of the fully-automatic welds.

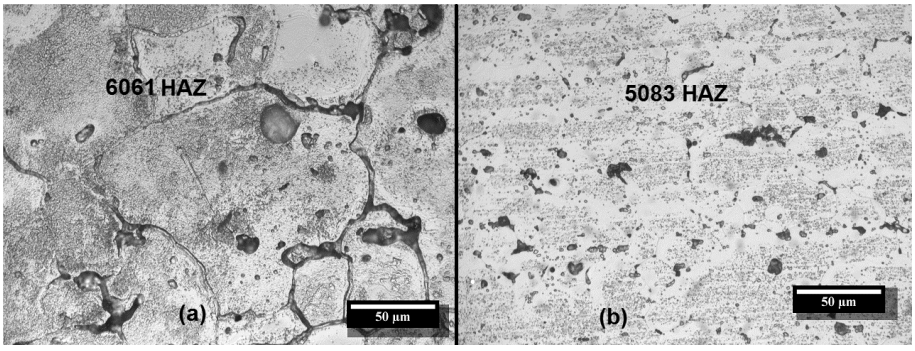

Figure 4.7. Representative optical micrographs of the heat-affected zone microstructures adjacent to the fusion line of (a) 6061-T651; and (b) 5083-H111 aluminium.

Representative optical micrographs of the weld metal of 6061-T651 welded with ER5356, ER5183 and ER4043 filler wire are shown in Figures 4.8(a) to (c). The weld microstructures appear dendritic in structure, characterized by an aluminium-rich matrix and a second phase, present as interdendritic films in the case of ER4043, and as more spherical precipitates in the case of ER5356 and ER5183. Similar weld metal microstructures were observed in 5083-H111 and in dissimilar 6061/5083 joints, welded with the three different filler wires (as

shown in Figures 4.9 and 4.10). The semi-automatic pulsed gas metal arc welds generally displayed coarser grain structures than the fully automatic pulsed gas metal arc welds.

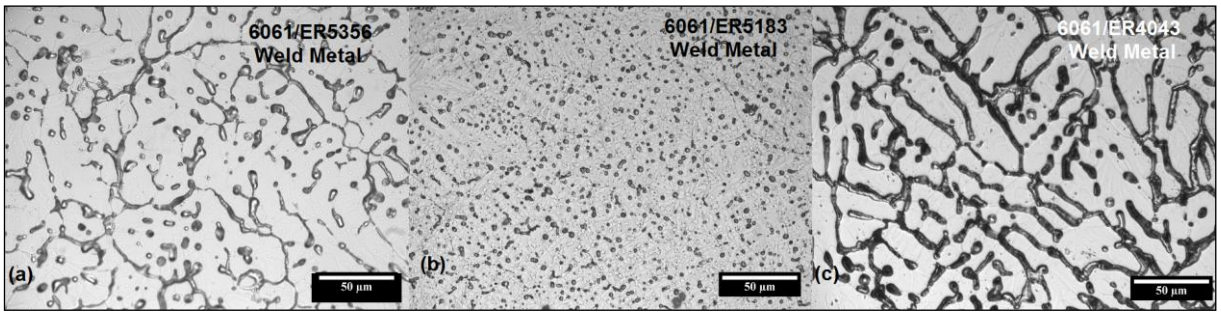

Figure 4.8. Typical micrographs of the weld metal microstructures of: (a) 6061/ER5356; (b) 6061/ER5183; and (c) 6061/ER4043.

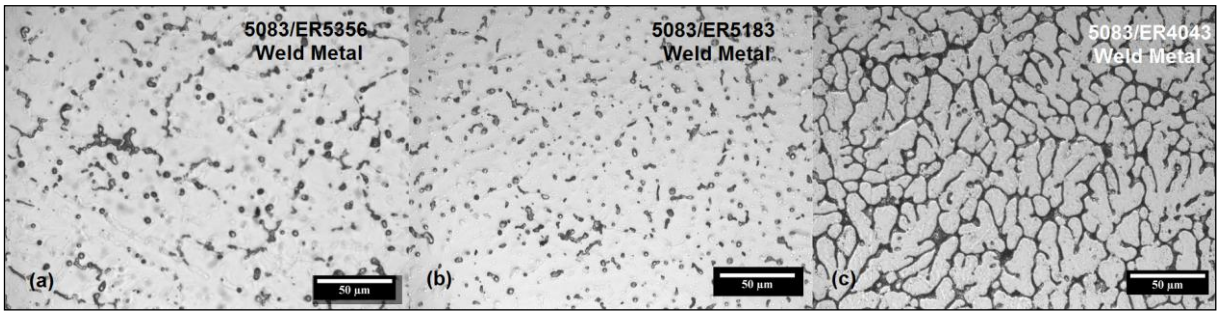

Figure 4.9. Typical micrographs of the weld metal microstructures of: (a) 5083/ER5356; (b) 5083/ER5183; and (c) 5083/ER4043.

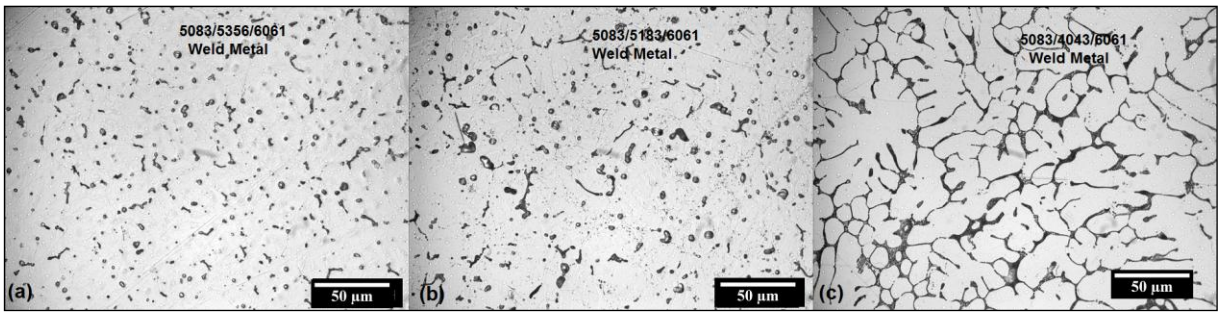

Figure 4.10. Typical micrographs of the weld metal microstructures of: (a) 5083/ER5356/6061; (b) 5083/ER5183/6061; and (c) 5083/ER4043/6061 dissimilar welds.

In order to identify the second phase particles observed in the microstructures of the welds, the weld metal of each welded joint was examined using the SEM-EDS technique and elemental maps were constructed to show the distribution of the chemical elements. A representative example of such an elemental map is shown in Figure 4.11 for a weld performed using ER5356 filler metal. These figures suggest that ER5356 welds contain second phase particles and grain boundary regions enriched in iron and magnesium, and slightly depleted in aluminium. In welds deposited using magnesium-alloyed ER5183 filler wire, second phase particles appear to be enriched mainly in magnesium and aluminium (Figure 4.12).

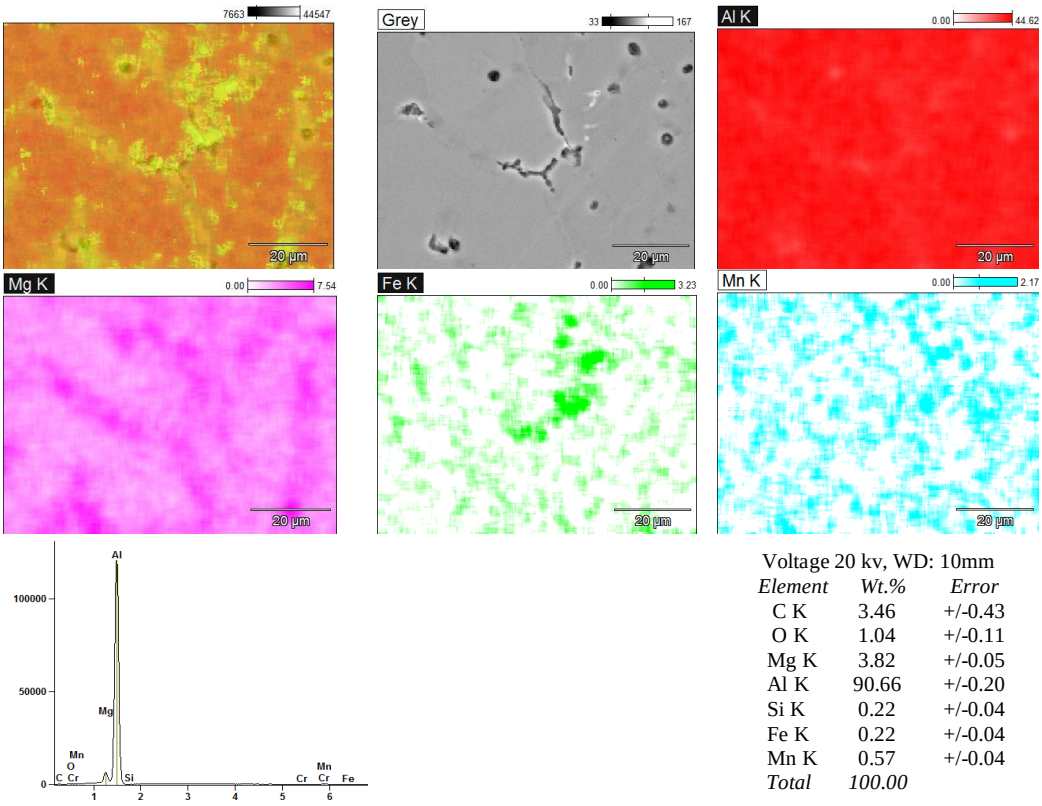

Voltage 20 kv, WD: 10mm

Element	*Wt.%*	*Error*
C K	3.46	+/-0.43
O K	1.04	+/-0.11
Mg K	3.82	+/-0.05
Al K	90.66	+/-0.20
Si K	0.22	+/-0.04
Fe K	0.22	+/-0.04
Mn K	0.57	+/-0.04
Total	*100.00*	

Figure 4.11. Typical SEM-EDS analysis of second phase particles observed in a weld performed using ER5356 filler wire.

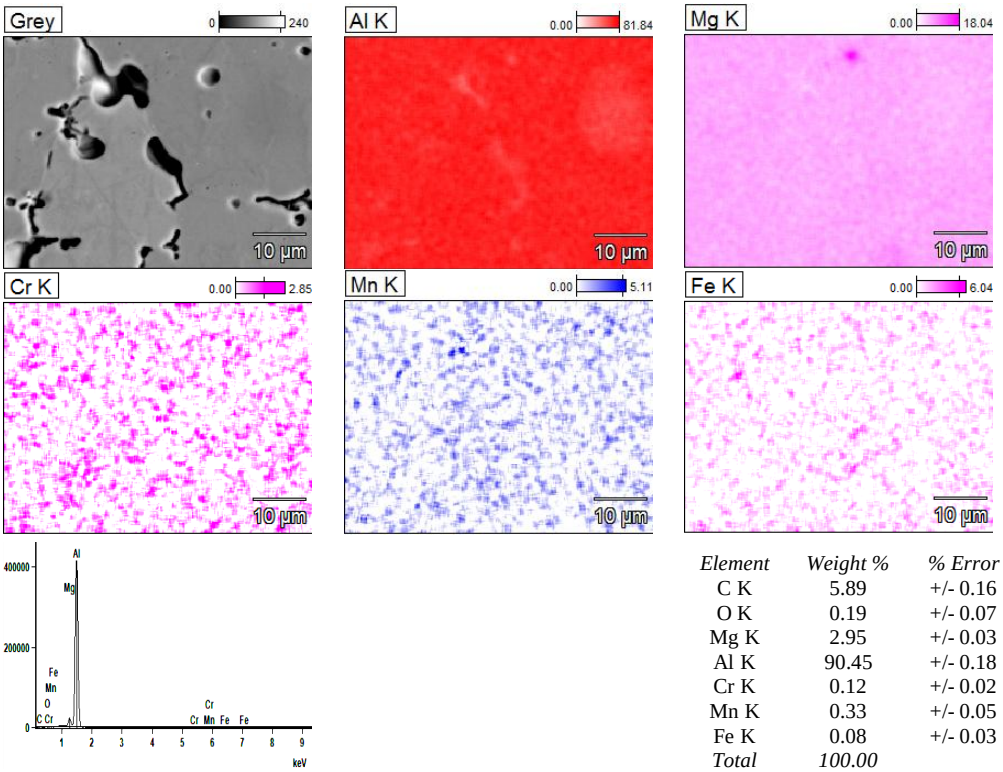

Element	*Weight %*	*% Error*
C K	5.89	+/- 0.16
O K	0.19	+/- 0.07
Mg K	2.95	+/- 0.03
Al K	90.45	+/- 0.18
Cr K	0.12	+/- 0.02
Mn K	0.33	+/- 0.05
Fe K	0.08	+/- 0.03
Total	*100.00*	

Figure 4.12. Typical SEM-EDS analysis of second phase particles observed in a weld performed using ER5183 filler wire.

As shown in Figure 4.13, the interdendritic component of weld metal deposited using ER4043 filler wire appears to consist of a fine silicon-rich eutectic. Isolated magnesium-rich particles are also evident.

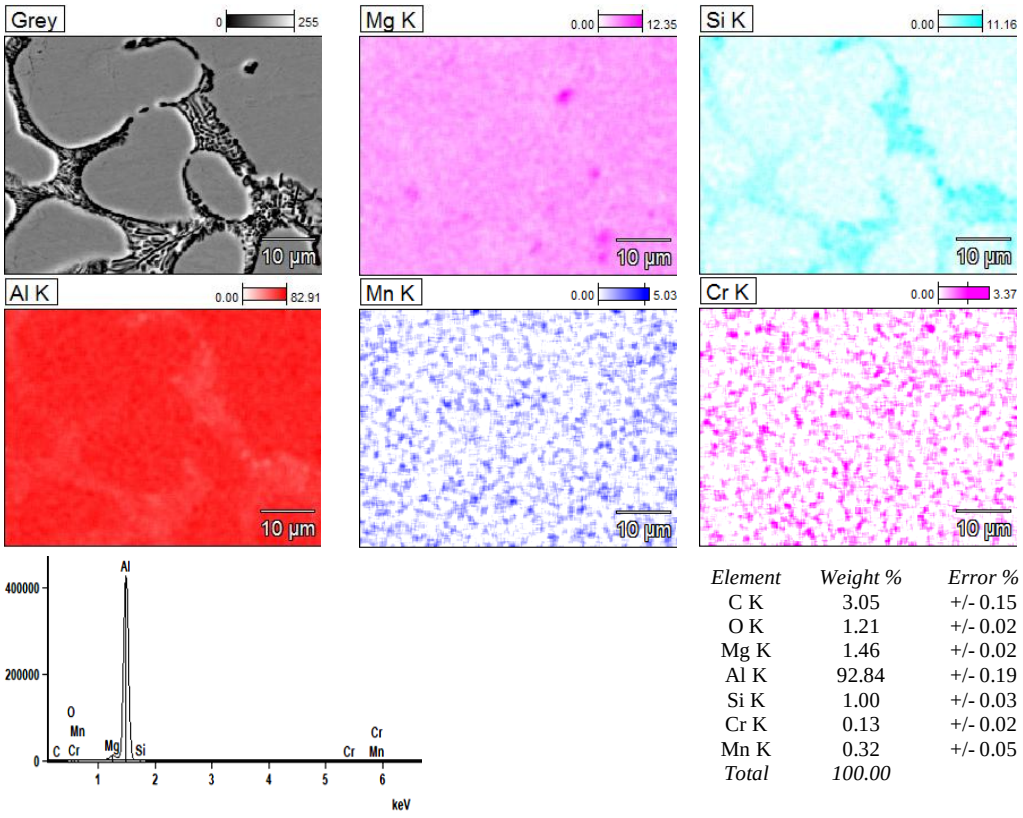

Element	*Weight %*	*Error %*
C K	3.05	+/- 0.15
O K	1.21	+/- 0.02
Mg K	1.46	+/- 0.02
Al K	92.84	+/- 0.19
Si K	1.00	+/- 0.03
Cr K	0.13	+/- 0.02
Mn K	0.32	+/- 0.05
Total	*100.00*	

Figure 4.13. Typical SEM-EDS analysis of second phase particles observed in a weld performed using ER4043 filler wire.

4.2 Micro-hardness evaluation of 5083-H111 and 6061-T651 welds

The average hardness values of aluminium 6061-T651 and 5083-H111 in the as-supplied condition are shown in Table 4.1. Aluminium 6061-T651 has a slightly higher hardness than 5083-T651. This can be attributed to the difference in prevailing strengthening mechanisms in these alloys. Magnesium-alloyed 5083-H111 aluminium can be strain hardened, but is only marginally responsive to precipitation strengthening. The 6061-T651 alloy responds well to precipitation strengthening, and was further strengthened by stretching in the –T651 temper condition. Micro-hardness measurements revealed higher hardness values in the region of second phase intermetallic particles, with hardness values in excess of 327 HV measured on precipitates in 6061-T651, and even higher values (a maximum of 794 HV) measured on inclusions in 5083-H111.

Table 4.1. Vickers micro-hardness of the aluminium alloys in the as-supplied condition.

Material	*Average Vickers micro-hardness [HV]*
5083-H111	91.8 ± 13.2
6061-T651	111.5 ± 10.4

Micro-hardness profiles, measured at 0.05 mm intervals over a total distance of 4 mm in the as-supplied material, shown in Figure 4.14, confirmed localized variations in hardness, influenced by experimental technique and the presence of coarse second phase particles within the matrix of both alloys.

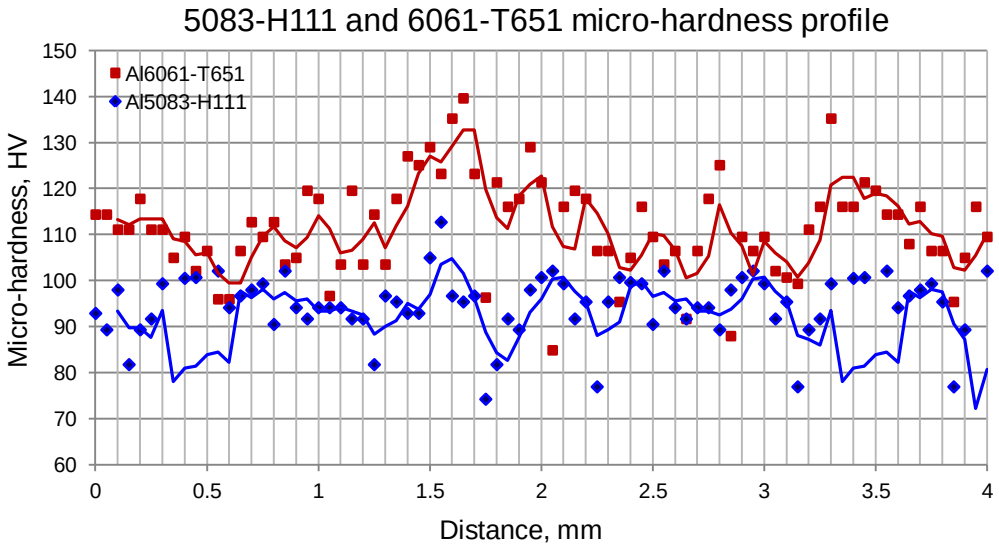

Figure 4.14. Micro-hardness profiles measured over a total distance of 4 mm in the as-supplied 5083-H111 and 6061-T651 material.

Micro-hardness profiles across fully automatic gas metal arc welds in 6061-T651 aluminium, joined using ER4043 filler wire and ER5183 filler wire are shown in Figures 4.15 and 4.16, respectively. A similar hardness profile was measured in welds performed using ER5356 filler wire. A significant reduction in hardness is evident in the heat-affected zone adjacent to the weld. This region experiences high temperatures during the weld thermal cycle, resulting in recrystallization and partial dissolution of second phase particles close to the fusion line, and varying degrees of overageing of strengthening precipitates in the heat-affected zone. The slightly lower hardness of the weld metal can be attributed to the lower hardness of the non-matching magnesium-alloyed welding consumable.

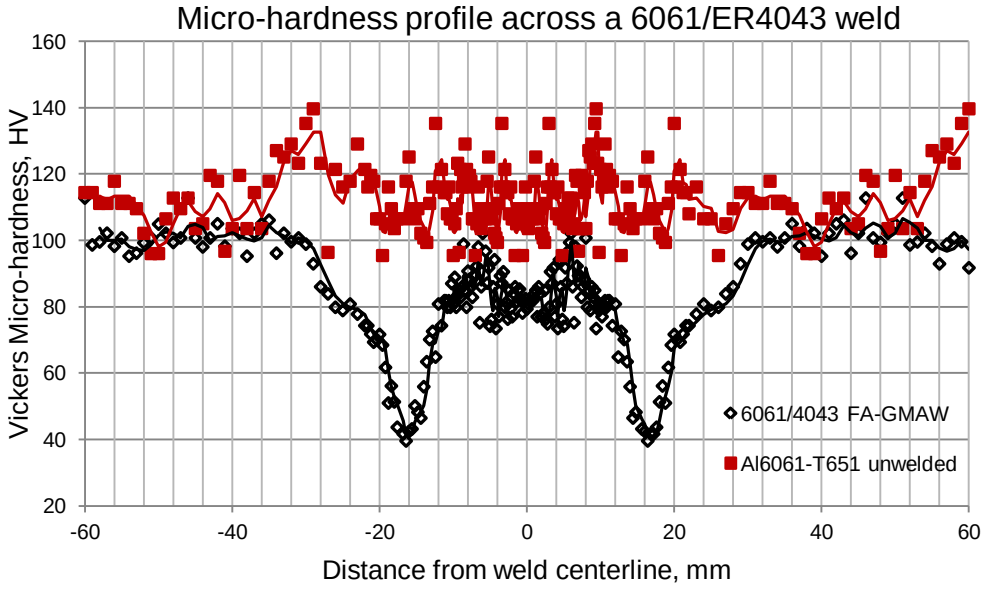

Figure 4.15. Micro-hardness profile across a semi-automatic pulsed gas metal arc weld in 6061-T651 aluminium welded with ER4043 filler wire. The heat-affected zone is distinguished by hardness troughs on either side of the weld metal, with the fusion line located approximately 10 mm from the weld centreline.

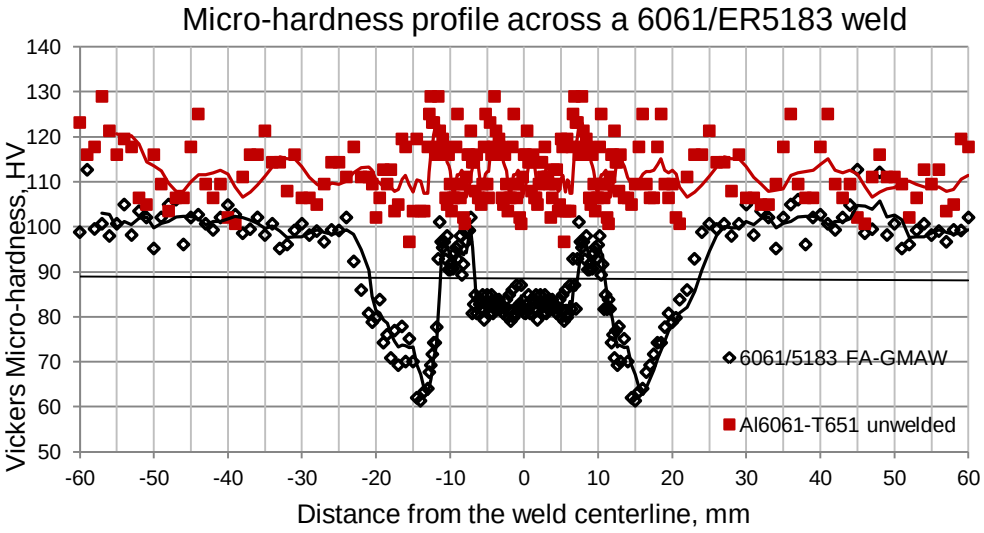

Figure 4.16. Micro-hardness profile across a semi-automatic pulsed gas metal arc weld in 6061-T651 aluminium welded with ER5183 filler wire. The heat-affected zone is distinguished by hardness troughs on either side of the weld metal, with the fusion line located approximately 10 mm from the weld centreline.

Figures 4.17 and Figure 4.18 display micro-hardness profiles across fully automatic gas metal arc welds in 5083-H111 aluminium performed using ER5356 and ER4043 filler wire, respectively. The measured hardness across the 5083/ER5356 weld is more uniform than in the case of welds in 6061-T651, with a low weld metal hardness due to the non-matching consumable used and a significant reduction in the heat-affected zone hardness due to recrystallization, overageing and grain growth during the weld thermal cycle. A similar trend was observed for the ER5183 and ER4043 filler metals. The lowest hardness values were observed within the weld metal of both the semi-automatic and fully automatic welds produced using ER5356 or ER4043 filler wire. The semi-automatic welds displayed lower heat-affected zone hardness values than the fully automatic welds, regardless of the base metal and filler wire used.

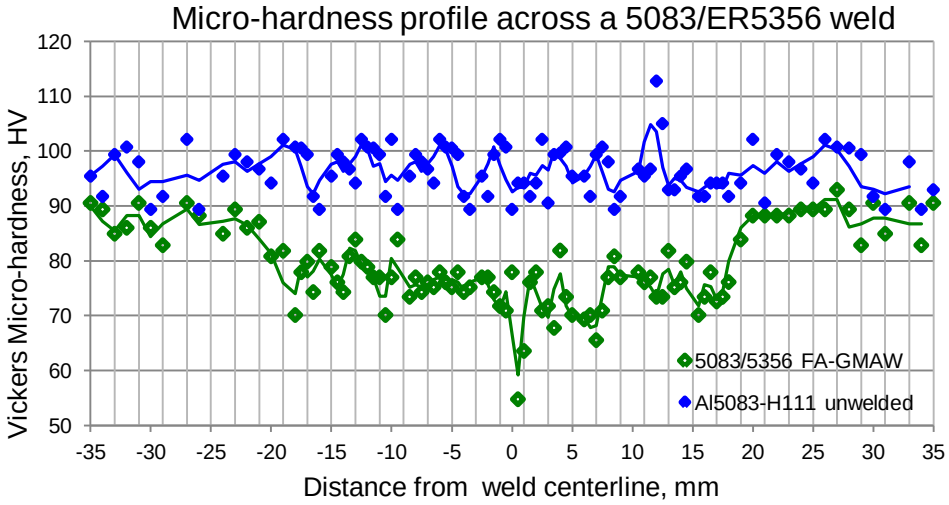

Figure 4.17. Micro-hardness profile across a semi-automatic pulsed gas metal arc weld in 5083-H111 aluminium welded with ER5356 filler wire. The fusion line was located approximately 8 mm from the weld centreline and the heat-affected zone was approximately 12 mm wide.

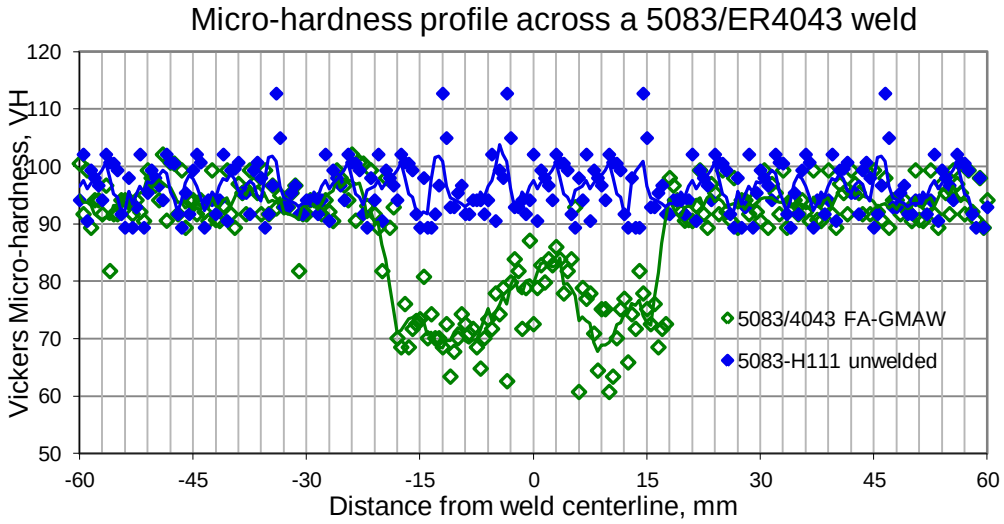

Figure 4.18. Micro-hardness profile across a semi-automatic pulsed gas metal arc weld in 5083-H111 aluminium welded with ER4043 filler wire. The heat-affected zone was approximately 12 mm wide.

A micro-hardness profile across a dissimilar metal weld of 5083-H111 and 6061-T651 (joined using ER5183 filler wire) is shown in Figure 4.19. The hardness appears more uniform on the 5083-H111 side of the weld. The hardness reduction in the heat-affected zone of the 6061-T651 alloy is again evident, indicative of grain coarsening, overageing and partial dissolution of strengthening precipitates in the heat treated aluminium. Due to dilution effects, the weld metal on the 6061-T651 side of the joint appears slightly harder than on the 5083-H111 side.

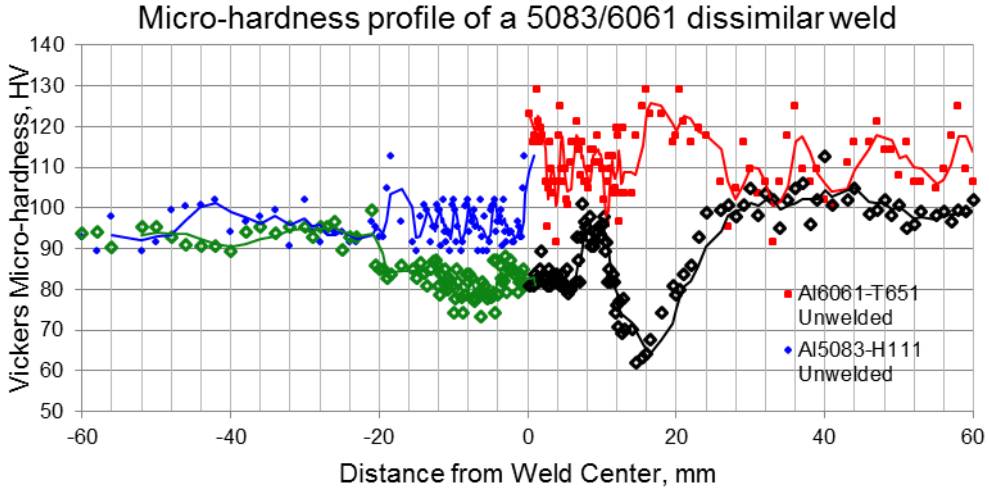

Figure 4.19. Micro-hardness profile across a fully automatic dissimilar metal weld joining 5083-H111 and 6061-T651 (ER5183 filler wire).

4.3 Tensile properties of 5083-H111 and 6061-T651 aluminium

4.3.1 Tensile properties in the as-supplied condition

As shown in Figure 4.20, the artificially aged and stretched aluminium 6061-T651 displayed higher tensile and yield strength values compared to those of the 5083-H111 magnesium-alloyed aluminium. Since the 5083-H111 alloy does not respond well to precipitation hardening and was only strengthened to a limited extent by strain hardening, the lower strength of the magnesium-alloyed material was expected. The lower ductility of the 6061-

T651 material, compared to that of 5083-H111, is consistent with the higher strength of the 6061-T651.

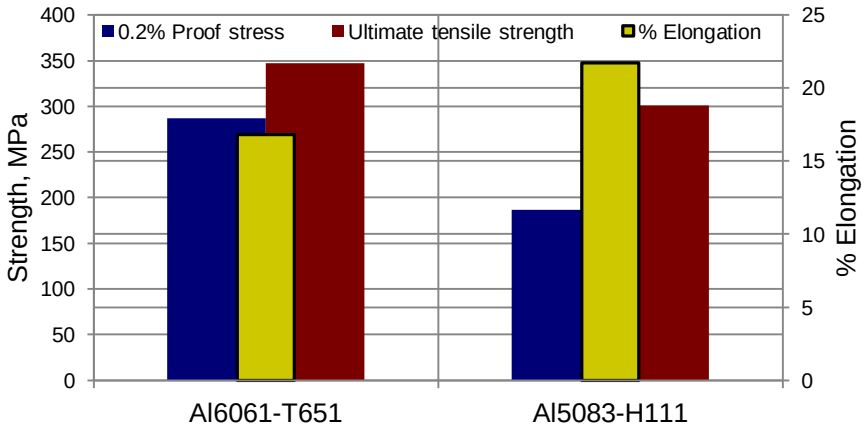

Figure 4.20. Tensile properties of 5083-H111 and 6061-T651 aluminium in the as-supplied condition.

During axial tensile testing, the crack path in both 6061-T651 and 5083-H111 followed coarse second phase particles within the matrix, as illustrated in Figures 4.21(a) and (b). Both alloys fractured in a ductile manner, as evidenced by microvoid coalescence (dimples) observed around coarse precipitates and second phase particles on the fracture surface (Figures 4.21(c) and (d)).

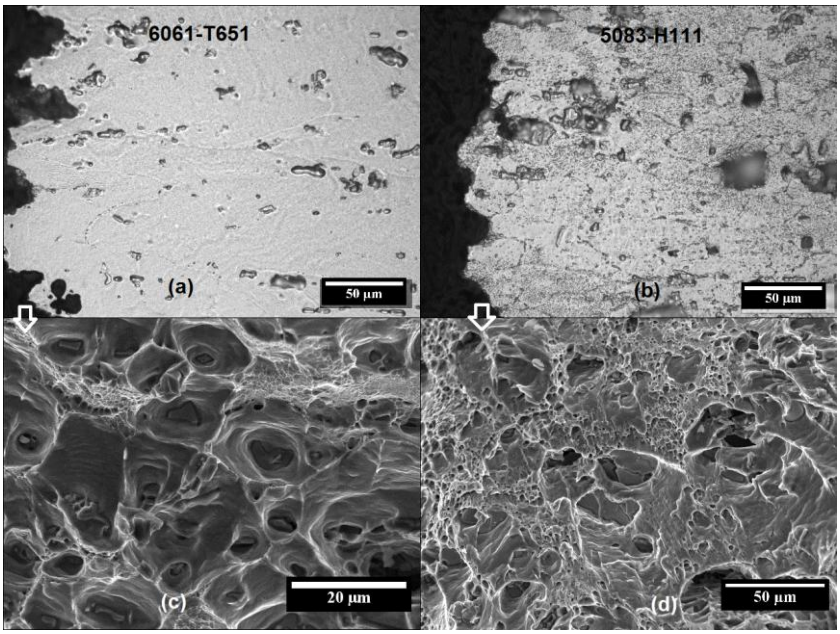

Figure 4.21. Tensile fracture of the as-supplied material: (a) fracture path in 6061-T651 aluminium; (b) fracture path in 5083-H111 aluminium; (c) microvoid coalescence on the fracture surface of 6061-T651; and (d) microvoid coalescence on the fracture surface of 5083-H111.

4.3.2 Tensile properties of 5083-H111 welds

The transverse tensile properties of 5083-H111 aluminium welded using ER5356, ER5183 and ER4043 filler wire are given in Figures 4.22, 4.23 and 4.24, respectively. As illustrated by representative examples shown in Figures 4.25 to 4.27, all the fully dressed welds in aluminium 5083-H111 (regardless of filler metal or welding mode used) failed in the weld metal. As such, the measured tensile properties reflect those of the consumables used. As shown in Figures 4.17 and 4.18, the hardness across welds in 5083-H111 is fairly uniform,

with a moderate reduction in hardness in the weld metal. This reduction in hardness most likely prompted failure in this region during tensile testing. Any discontinuities in the weld metal, such as gas porosity or lack-of-fusion type defects, will also affect the measured tensile properties. The ultimate tensile strength (UTS) of fully automatic dressed 5083-H111 welds performed using ER5356 filler wire was very similar to that of the base metal, with ER5183 and ER4043 generally yielding lower strength values due to the inherently lower strength levels of the consumables. Figures 4.22 to 4.24 also indicate that the ultimate tensile strength (UTS) values of fully automatic welds are consistently higher than those of semi-automatic welds. This can most likely be attributed to the higher incidence of porosity and welding defects observed in the semi-automatic welds (as shown in Figure 4.5). The strength values of fully dressed welds in 5083-H111 using ER5356 filler wire, shown in Figure 4.22, are significantly higher than those of undressed welds, emphasising the detrimental effect of geometrical stress concentrations (at the weld toe and root) and weld defects (such as undercut) on the measured tensile properties. Undressed welds consistently failed in the heat-affected zone at the weld toe or root. The tensile fractures (shown in Figure 4.25 and 4.26) and scanning electron micrographs of the weld metal fracture surfaces (shown in Figure 4.27) confirm a predominantly ductile failure mode in the ER5356 and ER5183 welds, with mixed mode failure along the interdendritic silicon-rich eutectic regions in the ER4043 weld metal.

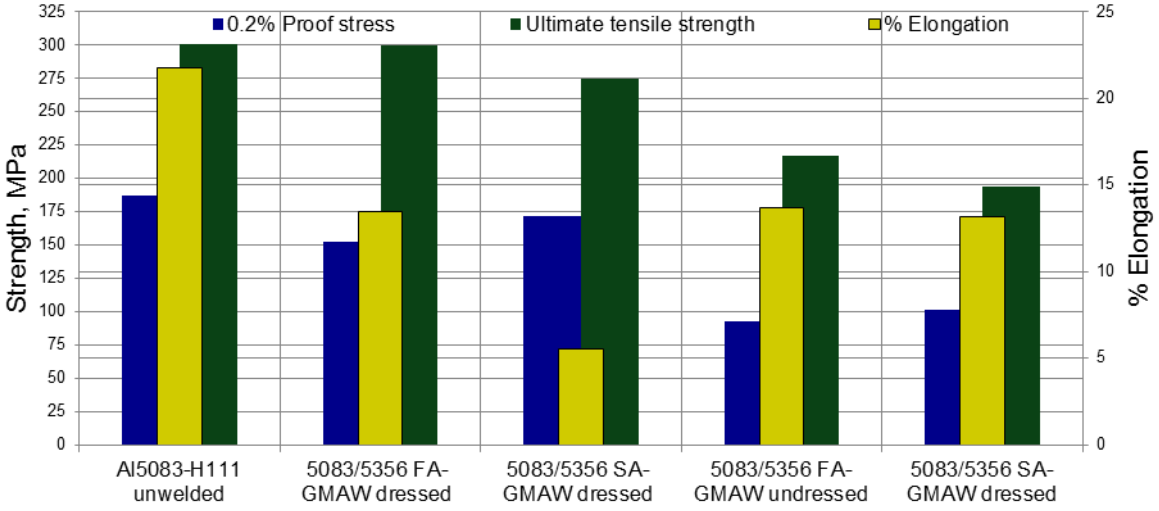

Figure 4.22. Tensile properties of 5083-H111/ER5356 welds.

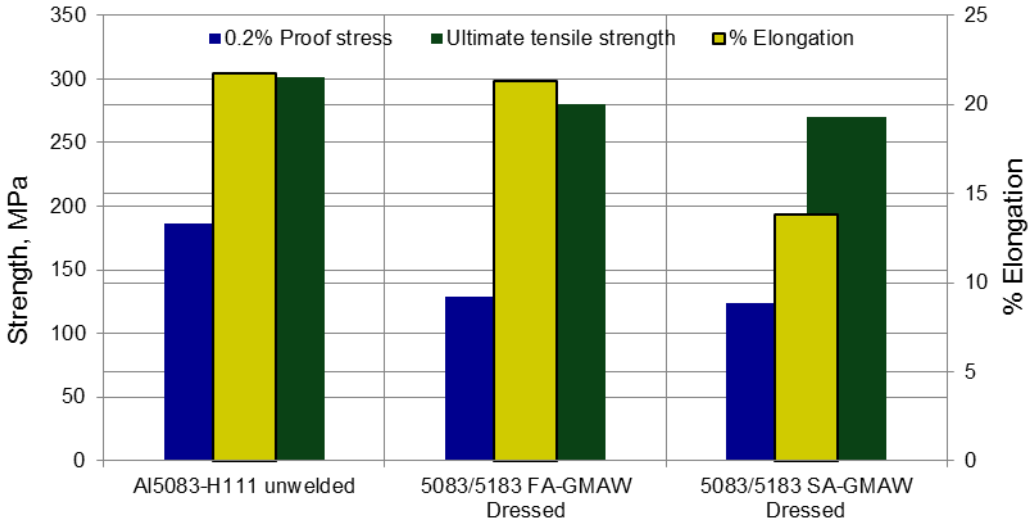

Figure 4.23. Tensile properties of 5083-H111/ER5183 welds.

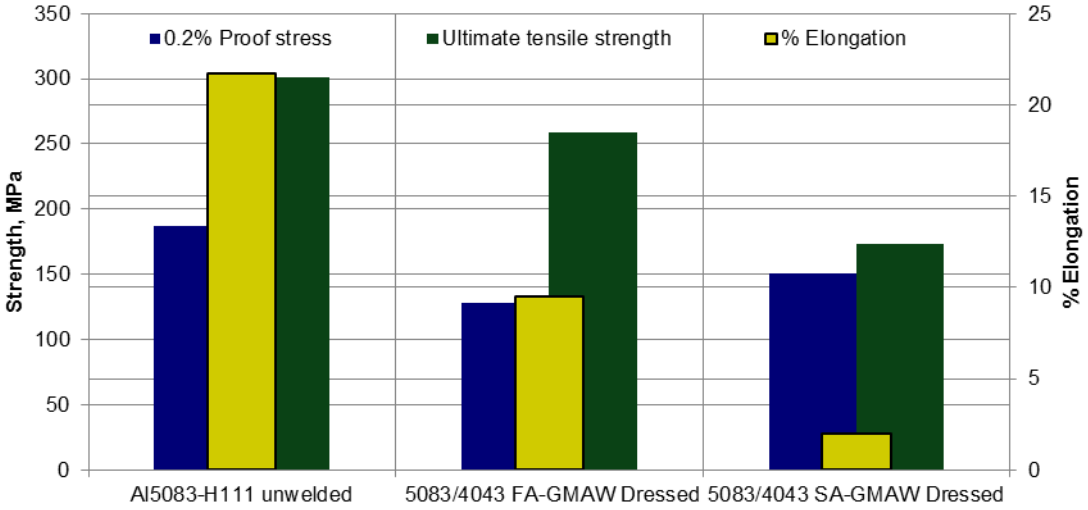

Figure 4.24. Tensile properties of 5083-H111/ER4043 welds.

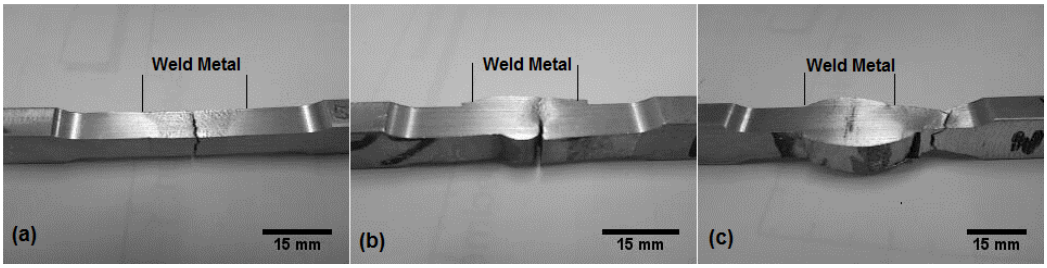

Figure 4.25. Representative photographs of the tensile fractures observed in 5083-H111 welded using ER5356, ER5183 and ER4043 filler wires: (a) fully dressed automatic weld; (b) undressed fully automatic weld; and (c) undressed semi-automatic weld.

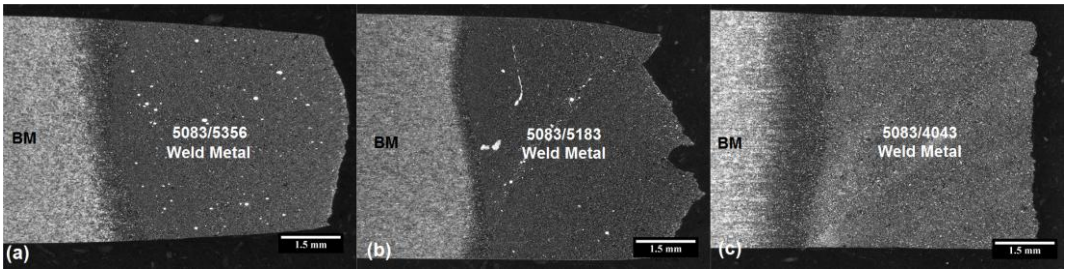

Figure 4.26. Tensile fractures of dressed welds in 5083 aluminium welded with (a) ER5356 filler wire; (b) ER5183 filler wire; and (c) ER4043 filler wire.

Since failure occurs preferentially in the weld metal of dressed 5083-H111 welds, filler metal selection plays an important role in determining the transverse tensile properties of the welds. ER5356 welds display tensile properties very similar to those of the unwelded base metal, with ER5183 and ER4043 resulting in welds with lower strength.

In the case of undressed welds, failure at the fusion line was promoted by the presence of gas pores and lack of fusion type defects at the fusion line, as shown in Figure 4.28.

4.3.3 Tensile properties of 6061-T651 welds

The tensile properties of 6061-T651 aluminium welded using ER5356, ER5183 and ER4043 filler wire in the fully dressed condition are shown in Figures 4.29, 4.30 and 4.31, respectively.

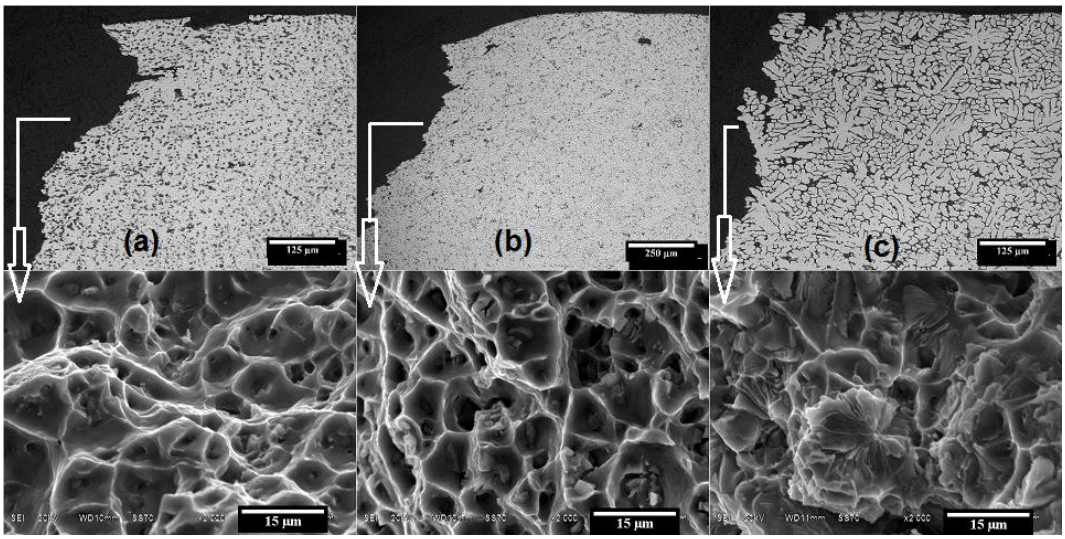

Figure 4.27. Tensile fracture surfaces of 5083-H111 welds displaying predominantly ductile failure in the weld metal of (a) 5083/ER5356, and (b) 5083/ER5183 welds; and mixed-mode failure along the interdendritic eutectic regions in (c) 5083/ER4043 weld metal.

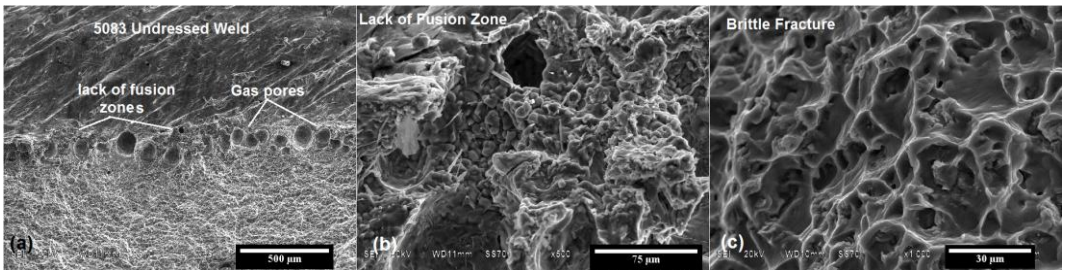

Figure 4.28. Typical tensile fracture surfaces of undressed 5083 welds failing at the weld/HAZ transition zone: (a) lack-of-fusion type defects and gas pores at the 5083 weld/HAZ interface, (b) lack-of-fusion defects; and (c) ductile mixed-mode failure in 5083 at the weld/HAZ interface.

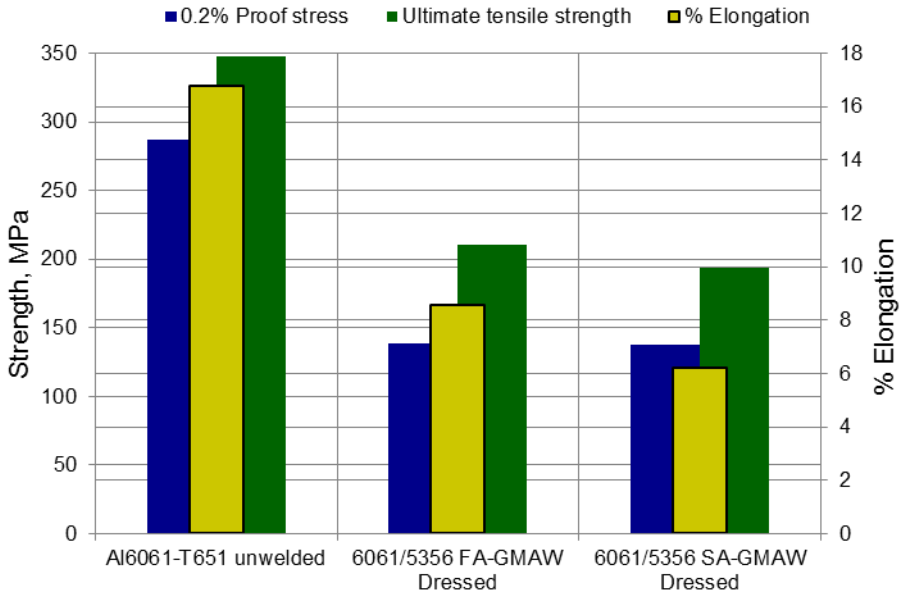

Figure 4.29. Tensile properties of 6061-T651/ER5356 welds.

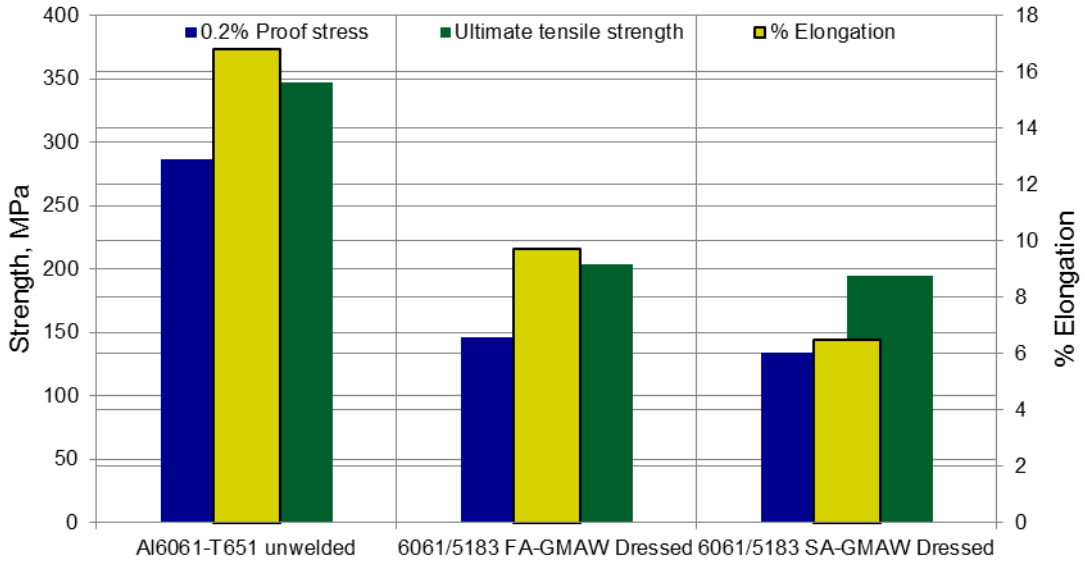

Figure 4.30. Tensile properties of 6061-T651/ER5183 welds.

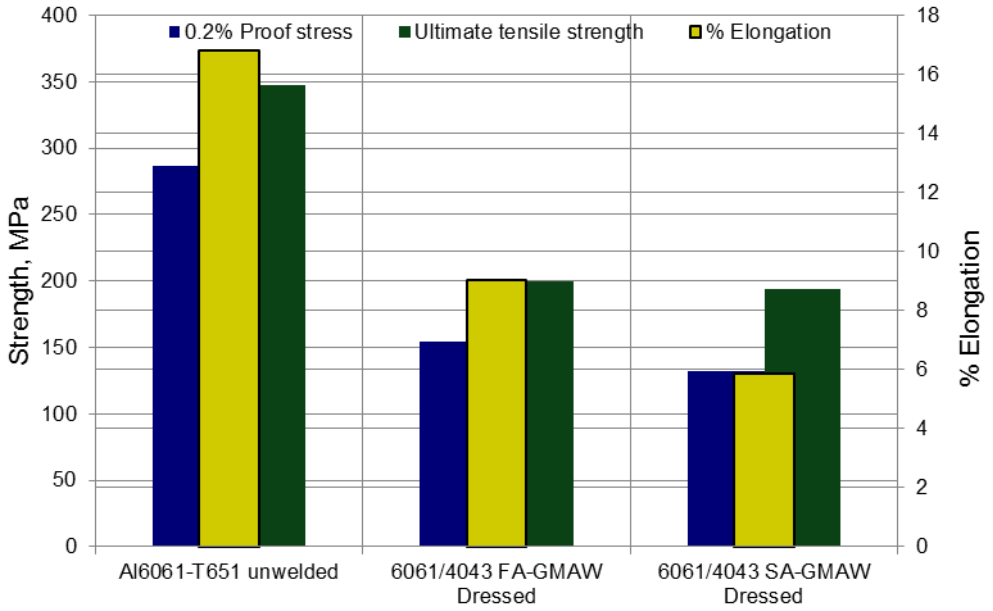

Figure 4.31. Tensile properties of 6061-T651/ER4043 welds.

The tensile properties of the 6061 welds are in all cases significantly lower than those of the unwelded material, regardless of the consumable selected. Failure occurred almost exclusively in the heat-affected zone at the weld/HAZ or HAZ/base metal interface (as shown in Figures 4.32 and 4.33), with the exception of a small number of undressed fully automatic welds. Since the fully automatic welds were welded from one side only, these welds failed in the weld metal due to incomplete penetration during welding. The observation that failure occurred preferentially in the heat-affected zone of the majority of samples is consistent with the low hardness values measured in this region (as illustrated in Figures 4.15 and 4.16). The low heat-affected zone hardness is attributed to grain growth, precipitate dissolution, particle coarsening and recrystallization during the weld thermal cycle. During tensile testing, most of the deformation is concentrated in the soft heat-affected zone region, protecting the weld metal, but resulting in premature failure adjacent to the weld. Local concentration of deformation in the heat-affected zone also leads to low ductility values. Since failure occurs preferentially in the heat-affected zone, filler metal selection has less influence on the

transverse tensile properties of welds in 6061-T651 aluminium, with all three consumables yielding similar tensile properties.

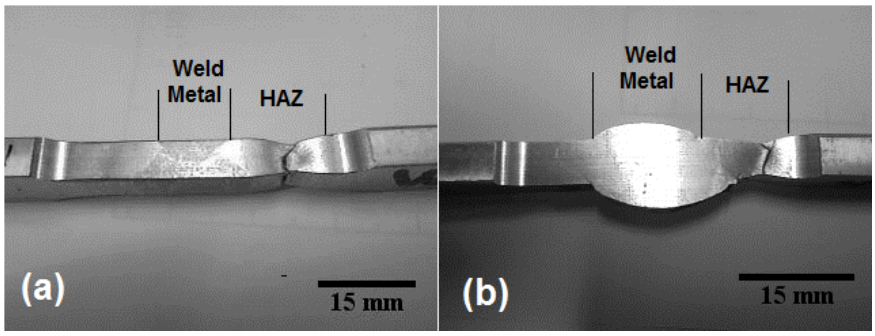

Figure 4.32. Representative photographs of the tensile fractures observed in (a) fully dressed; and (b) undressed semi-automatic welds in 6061-T651.

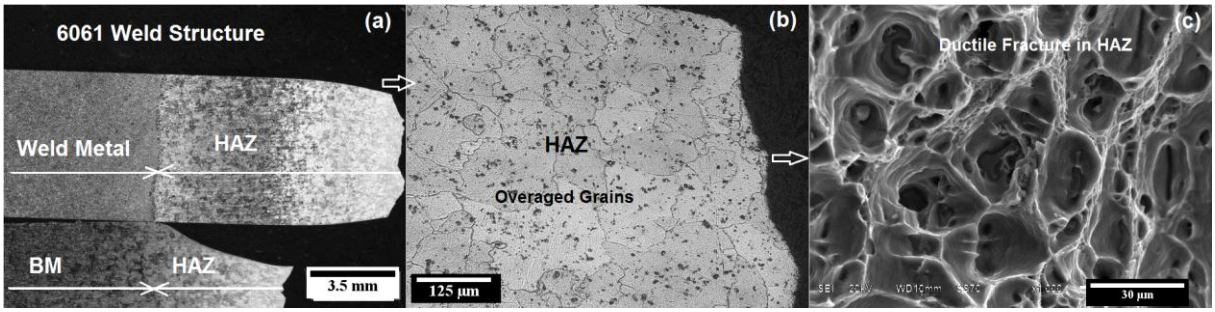

Figure 4.33. Typical tensile fracture surfaces of 6061-T651 welds displaying ductile failure in the heat-affected zone (a) typical fracture location; (b) ductile fracture in the HAZ and; (c) ductile fracture surface in the HAZ of 6061.

The welding technique and filler metal selected also play a major role in determining the corrosion resistance of the welds. This is considered in more detail below.

4.4 Corrosion behaviour of 5083-H111 and 6061-T651 in a 3.5% NaCl solution

Both aluminium 5083-H111 and 6061-T651 in the as-supplied condition exhibit pitting corrosion on immersion in a 3.5% NaCl solution (maintained at a temperature of 16ºC to 27ºC, with a pH between 6.9 and 7.2). Representative examples of the surfaces of these alloys after various immersion times (with a total immersion time of 90 days) are given in Figures 4.34 and 4.35. Although both alloys show evidence of extensive pitting corrosion, alloy 6061-T651 appears to be more severely attacked than 5083-H111. Pitting attack is generally associated with second phase particles in the matrix of both alloys.

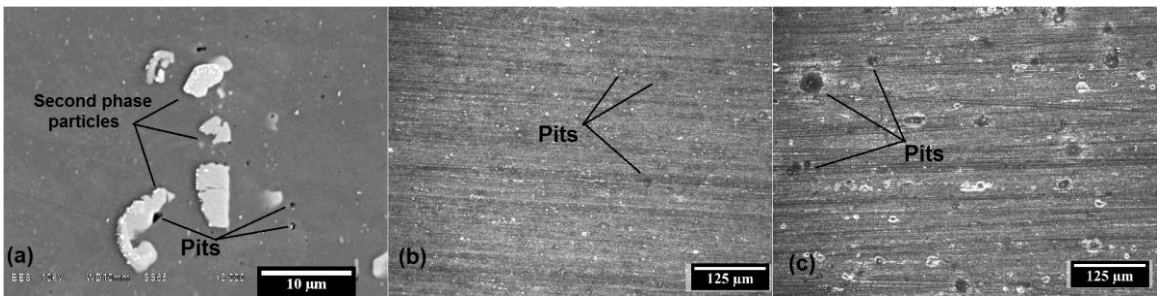

Figure 4.34. Pitting corrosion observed on the surface of 5083-H111 aluminium after immersion in a 3.5% NaCl solution: (a) a polished surface immersed for 24 hours; (b) a ground surface immersed for 30 days; and (c) a ground surface immersed for 90 days.

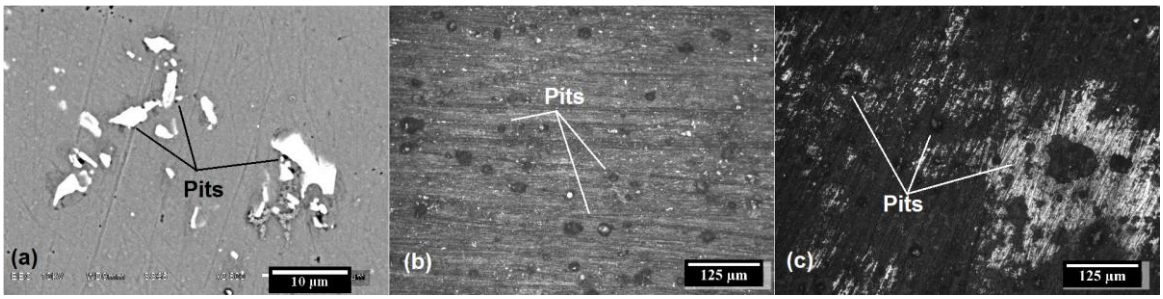

Figure 4.35. Pitting corrosion observed on the surface of 6061-T651 aluminium after immersion in a 3.5% NaCl solution: (a) a polished surface immersed for 3 hours, (b) a ground surface immersed for 30 days; and (c) a ground surface immersed for 90 days.

The pit dimensions observed on immersion in a 3.5% NaCl solution are shown graphically as a function of exposure time in Figures 4.36 and 4.37 for 5083-H111 and 6061-T651, respectively. (See Appendix I for pitting corrosion data). Longer exposure times increase the depth, length and width of the observed pits, with aluminium 6061-T651 showing significantly greater pit depths than 5083-H111 after equivalent exposure times.

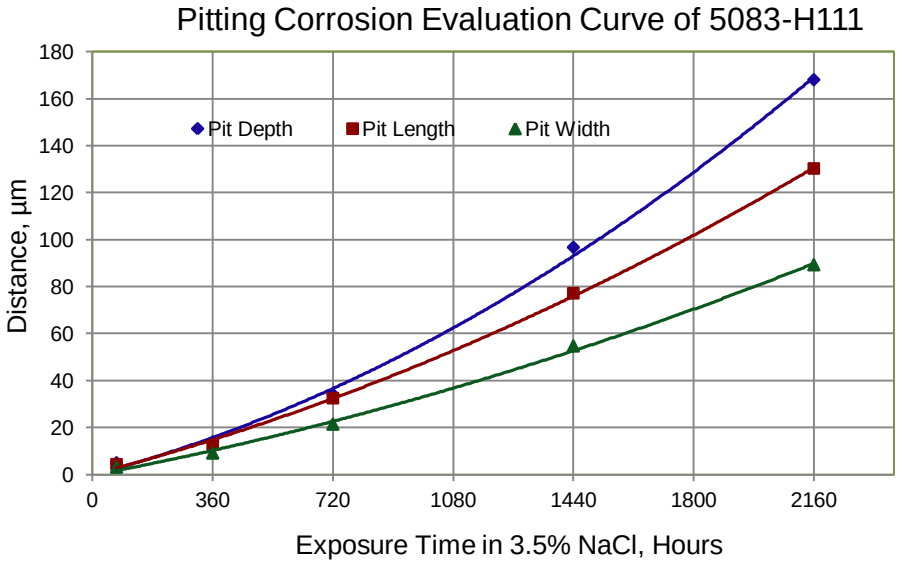

Figure 4.36. Mean dimensions of corrosion pits observed in aluminium 5083-H111 exposed to a 3.5% NaCl solution at temperatures between 25 and 27 ºC and dissolved oxygen contents of 5.5 to 9 ppm.

Welding appeared to increase susceptibility to pitting corrosion. Welds in both 6061-T651 and 5083-H111 aluminium suffered severe pitting attack on exposure to a 3.5% NaCl solution. As shown in Figure 4.38, immersion in a 3.5% NaCl solution of welds in 5083-H111 aluminium resulted in pitting of the weld metal and HAZ of the ER5356 and ER5183 welds, with very severe corrosive attack of the ER4043 weld metal and HAZ. In the 6061-T651 welds, pitting occurred preferentially at the interface between the weld metal and the heat-affected zone. As shown in Figure 4.39, the HAZ of 6061-T651 aluminium appeared to be more susceptible to pitting attack than the HAZ of 5083-H111, welded using the same filler wire.

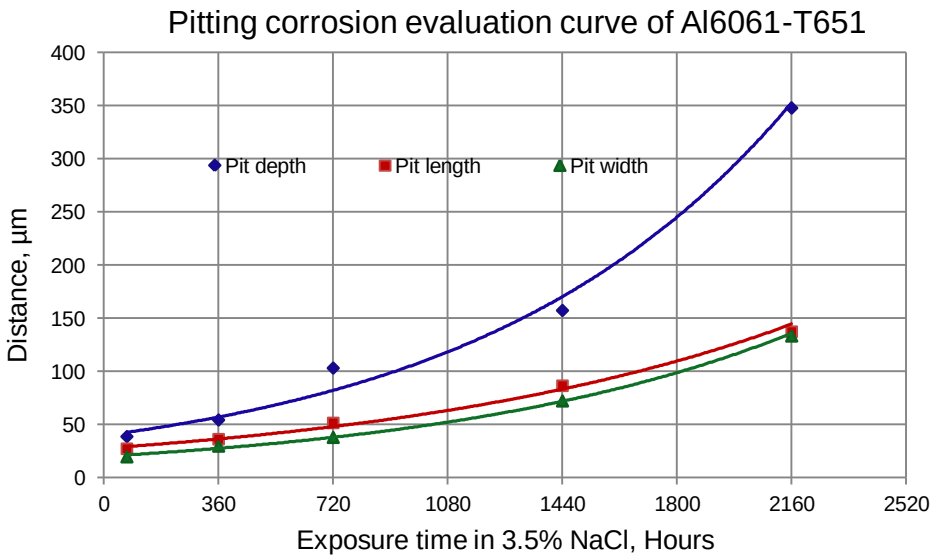

Figure 4.37. Mean dimensions of corrosion pits observed in aluminium 6061-T651 exposed to a 3.5% NaCl solution at temperatures between 25 and 27 ^{0}C and dissolved oxygen contents of 5.5 to 9 ppm.

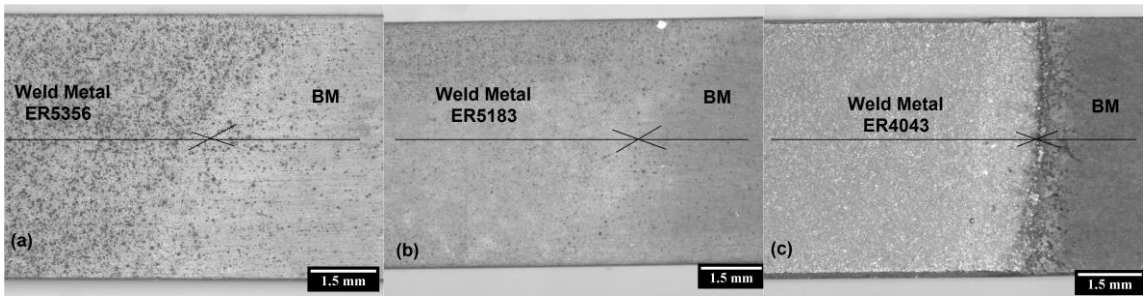

Figure 4.38. Representative photographs of 5083-H111 aluminium welds after immersion in a 3.5% NaCl solution for 60 days: (a) ER5356 filler wire; (b) ER5183 filler wire and; (c) ER4043 filler wire.

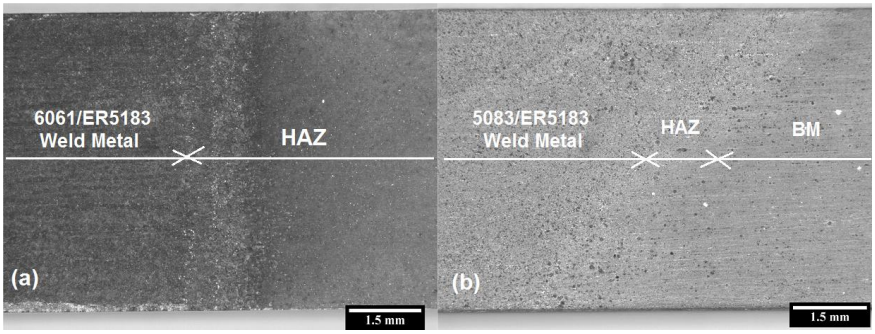

Figure 4.39. Pitting corrosion in the HAZ after immersion in 3.5%NaCl for 60 days: (a) 6061 welded with ER5183; and (b) 5083 welded with ER5183.

4.5 Fatigue properties of 5083-H111 and 6061-T651 aluminium

4.5.1 Fatigue properties in the as-supplied condition

S-N_f curves of 5083-H111 and 6061-H111 in the as-supplied condition after testing in air and in a 3.5% NaCl solution are shown in Figure 4.40. (Detailed fatigue test results are given in Appendix II and Appendix III). As expected, the number of cycles to failure increases with a decrease in the applied stress amplitude (S_a) for both aluminium alloys. The unwelded magnesium-alloyed aluminium 5083-H111 displayed considerably longer fatigue life than 6061-T651 aluminium in air and in a 3.5% NaCl solution, especially at higher stress

amplitudes. Although 6061-T651 has a higher tensile strength than 5083-H111, the greater availability of surface crack initiation sites in the form of precipitates and inclusions probably accelerated fatigue crack initiation and failure in the 6061-T651 alloy.

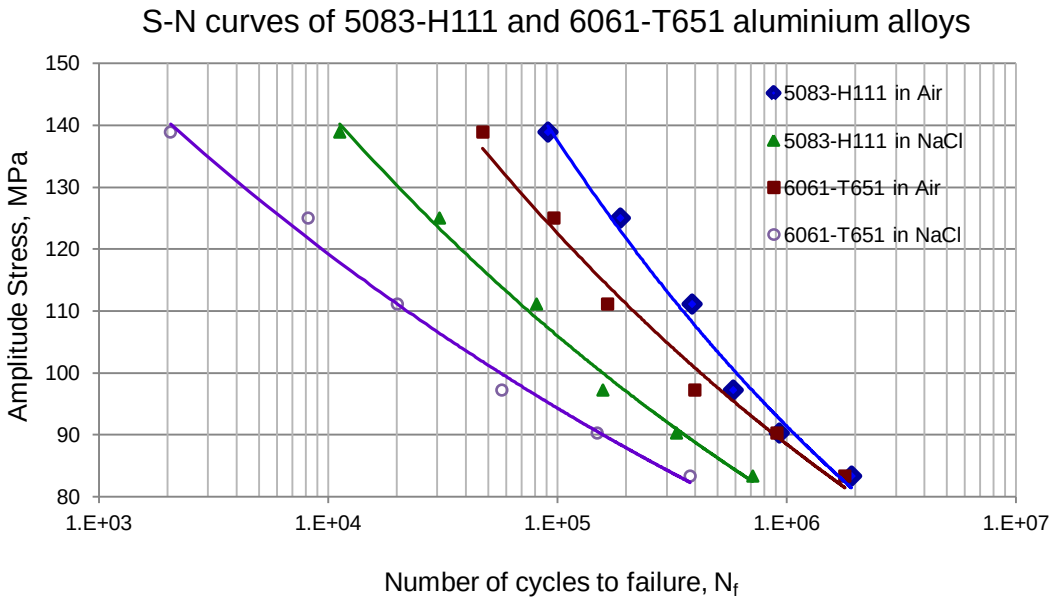

Figure 4.40. S-N curves of 5083-H111 and 6061-T651 aluminium in the as-supplied condition.

During testing in air, fatigue cracks initiated preferentially at the free surfaces of the samples at discontinuities such as slip lines, polishing or machining marks and precipitates or inclusions. This is illustrated in Figures 4.41(a) to (c) for 6061-T651, and Figures 4.42(a) to (c) for 5083-H111. Once initiated at the free surface (Figure 4.41(a)) or at inclusions (Figure 4.42(a)), the cracks propagated rapidly during testing, followed by final ductile failure when the remaining cross section of the sample could no longer sustain the applied stress.

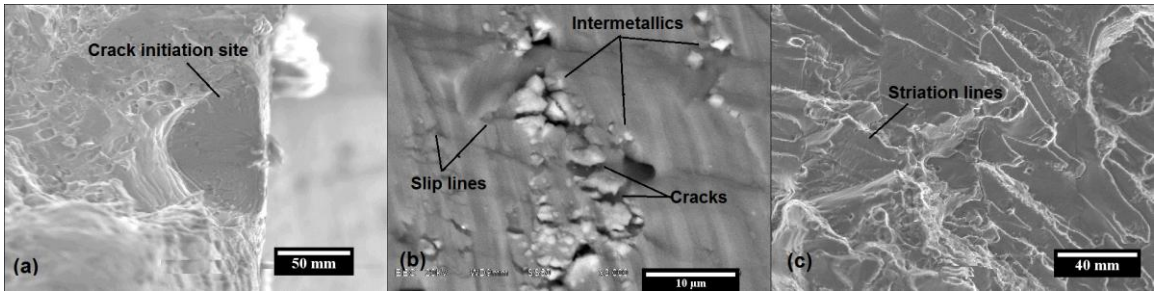

Figure 4.41. (a) Crack initiation site; (b) crack initiation at second phase particles; and (c) crack propagation in a 6061-T651 aluminium alloy fatigued in air.

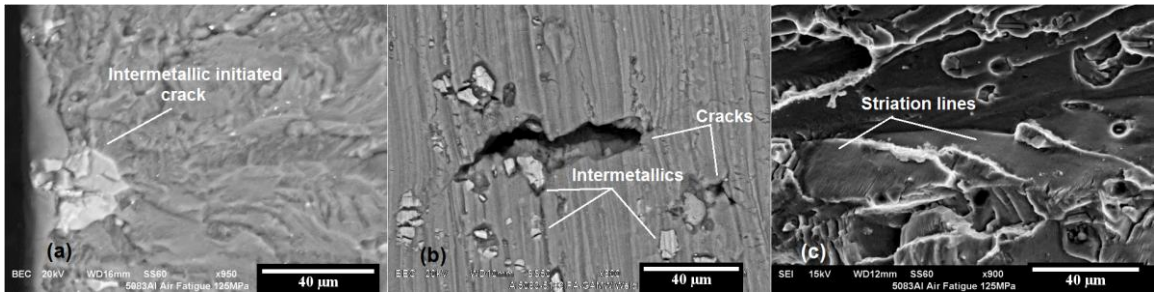

Figure 4.42. Surface crack initiation at a second phase particle; (b) fatigue crack initiation due to disbonding between precipitates and the matrix; and (c) crack propagation in a 5083-H111 aluminium alloy.

Immersion in a 3.5% NaCl solution during fatigue testing shortened the fatigue life of both alloys significantly. As shown in Figures 4.43 and 4.44 for alloys 6061-T651 and 5083-H111, crack initiation was accelerated by the presence of corrosion pits at the surface of the samples. In 6061-T651 aluminium, these pits formed preferentially at precipitates or inclusions due to the galvanic effect between the particle and the aluminium matrix. The greater susceptibility of 6061-T651 to pitting corrosion in chloride-containing solutions accelerated fatigue failure, resulting in shorter fatigue life compared to 5083-H111. In 5083-H111 aluminium, crack initiation occurred at small pits (Figure 4.44(a) and (b)), with pit formation apparently promoted by second phase particles that enhanced the dissolution of the surrounding aluminium matrix.

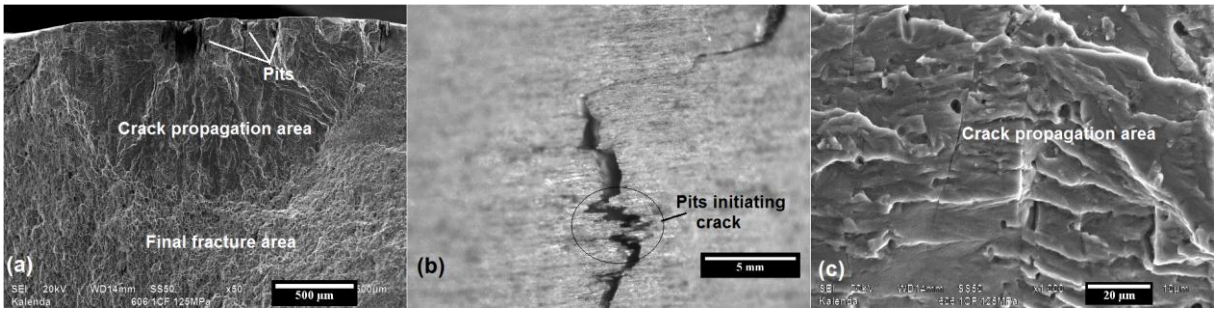

Figure 4.43. (a) and (b) Crack initiation at corrosion pits; and (c) crack propagation in aluminium 6061-T651 during fatigue testing.

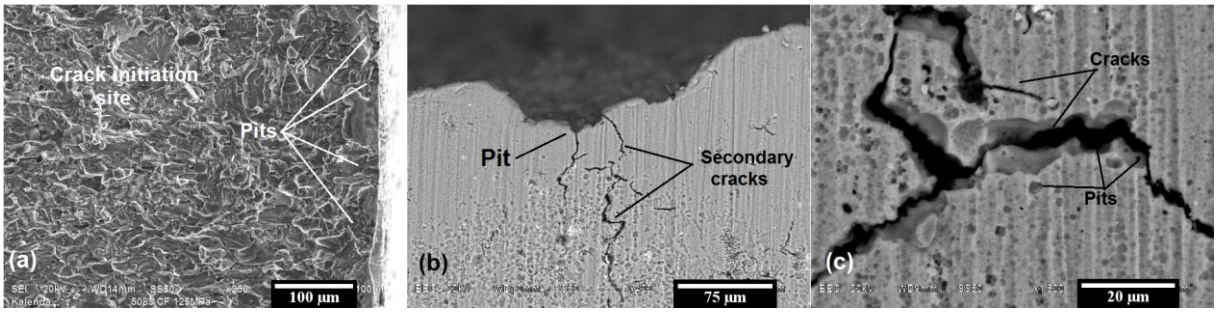

Figure 4.44. (a) Multiple fatigue crack initiation sites at small corrosion pits; (b) crack propagation from corrosion pits; and (c) fatigue cracks associated with small pits in 5083-H111 aluminium.

The fatigue damage ratio (DR) is the ratio between the number of cycles to failure in a 3.5% NaCl solution ($N_{f\ NaCl}$) and the number of cycles to failure in air ($N_{f\ Air}$), as shown in equation (4.1).

$$DR = \frac{N_{f\,NaCl}}{N_{fAir}} \qquad \text{.... (4.1)}$$

The limit values of the fatigue damage ration are zero (0) and one (1). The DR approaches zero only when $N_{f\ NaCl}$ approaches zero, i.e. pitting corrosion is the dominant process in determining the corrosion fatigue behaviour. Corrosion pits act as stress raisers by rapidly initiating fatigue cracks. When DR approaches one, or $N_{f\ NaCl}$ approaches $N_{f\ Air}$, the dominant process determining fatigue life is the fluctuating stress.

The fatigue damage ratios (DR) of 5083-H111 and 6061-T651 aluminium in the as-supplied condition are shown graphically in Figure 4.45. This graph indicates that the effect of pitting corrosion on fatigue properties in unwelded specimens is most pronounced at higher stress amplitudes. At high stress levels, corrosion pits act as sharp stress raisers, accelerating fatigue crack initiation. The effect of the corrosive environment on fatigue properties becomes less apparent at lower stress amplitudes, but is unlikely to approach a ratio of one (signifying that

the corrosive environment has no influence on fatigue behaviour). The fatigue damage ratio of 5083-H111 aluminium is higher than that of 6061-T651 at all applied stress levels, implying that the fatigue properties of 5083-H111 are less sensitive to the effect of pitting corrosion than those of 6061-T651. This can be attributed to the higher corrosion resistance of 5083-H111 in chloride-containing environments.

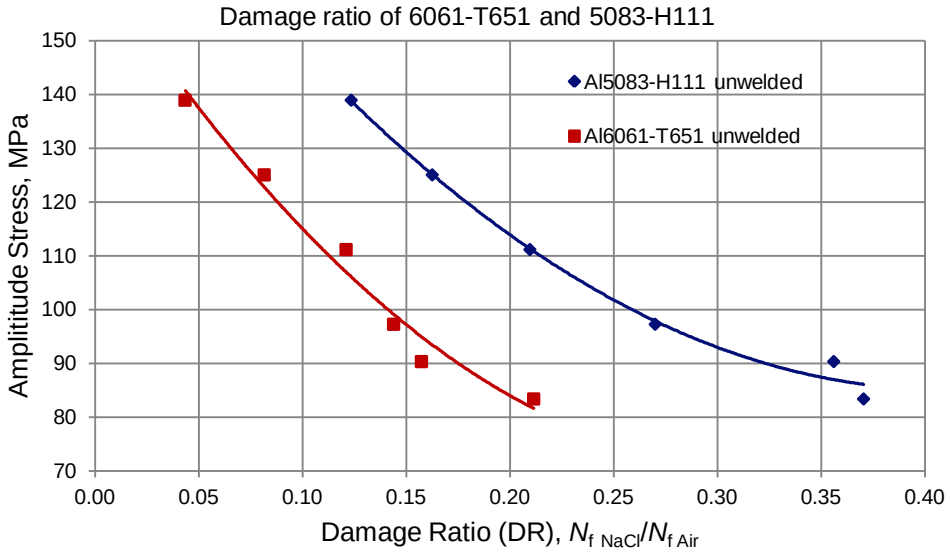

Figure 4.45. Fatigue damage ratio, DR, of 5083-H111 and 6061-T651 aluminium.

4.5.2 Fatigue behaviour of 5083-H111 aluminium welds

4.5.2.1 Aluminium 5083-H111 welded using ER5356 filler wire

The results of fatigue tests in air of 5083-H111 aluminium joined using ER5356 filler wire are shown in Figure 4.46. The data points shown represent median values, whereas the S-N_f curves in Figure 4.46 were fit using the power law. It is evident that welding reduces the fatigue life of aluminium 5083-H111 significantly. Semi-automatic welds (fully dressed and as-welded) and as-welded (undressed) fully automatic welds display similar fatigue properties, with the fully dressed semi-automatic welds performing marginally better than the undressed joints. The dressed fully automatic welds display much higher fatigue properties, which can be attributed to the absence of sharp stress concentrations at the weld toe and root, and the reduced incidence of welding defects such as porosity.

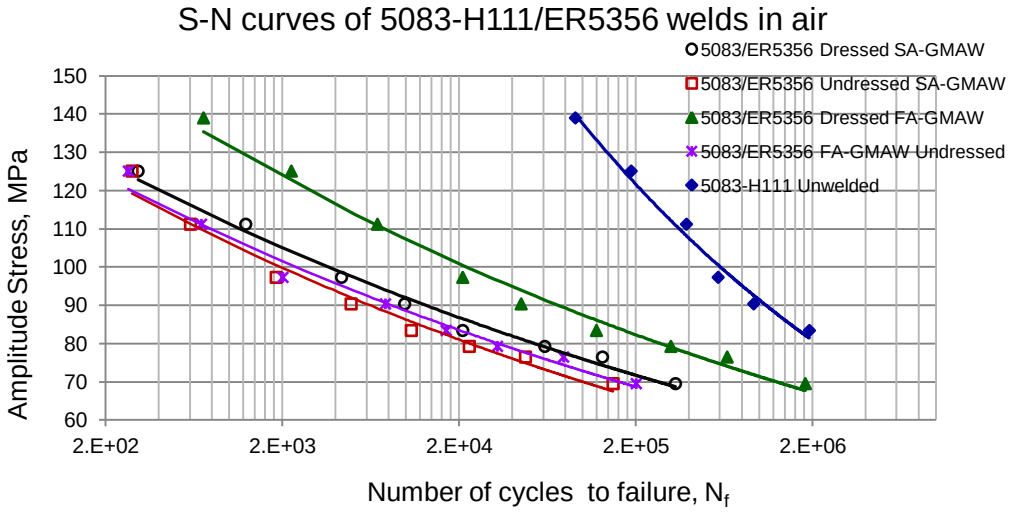

Figure 4.46. Fatigue properties of 5083-H111 welded with ER5356, tested in air.

Fatigue cracks initiated preferentially at gas pores, lack-of-fusion type defects and incomplete weld penetration; and at the weld toes of undressed joints, as illustrated in Figure 4.47. Crack propagation occurred preferentially in the weld metal.

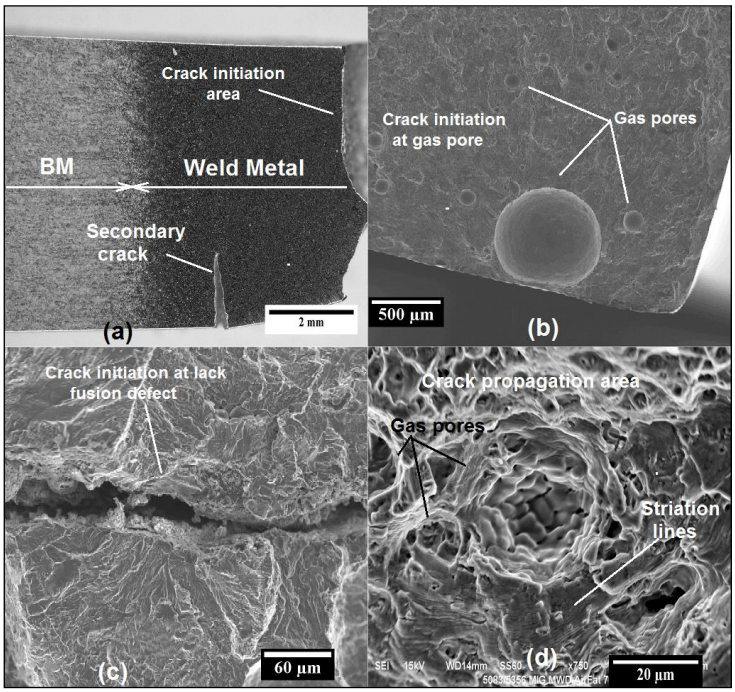

Figure 4.47. Typical fatigue fractures in 5083 welds: (a) crack initiation in the weld metal; (b) crack initiation associated with a large gas pore; (c) crack initiation at a lack-of-fusion type defect; (d) crack propagation associated with gas pores.

The results of fatigue tests of 5083-H111 aluminium joined using ER5356 filler wire in a 3.5% NaCl solution are shown in Figure 4.48. The results indicate that immersion in NaCl during fatigue testing reduces the fatigue properties of both the semi-automatic and fully automatic welds. The advantage gained by fully automatic welding in reducing the number of welding defects are largely negated in the presence of a corrosive environment due to the introduction of corrosion pits as preferential crack initiation sites. The fully automatic weld therefore displays similar fatigue performance to the semi-automatic weld under corrosion fatigue conditions.

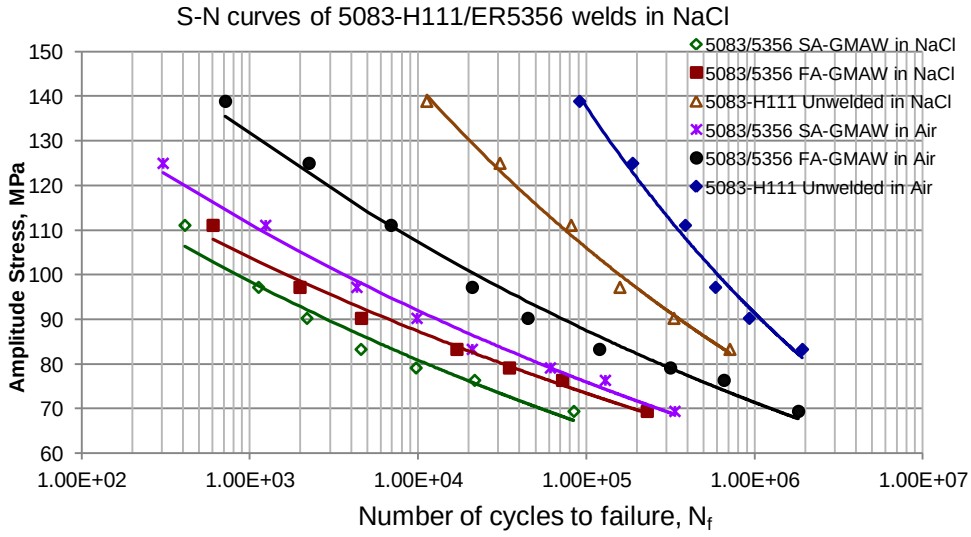

Figure 4.48. Fatigue properties of 5083-H111 welded with ER5356, tested in a 3.5% NaCl solution.

The fatigue damage ratio (DR) curve of 5083/ER5356 welds shown in Figure 4.49 reveals that the effect of pitting corrosion on fatigue properties is most pronounced at stress amplitudes between 80 and 70 MPa. In this stress range, pits act as sharp stress raisers, accelerating fatigue crack initiation. Due to the presence of pre-existing weld defects, the effect of the corrosive environment on the fatigue properties of the welds becomes less apparent at higher stress amplitudes. At these higher stress amplitude values, the number of cycles to failure decreases and the effect of pitting corrosion becomes less apparent.

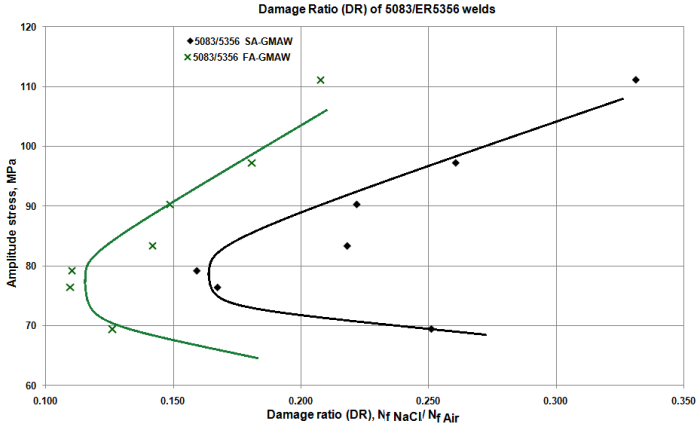

Figure 4.49. Fatigue damage ratio of 5083-H111 aluminium welded with ER5356 filler metal.

During fatigue testing in a 3.5% NaCl solution, cracks initiate preferentially at pits in the weld metal (Figure 4.50(a) and (b)), or at discontinuities such as the lack-of-fusion type defect shown in Figure 4.50(d)).

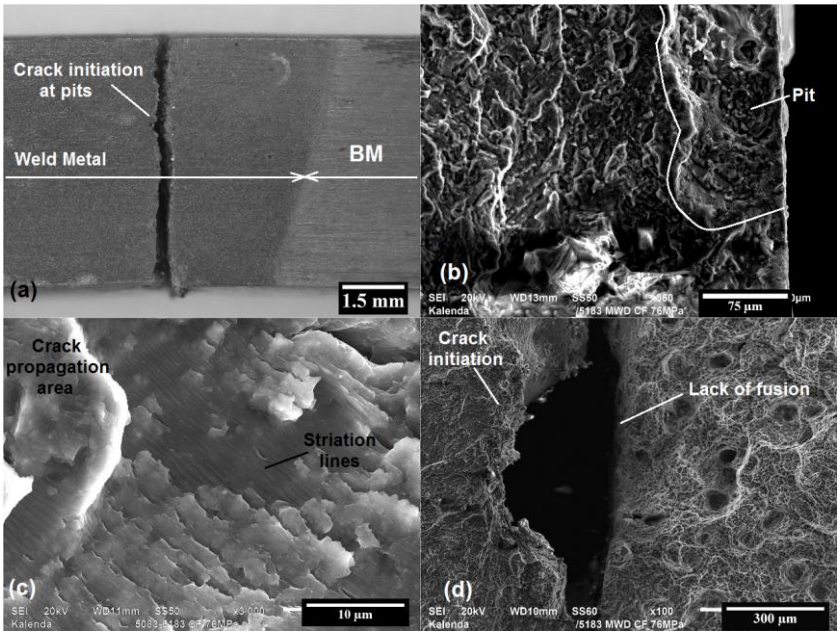

Figure 4.50. Typical features of fatigue fracture in 5083/ER5356 welds tested in 3.5% NaCl: (a) and (b) crack initiation at pits in the weld metal; (c) crack propagation in the weld metal; and (d) crack initiation at a lack-of-fusion type defect.

4.5.2.2 Aluminium 5083-H111 welded using ER5183 filler wire

The fatigue properties (in air) of 5083-H111 aluminium welded with ER5183 filler wire using semi-automatic or fully automatic GMAW are presented in Figure 4.51. Welding reduces the fatigue life considerably. Failure occurs in the weld metal, which has a lower hardness and strength than the base materials (as shown in Figures 4.17 and 4.23). Cracks initiate preferentially at weld defects such as gas pores, lack-of-fusion type defects, incomplete penetration and slag inclusions.

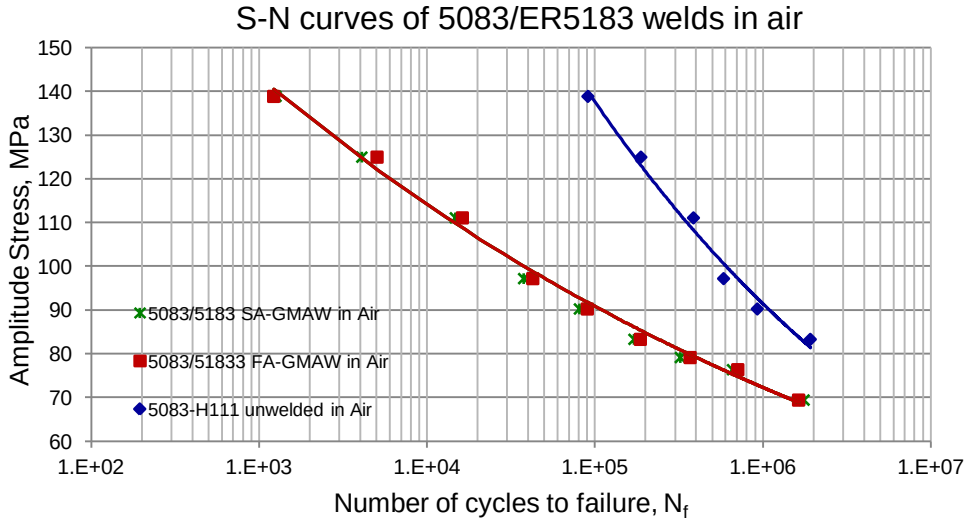

Figure 4.51. Fatigue properties of 5083/ER5183 welds tested in air.

Figure 4.52 displays the corrosion fatigue properties of 5083-H111 aluminium welded with ER5183 filler wire tested in a 3.5% NaCl solution. The corrosive environment reduces the number of cycles to failure for the semi-automatic and fully automatic welds. Cracking occurs preferentially in the softer weld metal which corrodes faster than the base material (Figure 4.39(b)). Crack initiation is accelerated by pits that formed prematurely in the weld metal at defects such as gas pores, lack-of-fusion defects and slag inclusions. Very little difference is evident between semi-automatic and fully automatic welds, suggesting that the lower defect content of the automatic welds does not affect the fatigue behaviour significantly.

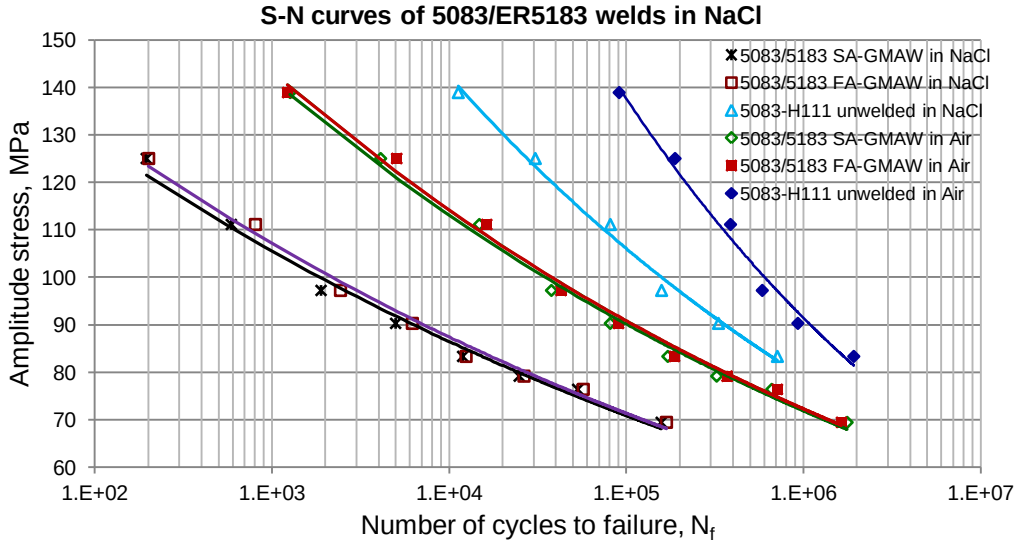

Figure 4.52. Fatigue properties of 5083/ER5183 welds tested in a 3.5% NaCl solution.

The fatigue damage ratio of aluminium 5083-H111 welded with ER5183 filler wire is shown in Figure 4.53 for semi-automatic and fully automatic welds. Corrosion fatigue plays a more dominant role at higher stress amplitudes, where the presence of welding defects may accelerate pitting corrosion, leading to rapid fatigue crack initiation and propagation.

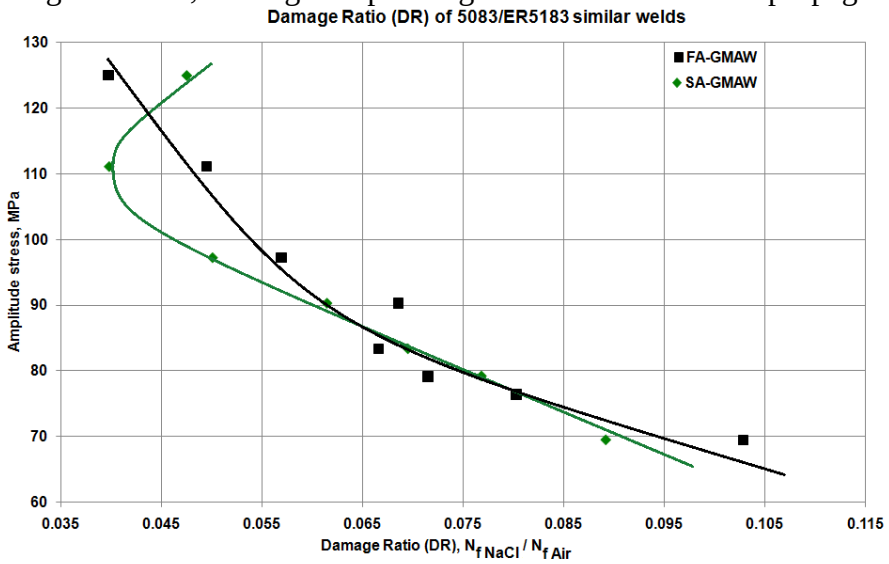

Figure 4.53. Fatigue damage ratio of 5083-H111 welded with ER5183 filler wire.

4.5.2.3 Aluminium 5083-H111 welded using ER4043 filler wire

Figure 4.54 displays the fatigue properties in air of aluminium alloy 5083-H111 welded with ER4043 filler wire. Failure occurs in the weld metal and these welds exhibit reduced fatigue life compared to that of unwelded 5083-H111 tested under the same conditions. The 5083/ER4043 welds appear to be sensitive to the presence of weld defects, with the semi-automatic welds displaying lower fatigue properties than the fully automatic welds.

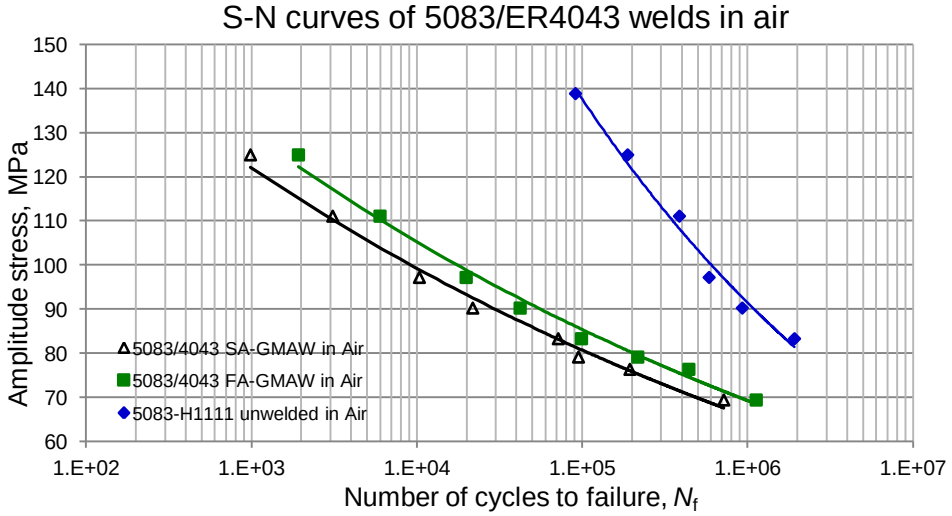

Figure 4.54. Fatigue properties of 5083/ER4043 welds tested in air.

The corrosion fatigue properties of 5083-H111 aluminium welded with ER4043 filler metal using semi-automatic and fully-automatic pulsed GMAW are presented in Figure 4.55. The semi-automatic and fully automatic welds display similar corrosion fatigue life when tested in a 3.5% NaCl salt water environment, suggesting that the presence of a higher percentage of welding defects in the semi-automatic welds did not affect the fatigue behaviour in the

corrosive environment to any significant extent. The short fatigue life of these welds can be attributed to the poor corrosion resistance of the ER4043 welds. Pit formation is rapid, with fatigue cracks initiating prematurely at corrosion pits.

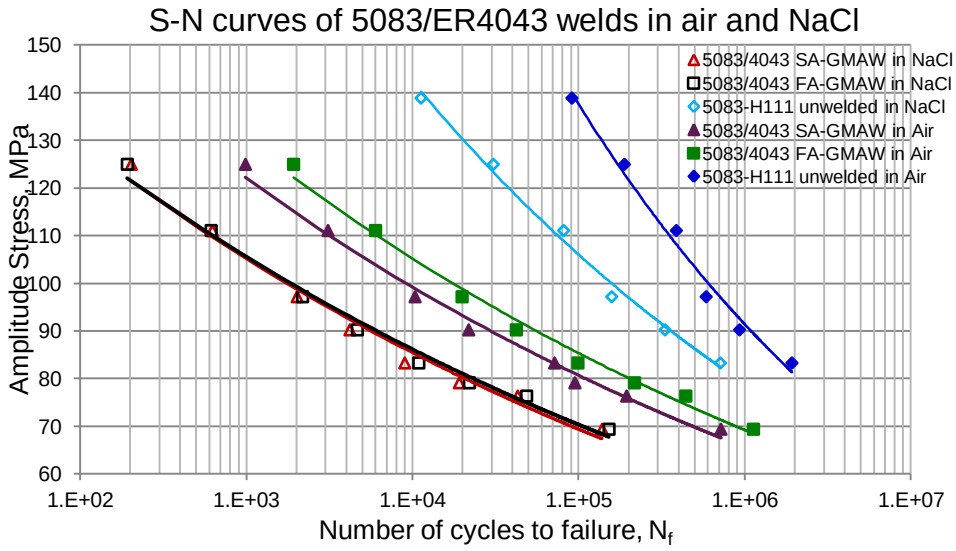

Figure 4.55. Corrosion fatigue properties of 5083-H111 aluminium welded with ER4043 filler metal.

The fatigue damage ratio (DR) values of 5083-H111 aluminium welded using ER4043 filler metal are presented in Figure 4.56. The fatigue ratio values are low, suggesting that the fatigue properties of the welds are sensitive to pitting corrosion in the NaCl solution. The fully automatic welds appear to be affected to a greater extent by the presence of a corrosive environment. These welds displayed slightly better fatigue properties than the semi-automatic welds in air, probably due to the lower number of weld defects. In the NaCl solution, however, both curves shift to lower numbers of cycles to failure, with the fully automatic curve shifting more than the semi-automatic curve. This suggests that the availability of welding defects ceases to dominate the fatigue behaviour, with crack initiation at corrosion pits becoming controlling. The rapid pitting rate of the ER4043 weld in NaCl therefore creates large numbers of potential pit initiation sites in both the fully automatic and semi-automatic welds, resulting in a very low damage ratio, especially for the fully automatic weld.

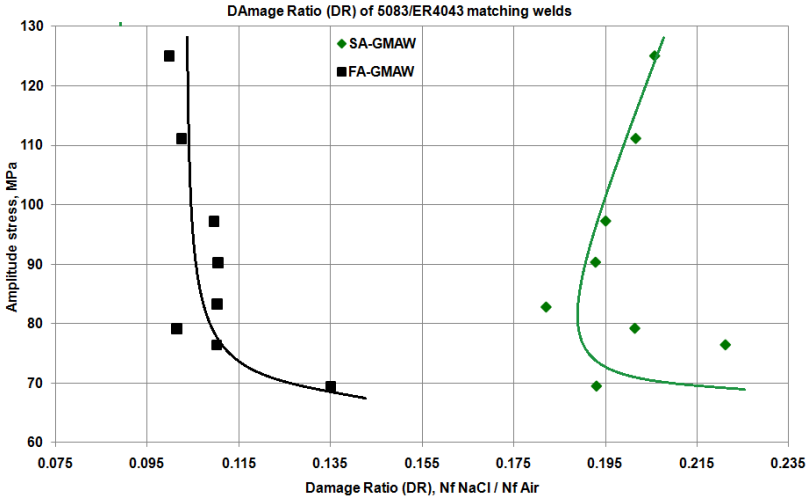

Figure 4.56. Fatigue damage ratio of 5083/ER4043 welds.

4.5.3 Fatigue behaviour of 6061-T651 aluminium welds

4.5.3.1 Aluminium 6061-T651 welded using ER5356 filler wire

The results of fatigue tests in air of 6061-T651 aluminium joined using ER5356 filler wire are shown in Figure 4.57.

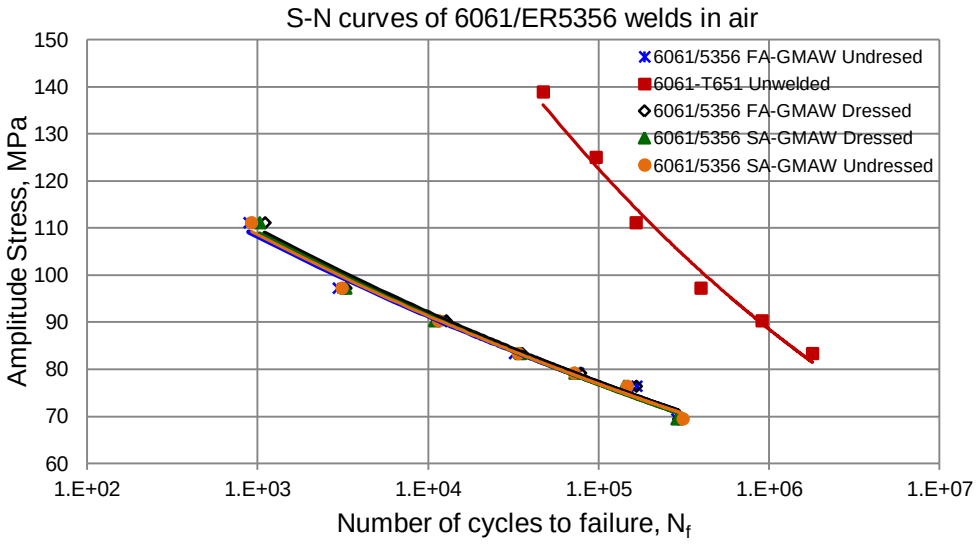

Figure 4.57. Fatigue properties of aluminium 6061-T651 welded with ER5356, tested in air.

The S-N_f curves in Figure 4.57 confirm that welding reduces the fatigue properties of 6061 aluminium significantly. It is interesting to note that the mode of welding (fully automatic or semi-automatic) and dressing of the weld prior to testing have no statistically relevant influence on the fatigue life of the welded samples. In 6061-T651 aluminium, failure occurs preferentially in the heat-affected zone (as shown in Figures 4.58(a) and (b)) due to softening and precipitate coarsening/dissolution during welding. The higher incidence of welding defects in the semi-automatic welds (a weld metal phenomenon) therefore does not play a role in initiating fatigue cracks in this instance. The softened heat-affected zone apparently acts as preferential fatigue crack initiation site, regardless of the absence of a stress raiser at the weld toe in the dressed welds. Cracks apparently initiated at the free surface at cavities left by hard particles during fatigue testing (Figure 4.58(c)), and gradually propagated to final failure as shown on Figure 4.58(d).

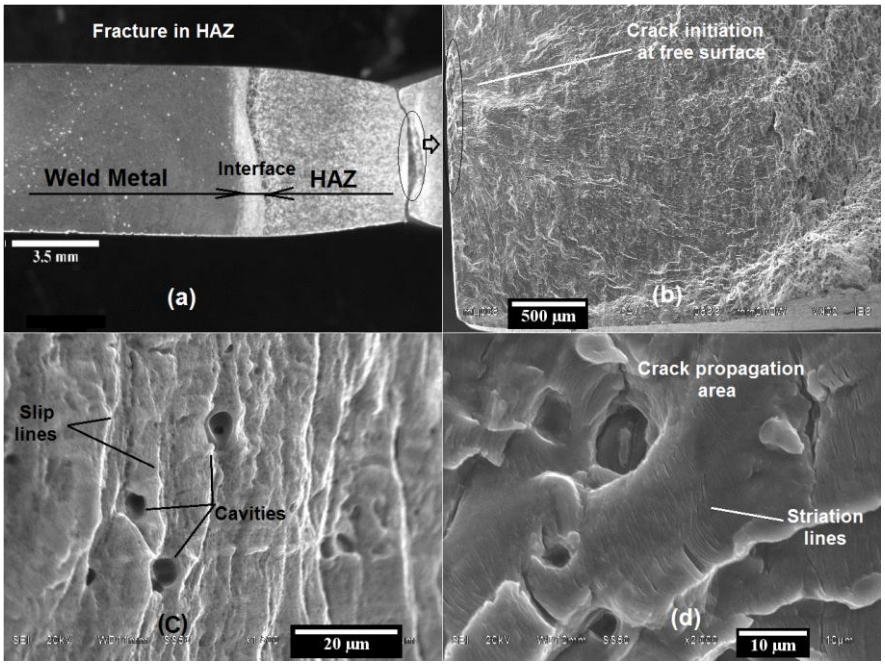

Figure 4.58. Typical fatigue fracture of 6061 welds: (a) failure in HAZ; (b) crack initiation from a cavity left by a second phase particle; (c) cavities left by second phase particles; and (d) crack propagation.

The influence of immersion in a 3.5% NaCl solution during the fatigue testing of 6061-T651 aluminium joined using ER5356 filler wire is shown in Figure 4.59 for fully dressed welds. A similar trend to that observed in Figure 4.57 is evident. Exposure to a corrosive environment during fatigue testing largely negated the advantage gained by reducing the number of weld defects through fully automatic welding. The combination of a lower hardness in the heat-affected zone, the presence of coarse precipitates and preferential pitting corrosion in the HAZ facilitates rapid fatigue crack initiation in the heat-affected zone.

Cracks initiate preferentially at pits formed at the weld metal/HAZ interface as shown in Figure 4.60(a) and (b). Pitting in this area seems to be accelerated by the presence of pre-existing weld defects, such as gas pores (as shown in Figure 4.60(c)). These defects reduce the time required for pit initiation.

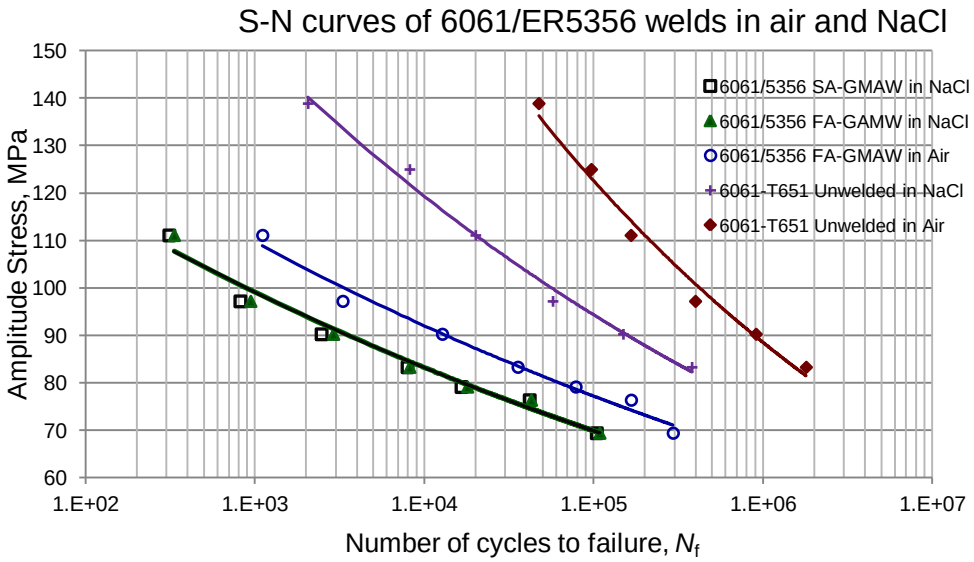

Figure 4.59. Fatigue properties of 6061-T651 welded with ER5356, tested in a 3.5% NaCl solution.

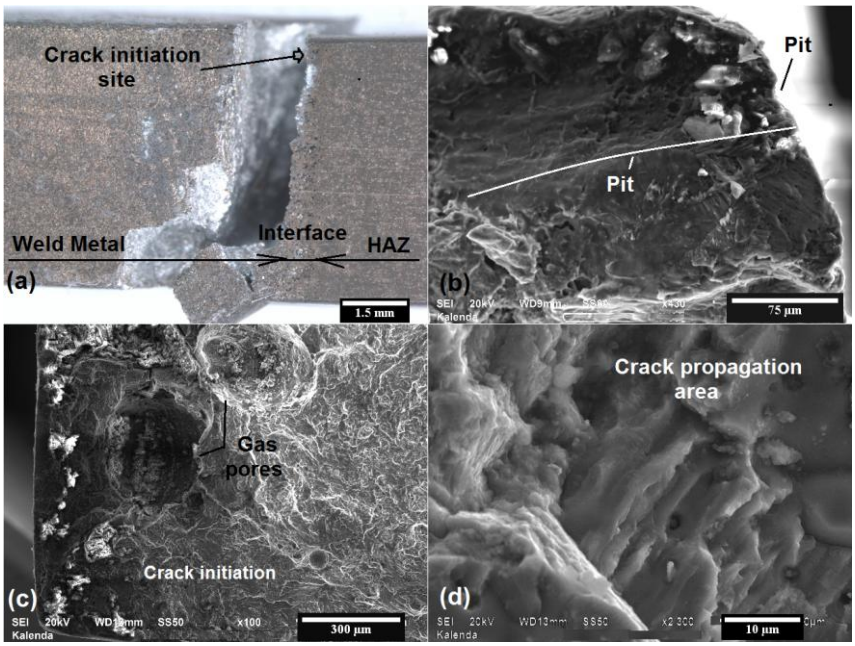

Figure 4.60. Typical fatigue fracture of 6061/ER5356 welds tested in a 3.5% NaCl solution: (a) failure at the interface between the weld metal and HAZ; (b) crack initiation from a corrosion pit; (c) crack initiation from corroded gas pores; and (d) crack propagation.

The fatigue damage ratio calculated for 6061-T651 welded with ER5356 filler wire is shown in Figure 4.61. The damage ratios for the fully automatic and semi-automatic welds are similar since weld defects play a less important role in the initiation of fatigue cracks. The effect of pitting corrosion on the fatigue properties is most apparent between stress amplitudes of 75 and 90 MPa. The effect of a corrosive environment on the fatigue properties of the welds becomes less apparent at higher and lower stress amplitudes, for both semi-automatic and fully automatic GMAW welds.

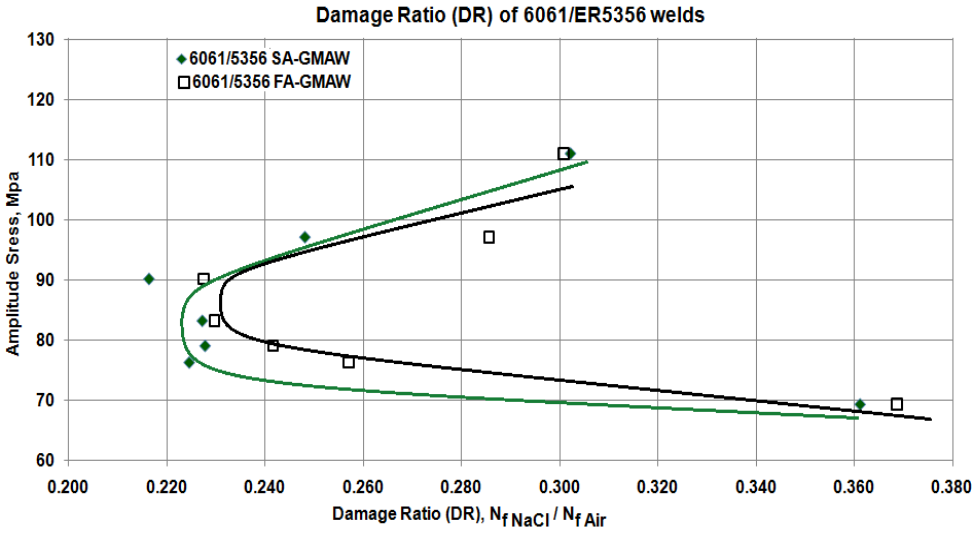

Figure 4.61. Fatigue damage ratio of 6061-T651 aluminium welded with ER5356 wire.

4.5.3.2 Aluminium 6061-T651 welded using ER5183 filler wire

The fatigue properties of 6061-T651 welds joined using ER5183 filler wire in air are shown in Figure 4.62. Welding reduces the fatigue life of 6061-T651 significantly, with fully automatic welds showing significantly better fatigue properties compared to semi-automatic welds. Failure occurs in the heat-affected zone due to the lower hardness in this region. The presence of weld defects, such as gas pores, lack-of-fusion defects and incomplete weld penetration, contributes to premature failure. These defects are more apparent in the semi-automatic welds, resulting in reduced fatigue life compared to fully automatic welds tested under similar conditions.

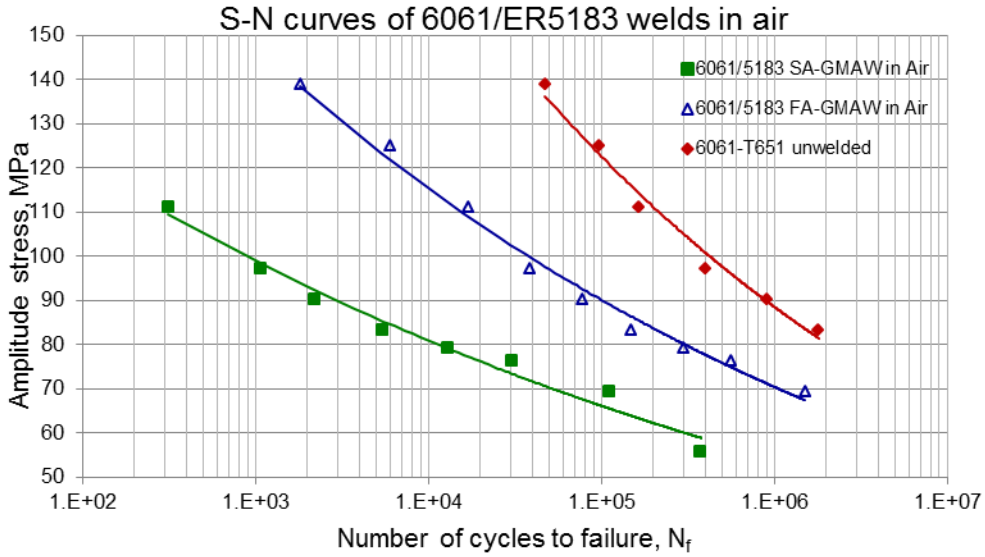

Figure 4.62. Fatigue properties of 6061/ER5183 welds tested in air.

Figure 4.63 shows the corrosion fatigue properties, tested in a 3.5% NaCl solution, of 6061-T651 aluminium welded with ER5183 filler wire. Immersion in a corrosive environment reduces the fatigue life of both the semi-automatic and fully automatic welds. The fatigue life of the semi-automatic weld is much lower than that of the fully automatic weld. At higher stress amplitudes, failure occurs preferentially in the softened heat-affected zone with crack initiation mainly at cavities left by hard constituent particles. At lower stress amplitudes, cracks initiate at corrosion pits at the weld metal/HAZ interface.

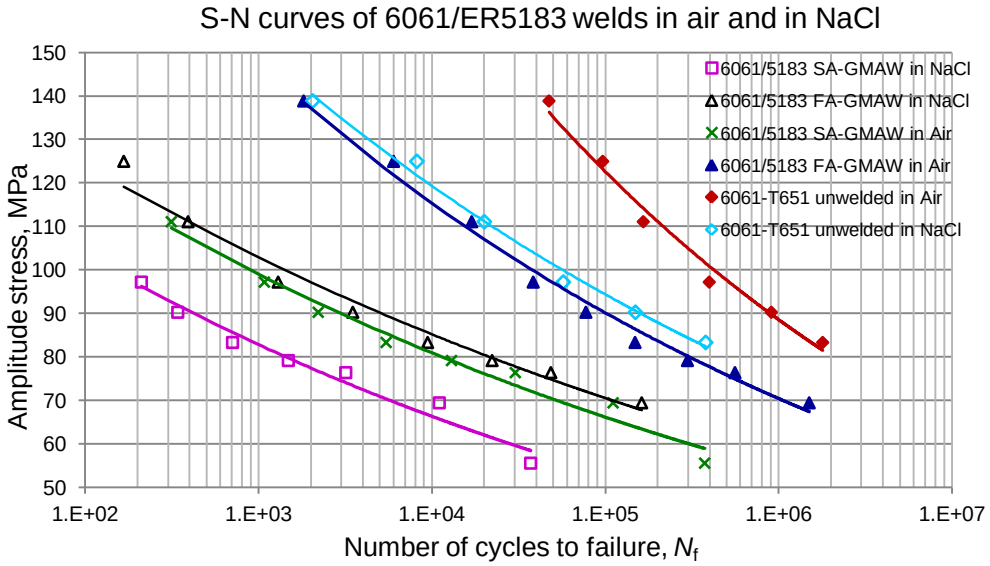

Figure 4.63. Fatigue properties of 6061-T651 aluminium alloy welded with ER5183 filler wire tested in air and in a 3.5% NaCl solution.

Figure 4.64 compares the fatigue damage ratio curves of semi-automatic and fully automatic welds of 6061-T651 aluminium and ER5183 filler wire. The curves for the fully automatic and semi-automatic welds are separated, suggesting that the availability of welding defects at the fusion line plays a role in initiating fatigue failure. The low fatigue damage ratio of the fully automatic welds suggests that it is affected more by the presence of corrosion pits,

whereas the prior availability of welding defects in the semi-automatic welds results in a higher damage ratio.

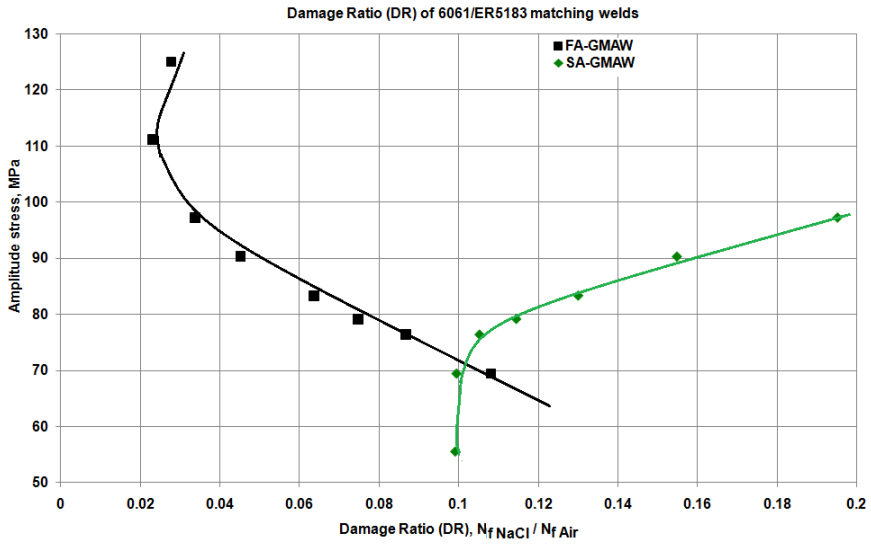

Figure 4.64. Fatigue damage ratio of 6061-T651 welded with ER5183 filler wire.

4.5.3.3 Aluminium 6061-T651 welded using ER4043 filler wire

The measured fatigue S-N_f curves for aluminium 6061-T651 welded with ER4043 filler are shown in Figure 4.65 for fully automatic and semi-automatic welds tested in air. Welding reduces the fatigue life significantly, but there is very little difference between the fully automatic and semi-automatic welds. Cracking occurs preferentially in the heat-affected zone, therefore the higher incidence of welding defects in the semi-automatic welds (a weld metal phenomenon) does not play a significant role in initiating fatigue cracks. The softened heat-affected zone acts as preferential fatigue crack initiation site.

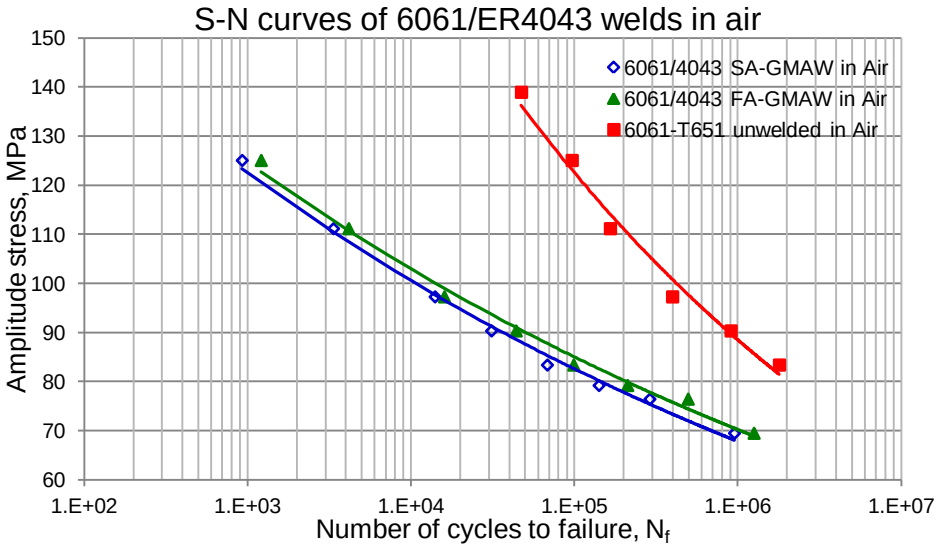

Figure 4.65. Fatigue properties of 6061/ER4043 welds in air.

Figure 4.66 displays the corrosion fatigue properties of the 6061/ER4043 welds tested in a 3.5% NaCl solution. The presence of the corrosive environment reduces the fatigue life of both the fully automatic and semi-automatic welds. The semi-automatic welds have slightly shorter fatigue lives than the fully automatic welds, suggesting that the presence of weld

defects such as gas pores, lack-of-fusion type defects and incomplete weld penetration accelerates fatigue crack initiation in NaCl. These defects facilitate rapid pit initiation.

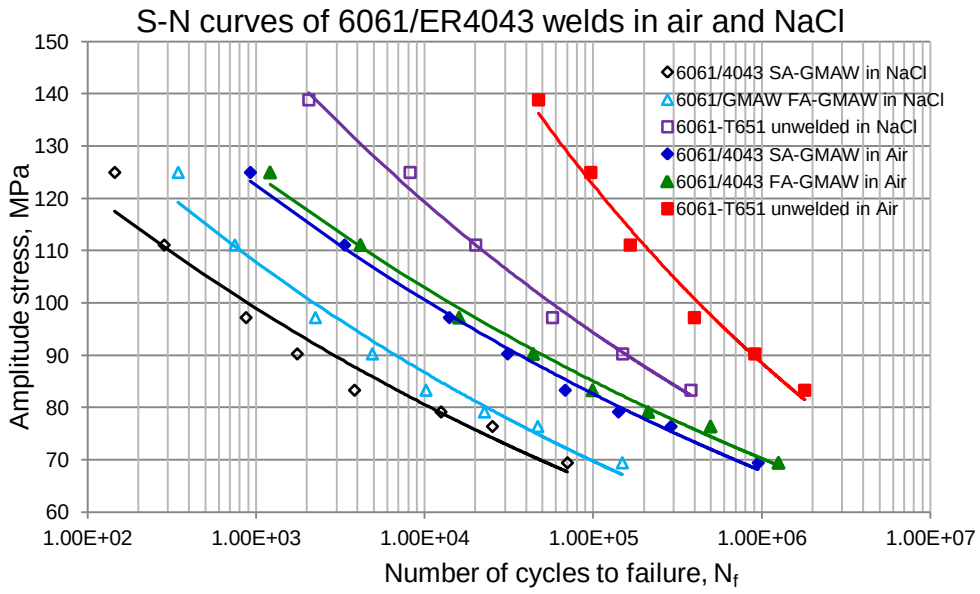

Figure 4.66. Corrosion fatigue properties of 6061-T651 aluminium welded with ER4043 filler wire in a 3.5% NaCl solution.

The fatigue damage ratio (DR) of 6061-T651 welded with ER4043 is displayed in Figure 4.67. The semi-automatic welds appear to be more sensitive to the presence of a corrosive environment, probably as a result of accelerated pit initiation at welding defects. At high amplitude stress values, pitting corrosion has less effect on fatigue resistance as fewer cycles are required to failure and fatigue cracks are more likely to initiate at pre-existing defects.

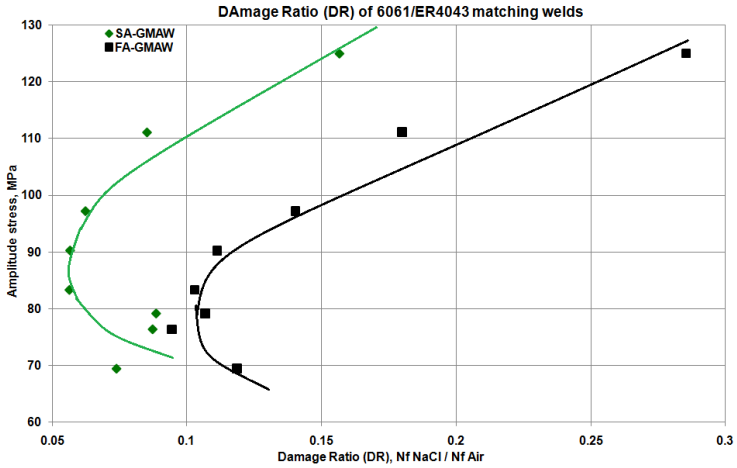

Figure 4.67. Fatigue damage ratio of 6061/ER4043 welds.

4.5.4 Fatigue behaviour of dissimilar welds of 5083-H111and 6061-T651 aluminium

4.5.4.1 Dissimilar welds joining 5083-H111 and 6061-T651 using ER5356 filler wire:

The fatigue properties in air and NaCl of dissimilar welds of 5083-H111 and 6061-T651 aluminium joined using ER5356 filler wire are shown in Figure 4.68. The dissimilar welds display much reduced fatigue properties compared to the unwelded base materials, but similar fatigue properties to those measured in the 6061/ER5356 and 5083/ER5356 welds. Failure occurred preferentially in the soft heat-affected zone on the 6061 side of the weld, with coarse

second phase particles in the high temperature HAZ acting as crack initiation sites during fatigue testing in air. The fully automatic welds appear to be more corrosion fatigue resistant than the semi-automatic welds. This can be attributed to the greater availability of welding defects, such as gas pores, at the fusion line in the semi-automatic welds. In a NaCl solution, the coarse overaged second phase particles not only promote crack initiation by acting as stress raisers during testing, but also accelerate pit formation in the HAZ, resulting in reduced fatigue life.

The fatigue damage ratio (DR) curves of dissimilar welds joining 5083-H111 and 6061-T651 aluminium using ER5356 filler wire are shown in Figure 4.69. The semi-automatic welds appear to be affected more than the fully automatic welds by the presence of a corrosive environment. It is postulated that the greater availability of welding defects at the fusion line of the semi-automatic welds accelerates pit initiation and growth in the high temperature heat-affected zone on the 6061 side of the joint, promoting rapid fatigue crack initiation. The higher corrosion resistance of the 5083-H111 base metal compared to the 6061-T651 plate material, may have accelerated corrosive attack due to a weak galvanic effect. The effect of pitting corrosion on the corrosion fatigue properties is less evident at higher applied stress values, probably due to the lower number of cycles to failure and less time available for interaction with the corrosive environment.

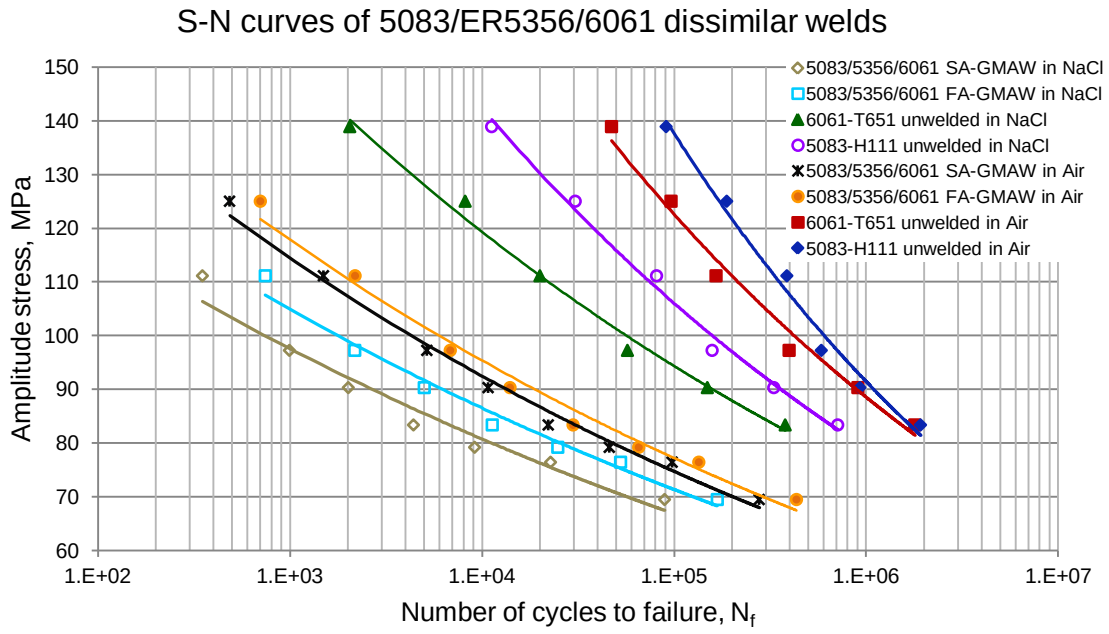

Figure 4.68. Fatigue properties of 508/ER5356/6061 dissimilar welds tested in air and in a 3.5% NaCl solution.

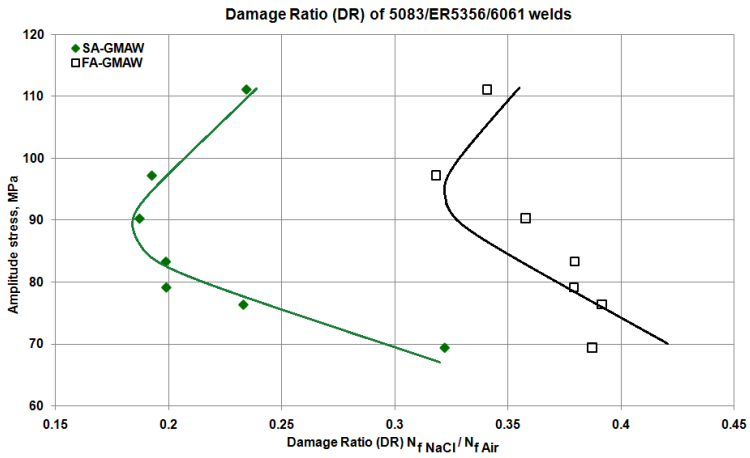

Figure 4.69. Fatigue damage ratio of dissimilar welds of 5083-H111 and 6061-T651 welded with ER5356 filler wire.

4.5.4.2 Dissimilar welds joining 5083-H111 and 6061-T651 using ER5183 filler wire:

The fatigue properties in air and NaCl of dissimilar welds of 5083-H111 and 6061-T651 aluminium joined using ER5183 filler wire are shown in Figure 4.70. A similar trend to that shown in Figure 4.68 is evident, with the semi-automatic welds performing markedly worse than the fully automatic welds in a 3.5% NaCl solution. Failure occurs preferentially in the HAZ of the 6061-T651 material due to overageing and softening. A higher incidence of welding defects at the fusion line in the semi-automatic welds accelerated fatigue failure in air by creating preferential crack initiation sites. In NaCl these welding defects promoted pit formation, leading to rapid failure.

The fatigue damage ratio (DR) values of dissimilar welds of 5083-H111 and 6061-T651 aluminium alloys with ER5183 filler metal are shown on Figure 4.71. The curves appear similar to those measured for 6061 welded with ER5183 filler wire (Figure 4.64), suggesting that the fatigue properties of the 6061 material dominate the total fatigue performance of the joint.

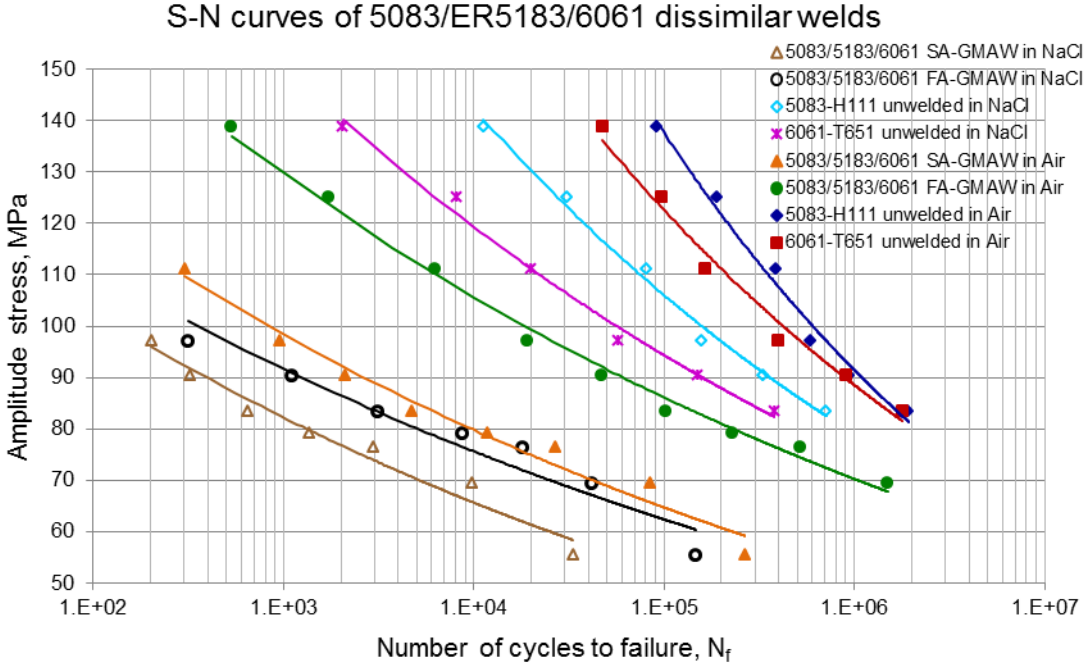

Figure 4.70. Fatigue properties of 5083-H111/ER5183/6061-T651 dissimilar welds tested in air and in a 3.5% NaCl solution.

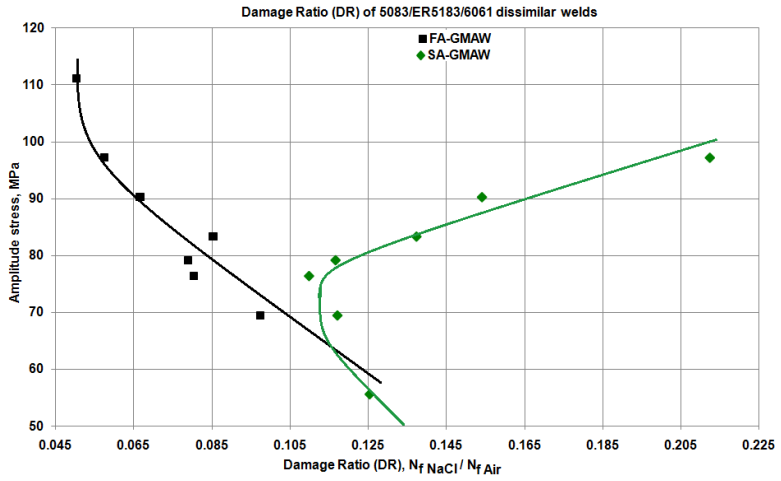

Figure 4.71. Fatigue damage ratio of dissimilar welds of 5083-H111 and 6061-T651 aluminium joined using ER5183 filler metal.

4.5.4.3 Dissimilar welds joining 5083-H111 and 6061-T651 using ER4043 filler wire:

The fatigue properties in air and NaCl of dissimilar welds of 5083-H111 and 6061-T651 aluminium joined using ER4043 filler wire are shown in Figure 4.72. Welding reduced the fatigue properties significantly, with failure occurring preferentially in the softened HAZ on the 6061 side of the welded joints in all cases. Semi-automatic and fully automatic welds displayed similar properties during testing in air. This is in agreement with the trend observed in Figure 4.65 for alloy 6061 welded using ER4043 filler wire. The semi-automatic welds performed markedly worse than the fully automatic welds on testing in a 3.5% NaCl solution. This suggests that the higher incidence of welding defects at the fusion line in the semi-automatic welds accelerated fatigue failure by promoting pit formation in the HAZ, leading to accelerated fatigue failure.

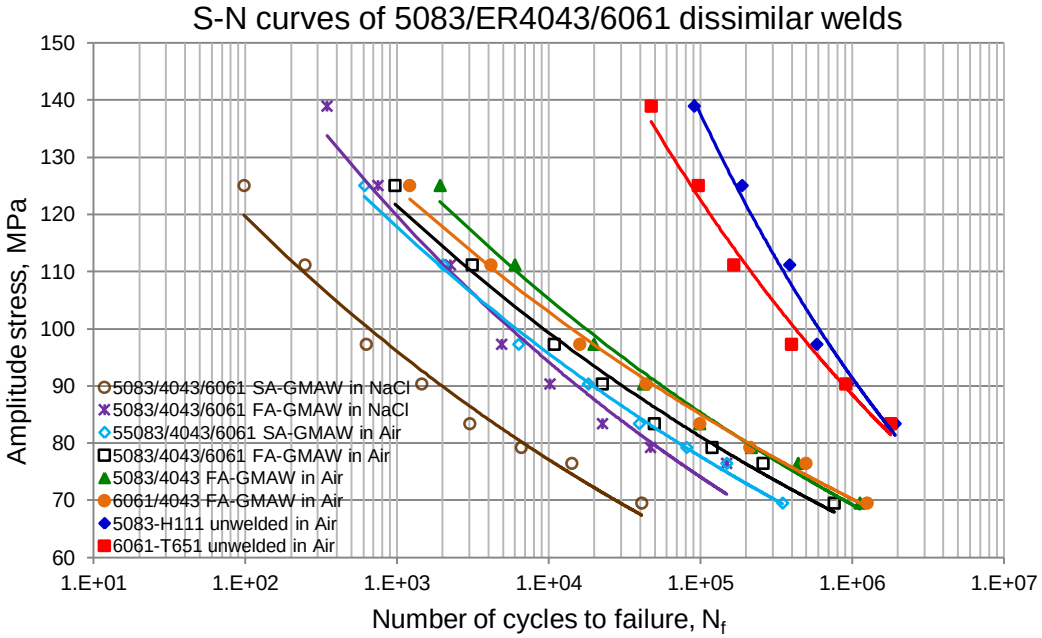

Figure 4.72. Fatigue properties of 5083-H111/ER4043/6061-T651 dissimilar welds tested in air and in a 3.5% NaCl solution.

The fatigue damage ratio (DR) curves of dissimilar welds of 5083-H111 and 6061-T651 joined using ER4043 filler wire are shown in Figure 4.73. The curves appear similar to those measured for 6061-T651 welded with ER4043 filler wire (Figure 4.67), suggesting that the fatigue properties of the 6061 material dominate the total fatigue performance of the joint.

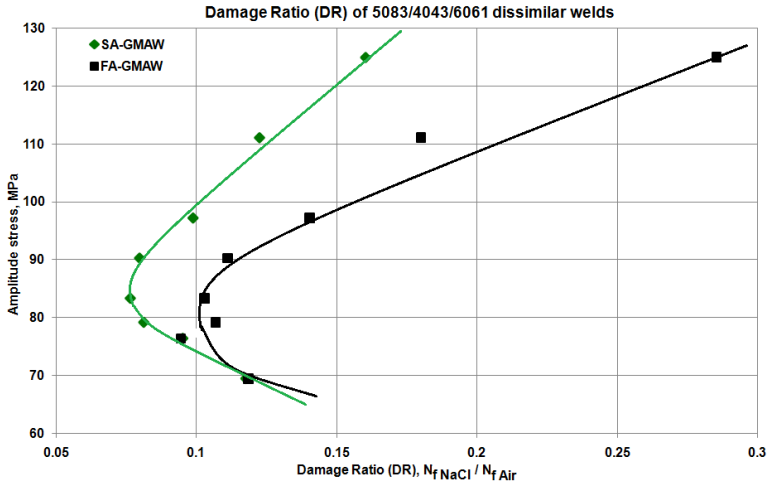

Figure 4.73. Fatigue damage ratio of dissimilar welds of 5083-H111 and 6061-T651 aluminium joined using E4043 filler metal.

4.6 Summary of results

The results presented in this chapter confirm that the fatigue properties of 5083-H111 and 6061-T651 aluminium are adversely affected by welding. Undressed welds generally display inferior fatigue properties compared to fully dressed welds due to the stress raisers introduced by the change in geometry at the weld toes and the weld root. As a result of improved control over the weld profile and a lower incidence of weld defects, fully automatic welds consistently outperformed semi-automatic welds during fatigue testing.

Fatigue cracks in fully dressed 5083-H111 welds preferentially initiated in the weld metal at defects such as gas pores, lack-of-fusion type defects and incomplete weld penetration. In the as-welded (undressed) condition, cracks initiated at the stress concentration caused by the weld toes or the weld root. In the 6061-T651 welds, failure occurred preferentially in the heat-affected zone. This region generally displays very low hardness after welding due to partial dissolution or overageing of strengthening precipitates, and recrystallization of any cold worked material. Fatigue failure was accelerated by the presence of a corrosive environment due to the formation of corrosion pits. These pits initiated preferentially at weld defects or coarse second phase particles and facilitated rapid fatigue crack initiation during testing.

The influence of filler metal selection on the mechanical properties of the welds is discussed below.

4.6.1 Effect of filler wire selection on the mechanical properties of 5083-H111 aluminium welds

The influence of filler metal selection (ER4043, ER5183 or ER5356) on the transverse tensile properties of welds in 5083-H111 aluminium is shown in Figure 4.74. The tensile strength of 5083-H111 welded with ER5356 is similar to that of the base metal, but the ductility is considerably lower. Welds performed using ER5183 filler wire display excellent ductility,

good tensile strength, but low yield stress, whereas welds performed using ER4043 filler metal display poor strength and ductility.

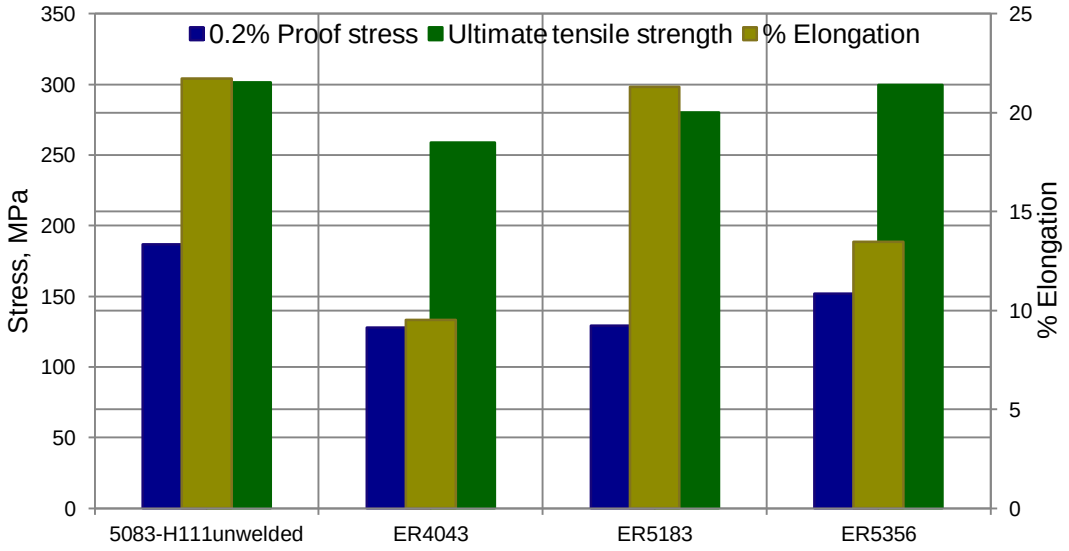

Figure 4.74. Tensile properties of dressed welds in 5083-H111 aluminium alloy joined using ER4043, ER5183 and ER5356 filler wires (fully automatic pulsed GMAW).

Figure 4.75 presents the fatigue properties of 5083-H111 welded using ER4043, ER5183 and ER5356 in air. Although the fatigue properties are very similar, the weld performed using ER5183 filler wire displays slightly longer fatigue life. The good fatigue resistance of the ER5183 welds can probably be attributed to a good combination of high strength and excellent ductility.

The corrosion fatigue properties of fully automatic welds in 5083-H111 aluminium, tested in a 3.5% NaCl solution, are presented in Figure 4.76 for ER5356, ER5183 and ER4043 filler wires. Exposure to a corrosive medium during fatigue testing reduced the fatigue life significantly, but despite the observed differences in mechanical properties, filler metal selection had very little effect on the corrosion fatigue properties. All three welds displayed similar corrosion fatigue properties during testing in a 3.5% NaCl solution.

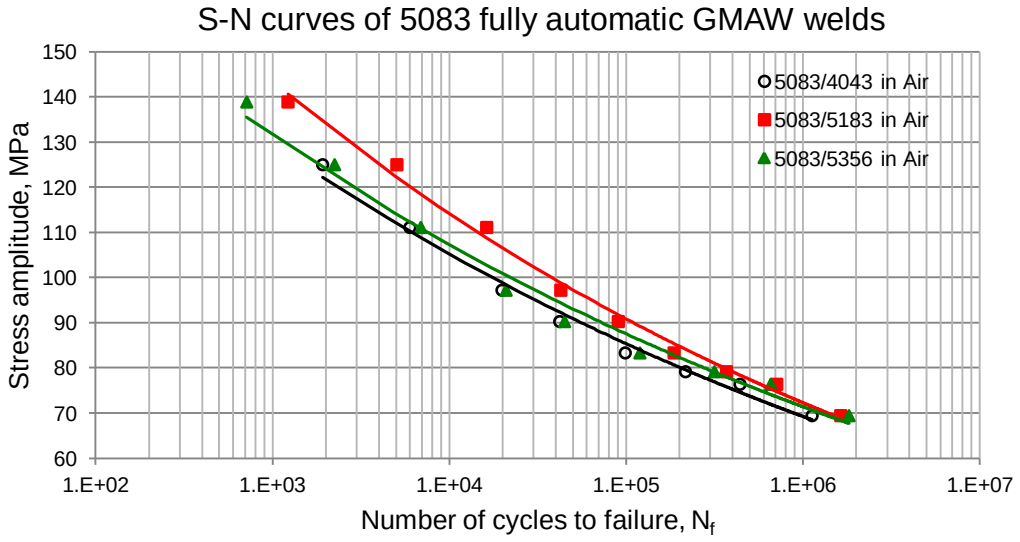

Figure 4.75. Fatigue properties of fully automatic welds in 5083-H111 performed using ER5356, ER5183 or ER4043 filler wire.

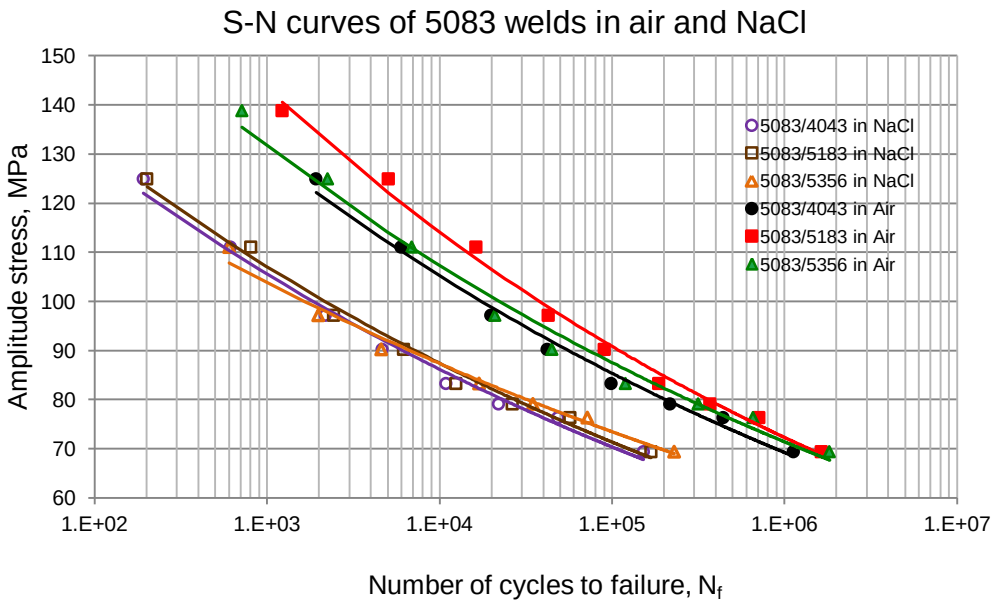

Figure 4.76. Corrosion fatigue properties of fully automatic welds in 5083-H111 performed using ER5356, ER5183 or ER5356 filler wire.

The results described above indicate that filler metal selection has little influence on the fatigue or corrosion fatigue properties of 5083-H111 aluminium. ER5356 or ER5183 filler metal is recommended for joining this alloy, with ER5356 yielding high strength welds and ER5183 providing for a good combination of high strength and excellent ductility. Fully automatic welding, with its good control over weld dimensions and its lower defect content, ensures optimal resistance to fatigue failure.

4.6.2 Effect of filler wire selection on the mechanical properties of 6061-T651 aluminium welds

As shown in Figure 4.77, filler metal selection (ER4043, ER5183 or ER5356) had virtually no effect on the transverse tensile properties of welds in 6061-T651 aluminium. All the welds tested during the course of this investigation displayed significantly lower tensile properties than those of the base metal, regardless of the filler material used. This can be attributed to the observation that failure occurred in the softened heat-affected zone of all the 6061-T651 welds (for dressed welds).

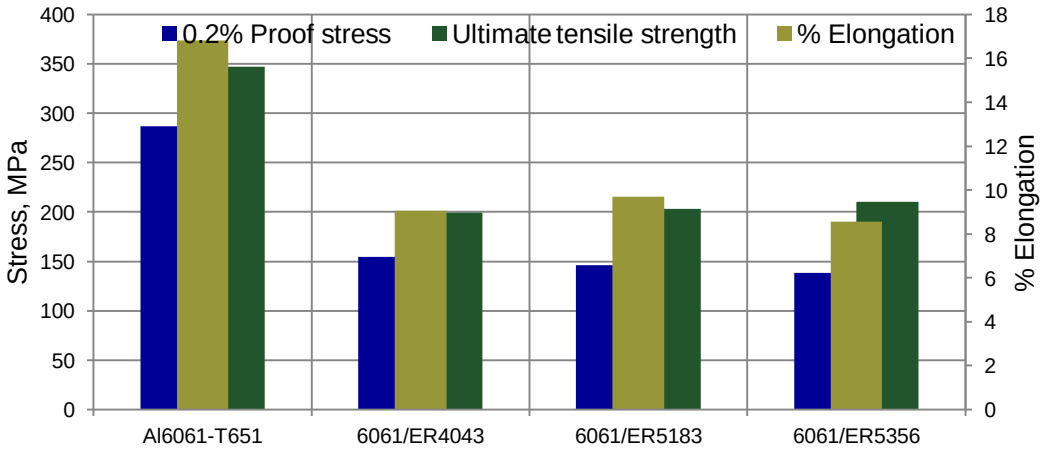

*Figure **Error! No text of specified style in document.**4.77. Tensile properties of dressed welds in 6061-T651 aluminium joined using ER4043, ER5183 and ER5356 filler wires (fully automatic pulsed GMAW).*

The fatigue properties of 6061-T651 welded using ER4043, ER5183 or ER5356 filler wire (tested in air and in a 3.5% NaCl solution), are represented in Figure 4.78 and 4.79. It is evident that the fatigue life of 6061-T651 welds is significantly reduced by welding. Cracking occurs preferentially in the heat-affected zone, therefore filler wire selection had little influence on the fatigue properties of 6061-T651 aluminium welds. Welds performed using ER5356 filler wire performed slightly better than ER5183 welds in air, with ER4043 welds displaying the lowest fatigue properties. The difference in the number of cycles to failure at higher amplitude stress levels can be attributed to a combination of a higher incidence of weld defects and a lower hardness in heat-affected-zone in the case of ER5183 and ER4043 welds.

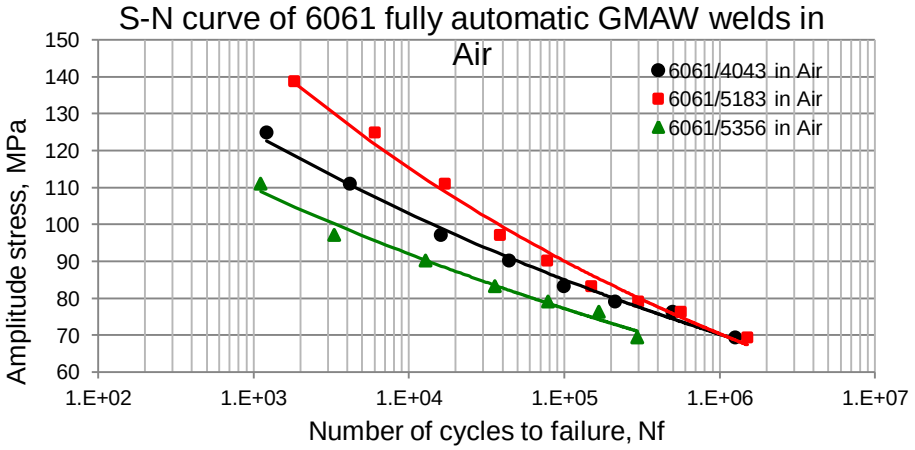

Figure 4.78. Fatigue properties of fully automatic welds in 6061-T651 performed using ER4043, ER5183 or ER5356 filler wire (tested in air).

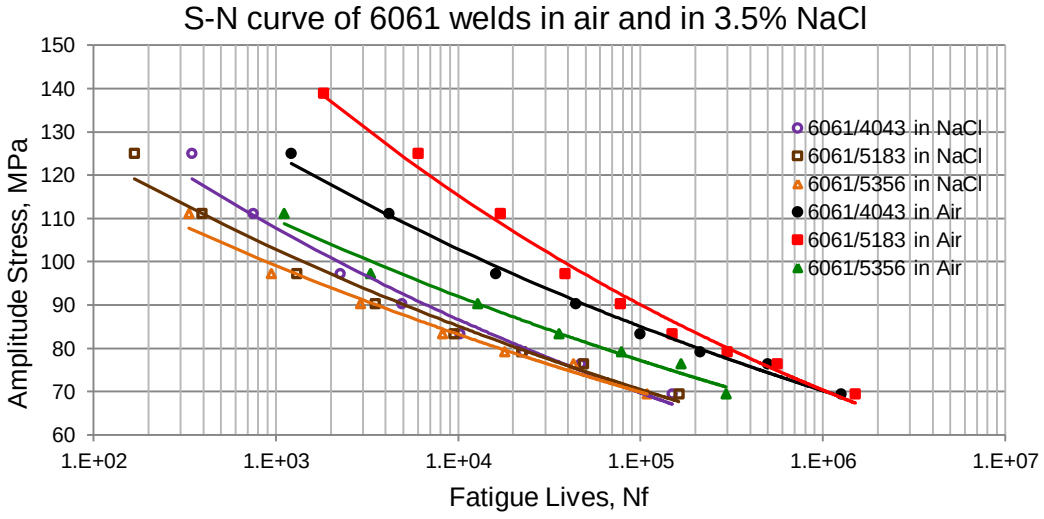

Figure 4.79. Fatigue properties of fully automatic welds in 6061-T651 performed using ER4043, ER5183 or ER5356 filler wire (tested in 3.5% NaCl solution).

The presence of a 3.5% NaCl corrosive environment during fatigue testing reduced the fatigue properties of 6061-T651 welds well below those measured in air. This can be attributed to the presence of corrosion pits which act as preferential crack initiation sites during fatigue testing. Failure occurred in the heat-affected zone of all welds. No statistically relevant differences were observed between welds produced with different filler materials.

CHAPTER 5. CONCLUSIONS AND RECOMMENDATIONS

This investigation studied the effect of semi-automatic or fully automatic pulsed gas metal arc welding using ER5356, ER5183 or ER4043 filler wire on the mechanical properties, fatigue resistance and corrosion fatigue behaviour (measured in a 3.5% NaCl solution) of wrought aluminium alloys 5083-H111 and 6061-T651.

5083-H111 aluminium:

Arc welding reduces the strength and ductility of 5083-H111 joints, with the near-matching magnesium-alloyed welding consumables (ER5356 and ER5183) delivering the best combination of strength and ductility. Hardness profiles measured across the welds revealed a significant reduction in the hardness of the weld metal compared to that of the base material, regardless of the consumable (ER5356, ER5183 or ER4043) used.

As a result of the low weld metal hardness, fatigue failure occurred preferentially in the weld metal of dressed welds (with preferential crack initiation at discontinuities such as gas pores, lack-of-fusion type defects or incomplete penetration) or at the stress concentrations introduced by the change in geometry at the weld toes or weld root of undressed welds. Filler metal selection had very little influence on the weld fatigue properties, but dressing of the welds to remove geometrical stress concentrations improved the weld fatigue properties considerably. As a result of improved control over weld profile and defects levels, fully automatic welds consistently outperformed semi-automatic welds with regards to fatigue performance.

The presence of a corrosive environment reduced the fatigue life of 5083-H111 welds by at least an order of magnitude. On exposure to the NaCl solution, corrosion pits formed at pre-existing weld defects and second phase particles in the weld metal and at the weld/HAZ interface. These corrosion pits introduced severe local stress concentrations and accelerated fatigue crack initiation and failure. Filler metal selection had no discernable effect on the fatigue life of 5083-H111 welds in a 3.5% NaCl solution.

6061-T651 aluminium:

Welding resulted in a significant reduction in hardness in the heat-affected zone adjacent to the weld. This reduction in hardness can be attributed to partial dissolution and coarsening of strengthening precipitates, grain growth and recrystallization during welding. During transverse tensile testing, failure occurred preferentially in the softened HAZ of all the welds (dressed and undressed), resulting in low strength and ductility.

The fatigue life of 6061-T651 welds was reduced significantly compared to unwelded base metal under similar test conditions. As a result of the low heat-affected zone hardness, fatigue failure occurred preferentially at the weld/HAZ or HAZ/base metal interface of all the welds. Since failure occurred in the HAZ, filler metal selection had little influence on the fatigue properties of the welds. Fully automatic welds generally outperformed semi-automatic welds during fatigue testing due to the lower incidence of weld defects at the fusion line.

The introduction of a chloride-containing environment during fatigue testing resulted in a significant reduction in the fatigue life of 6061-T651 welds (more than an order of magnitude). Fatigue cracks initiated preferentially in the softened HAZ at corrosion pits. These pits initiated rapidly at coarse second phase particles in the HAZ. Filler metal selection had no discernable influence on the fatigue life of 6061-T651 welds tested in a 3.5% NaCl solution.

Future work:

Due to the importance of aluminium alloys in the manufacture of tank container vessels for transporting various liquids, it is proposed that the corrosion fatigue behaviour of 5083-H111 and 6061-T651 in other corrosive environments (such as various fruit juices) be evaluated. The effect of postweld heat treatment of 6061-T651 welds (to improve the mechanical properties of the heat-affected zone) on the fatigue and corrosion-fatigue properties will also be investigated.

The results indicate that crack initiation from corrosion pit sites can be extremely fast at high stress levels and can occur even from relatively small pits. As for the crack initiation predictions, there seems to be (based on very limited experimental data), a stress level dependency with regards to the form and magnitude of the effect of cyclic stress on pit growth and crack initiation. This may call for some modifications in the formulations (based on more experimental data) and deeper understanding of the phenomenon. Due to the random process of corrosion pit initiation, a stochastic-deterministic approach may be called for. Future work will attempt to address some of these issues.

BIBLIOGRAPHY

[1] Davis, J.R. (ed.). 1998. "Aluminum and Aluminum Alloys", published in "Alloying: Understanding the Basics". ASM International, Metals Park, Ohio, USA.

[2] Aluminum Association Inc. 2001. "International Alloy Designations and Chemical Composition Limits for Wrought Aluminum and Wrought Aluminum Alloys". Aluminium Association In., Arlington, Virginia, USA.

[3] Hatch, J.E. (ed.). 1984. "Aluminium: Properties and Physical Metallurgy". ASM International, Metals Park, Ohio, USA.

[4] ASM Handbook, vol. 6 "Welding, Brazing, and Soldering". 1993. ASM International, Metals Park, Ohio, USA.

[5] Wilcox, D.V., Adkins, H., Dickerson, P.B., Hasemeyer, E.A. & Lockwood, L. 1972. "Welding Aluminum" 6th edition. American Welding Society, Miami, Florida, USA. pp. 69.2-69.25.

[6] Praveen, P. & Yarlagadda, P.K.D.V. 2005. "Meeting challenges in welding of aluminium alloys through pulse gas metal arc welding". Journal of Materials Processing Technology", vol. 164-165. pp. 1106-1112.

[7] Lean, P.P., Gil, L. & Ureña, A. 2003. "Dissimilar welds between unreinforced AA6082 and AA6092/Si/25p composite by pulsed-MIG arc welding using unreinforced filler alloys (Al-5Mg and Al-5Si)". Journal of Materials Processing Technology, vol. 143-144. pp. 846-850.

[8] Potluri, N.B., Ghosh, P.K., Gupta, P.C. & Reddy, Y.S. 1996. "Studies on weld metal characteristics and their influence on tensile and fatigue properties of pulsed-current GMA welded Al-Zn-Mg alloy". Welding Journal, vol. 75, no. 2. pp. 62s-70s.

[9] Vargel, C. 2004. "Corrosion of Aluminium", 1st edition. Elsevier, Boston, USA. pp. 92-124.

[10] Jones, D.A. 1996. "Principles and Prevention of Corrosion", 2nd edition. Prentice-Hall, Upper Saddle River, USA. pp. 200-220, 236-247, 262-263, 279-285, 307, 309-316, 322.

[11] Maggiolino, S. & Schmid, C. 2008. "Corrosion resistance in FSW and in MIG welding techniques of AA6XXX". Journal of Materials Processing Technology, vol. 197, no. 1-3. pp. 237-240.

[12] ASM Handbook, vol. 13A "Corrosion: Fundamantals, Testing and Protection". 2003. ASM International, Metals Park, Ohio, USA.

[13] Winkler, S.L., Ryan, M.P. & Flower, H.M. 2004. "Pitting corrosion in cast 7XXX aluminium alloys and fibre reinforced MMCs". Corrosion Science, vol. 46, no. 4. pp. 893-902.

[14] Chen, G.S., Gao, M. & Wei, R.P. 1996. "Microconstituent-induced pitting corrosion in aluminum alloy 2024-T3". Corrosion, vol. 52, no. 1. pp. 8-15.

[15] Ralston, K.D., Birbilis, N., Weyland, M. & Hutchinson, C.R. "The effect of precipitate size on the yield strength-pitting corrosion correlation in Al-Cu-Mg alloys". Acta Materialia (in press).

[16] Ahlatci, H. 2010. "Production and corrosion behaviours of the Al-12Si-XMg alloys containing in-situ Mg_2Si particles". Journal of Alloys and Compounds, vol. 503, no. 1. pp. 122-126.

[17] Czechowski, M. 2004. "Corrosion Fatigue of GMA Al-Mg alloy". Advances in Materials Science, vol. 4. pp. 16-24.

[18] Ambriz, R.R., Barrera, G., García, R. & López, V.H. 2009. "A comparative study of the mechanical properties of 6061-T6 GMA welds obtained by the indirect electric arc (IEA) and the modified indirect electric arc (MIEA)". Materials & Design, vol. 30, no. 7. pp. 2446-2453.

[19] Huskins, E.L., Cao, B. & Ramesh, K.T. 2010. "Strengthening mechanisms in an Al–Mg alloy". Materials Science and Engineering A, vol. 527, no. 6. pp. 1292-1298.

[20] Dutta, I. & Allen, S.M. 1991. "A calorimetric study of precipitation in commercial aluminium alloy 6061". Journal of Materials Science Letters, vol. 10, no. 6. pp. 323-326.

[21] Maddox, S.J. 1991. "Fatigue Strength of Welded Structures", 2nd edition. Abington Publishing, Cambridge, UK. pp. 19-43, 66-70.

[22] Ninh Nguyen, T. & Wahab, M.A. 1995. "A theoretical study of the effect of weld geometry parameters on fatigue crack propagation life". Engineering Fracture Mechanics, vol. 51, no. 1. pp. 1-18.

[23] ASM Handbook, vol. 19 “Fatigue and Fracture”. 1996. ASM International, Metals Park, Ohio, USA.

[24] Geoffroy, N., Vittecoq, E., Birr, A., De Mestral, F. & Martin, J.-M. 2007. “Fatigue behaviour of an arc welded Al–Si–Mg alloy”. Scripta Materialia, vol. 57, no. 4. pp. 349-352.

[25] Teng, T.-L., Fung, C.-P. & Chang, P.-H. 2002. “Effect of weld geometry and residual stresses on fatigue in butt-welded joints”. International Journal of Pressure Vessels and Piping, vol. 79, no. 7. pp. 467-482.

[26] Zheng, Z.Q., Cai, B., Zhai, T. & Li, S.C. 2011. “The behaviour of fatigue crack initiation and propagation in AA2524-T35 alloy”. Materials Science and Engineering A, vol. 528, no. 4-5. pp. 2017-2022.

[27] Kumar, M. & Guha, B. 1993. "Fatigue characteristics of ‘bead-on-plate’ of aluminum and AlZnMg alloy". Theoretical and Applied Fracture Mechanics, vol. 19, no. 2. pp. 151-156.

[28] Benachour, M., Benguediab, M., Hadjoui, A., Hadjoui, F. & Benachour, N. 2008. "Fatigue crack growth of a double fillet weld". Computational Materials Science, vol. 44, no. 2. pp. 489-495.

[29] Ishihara, S., Saka, S., Nan, Z.Y., Goshima, T. & Sunada, S. 2006. “Prediction of corrosion fatigue lives of aluminium alloy on the basis of corrosion pit growth law”. Fatigue and Fracture of Engineering Materials and Structures, vol. 29, no. 6. pp. 472-480.

[30] Rokhlin, S.I., Kim, J.-Y., Nagy, H. & Zoofan, B. 1999. “Effect of pitting corrosion on fatigue crack initiation and fatigue life”. Engineering Fracture Mechanics, vol. 62, no. 4-5, pp. 425-444.

[31] Pidaparti, R.M. & Patel, R.R. 2008. “Correlation between corrosion pits and stresses in Al alloys”. Materials Letters, vol. 62, no. 30. pp. 4497-4499.

[32] Pidaparti, R.M. & Rao, A.S. 2008. “Analysis of pits induced stresses due to metal corrosion”. Corrosion Science, vol. 50, no. 7. pp. 1932-1938.

[33] Chlistovsky, R.M., Heffernan, P.J. & DuQuesnay, D.L. 2007. “Corrosion-fatigue behaviour of 7075-T651 aluminum alloy subjected to periodic overloads”. International Journal of Fatigue, vol. 29, no. 9-11. pp. 1941-1949.

[34] Chen, G.S., Wan, K.-C., Gao, M., Wei, R.P. & Fluornoy, T.H. 1996. “Transition from pitting to fatigue crack growth – Modeling of corrosion fatigue crack nucleation in a 2024-T3 aluminum alloy”. Materials Science and Engineering A, vol. 219, no. 1-2. pp. 126-132.

[35] ASTM E3-01 (2007) “Standard Guide for Preparation of Metallographic Specimens”. ASTM International, West Conshohocken, PA, USA.

[36] ASTM E340-00 (2006) “Standard Test Method for Macroetching Metals and Alloys”. ASTM International, West Conshohocken, PA, USA.

[37] ASTM E384-10 (2010) “Standard Test Method for Knoop and Vickers Hardness of Materials”. ASTM International, West Conshohocken, PA, USA.

[38] ASTM E8/E8M-09 (2009) “Standard Test Methods for Tension Testing of Metallic Materials”. ASTM International, West Conshohocken, PA, USA.

[39] ASTM G1-03 (2003) “Standard Practice for Preparing, Cleaning, and Evaluating Corrosion Test Specimens”. ASTM International, West Conshohocken, PA, USA.

[40] ASTM G31-72 (2004) “Standard Practice for Laboratory Immersion Corrosion Testing of Metals”. ASTM International, West Conshohocken, PA, USA.

[41] ASTM G44-99 (2005) “Standard Practice for Exposure of Metals and Alloys by Alternate Immersion in Neutral 3.5% Sodium Chloride Solution”. ASTM International, West Conshohocken, PA, USA.

[42] ASTM G46-94 (2005) “Standard Guide for Examination and Evaluation of Pitting Corrosion”. ASTM International, West Conshohocken, PA, USA.

[43] ASTM E466-07 (2007) "Standard Practice for Conducting Force Controlled Constant Amplitude Axial Fatigue Tests of Metallic Materials". ASTM International, West Conshohocken, PA, USA.

[44] ASTM E739-10 (2010) "Standard Practice for Statistical Analysis of Linear or Linearized Stress-Life (S-N) and Strain-Life (ε-N) Fatigue Data". ASTM International, West Conshohocken, PA, USA.

[45] ASTM E467-08 (2008) "Standard Practice for Verification of Constant Amplitude Dynamic Forces in an Axial Fatigue Testing System". ASTM International, West Conshohocken, PA, USA.

APPENDIX I. Pitting corrosion of 5083-H111 and 6061-T651 in the as-supplied condition.

Pit dimensions measured in 5083-H111 after immersion in a 3.5% NaCl solution (dissolved oxygen content of 5.5 to 9 ppm, pH ≈ 7) for 3 days.

	Pit Depth [µm]	*Pit Length [µm]*	*Pit Width [µm]*
	2.00	1.00	1.00
	1.00	0.50	0.50
	3.00	2.00	2.00
	2.00	0.50	1.00
	0.50	0.50	1.00
	0.50	1.00	1.00
	0.50	0.50	1.00
	3.00	2.00	2.00
	2.00	1.00	1.00
	2.00	1.50	2.00
	1.00	1.00	1.00
	2.00	1.00	0.50
	2.00	1.00	1.50
Mean	1.65	1.04	1.19
Maximum	3.00	2.00	2.00
Minimum	0.50	0.50	0.50
Median	2.00	1.00	1.00
Standard deviation	0.88	0.52	0.52

Pit dimensions measured in 5083-H111 after immersion in a 3.5% NaCl solution (dissolved oxygen content of 5.5 to 9 ppm, pH ≈ 7) for 30 days.

	Pit Depth [µm]	*Pit Length [µm]*	*Pit Width [µm]*
	44.00	43.00	16.00
	23.00	14.00	6.00
	63.00	65.00	37.00
	72.00	53.00	46.00
	38.00	63.00	25.00
	36.00	23.00	31.00
	28.00	37.00	23.00
	38.00	18.00	11.00
	42.00	42.00	28.00
	43.00	20.00	14.00
	4.00	7.00	7.00
	6.00	26.00	24.00
	5.00	10.00	9.00
Mean	34.00	32.38	21.31
Maximum	72.00	65.00	46.00
Minimum	4.00	7.00	6.00
Median	38.00	26.00	23.00
Standard deviation	20.91	19.63	12.24

Pit dimensions measured in 5083-H111 after immersion in a 3.5% NaCl solution (dissolved oxygen content of 5.5 to 9 ppm, pH ≈ 7) for 90 days.

	Pit Depth [µm]	*Pit Length [µm]*	*Pit Width [µm]*
	198.00	175.00	65.00
	5.00	29.00	26.00
	7.00	104.00	156.00
	10.00	40.00	46.00
	323.00	212.00	117.00
	223.00	251.00	57.00
	197.00	94.00	28.00
	367.00	148.00	101.00
	104.00	57.00	38.00
	283.00	262.00	192.00
	170.00	71.00	105.00
	171.00	168.00	131.00
	125.00	81.00	97.00
Mean	167.92	130.15	89.15
Maximum	367.00	262.00	192.00
Minimum	5.00	29.00	26.00
Median	171.00	104.00	97.00
Standard deviation	117.27	78.56	51.52

Pit dimensions measured in 6061-T651 after immersion in a 3.5% NaCl solution (dissolved oxygen content of 5.5 to 9 ppm, pH ≈ 7) for 7 days.

	Pit Depth [µm]	*Pit Length [µm]*	*Pit Width [µm]*
	39.00	27.51	17.75
	42.00	14.84	14.76
	14.00	9.90	9.90
	35.00	19.98	18.32
	21.00	18.86	11.47
	44.00	16.50	16.90
	23.00	10.96	19.92
	44.00	31.39	31.82
	46.00	37.02	25.46
	48.00	32.45	22.20
	39.00	30.76	32.70
	45.00	44.78	34.70
	47.00	51.77	20.29
	12.00	14.58	11.33
	39.00	27.57	30.54
Mean	35.87	25.93	21.20
Maximum	48.00	51.77	34.70
Minimum	12.00	9.90	9.90
Standard deviation	12.22	12.40	8.18

Pit dimensions measured in 6061-T651 after immersion in a 3.5% NaCl solution (dissolved oxygen content of 5.5 to 9 ppm, pH ≈ 7) for 45 days.

	Pit Depth [µm]	*Pit length[µm]*	*Pit Width [µm]*
	122.00	36.93	42.81
	132.00	87.04	76.14
	132.00	57.59	76.94
	148.00	111.47	82.93
	169.00	95.78	59.65
	171.00	61.70	38.53
	177.00	75.91	69.92
	182.00	46.58	57.25
	188.00	46.58	56.45
	200.00	121.12	111.99
	214.00	83.90	78.20
	250.00	59.48	50.74
Mean	173.75	73.67	66.80
Maximum	250.00	121.12	111.99
Minimum	122.00	36.93	38.53
Median	174.00	68.81	66.80
Standard deviation	37.25	26.76	20.26

APPENDIX II. Fatigue properties.

Fatigue properties of as-supplied 5083-H111 in air.

Air	*Number of cycles to failure, N_f*						
S_a [MPa]	*Test 1*	*Test 2*	*Test 3*	*Mean*	*Median*	*Stdv*	*CV*
138.9	88484	91123	94456	91354	91123	2993	0.03
125.0	188484	190125	177149	185253	188484	7066	0.04
111.1	368254	387529	391878	382554	387529	12573	0.03
97.2	597245	585725	572498	585156	585725	12383	0.02
90.3	906435	930235	951246	929305	930235	22420	0.02
83.3	1870123	1998456	1923548	1930709	1923548	64465	0.03

Fatigue properties of as-supplied 5083-H111 in 3.5% NaCl.

NaCl	*Number of cycles to failure, N_f*						
S_a [MPa]	*Test 1*	*Test 2*	*Test 3*	*Mean*	*Median*	*Stdv*	*CV*
138.9	11254	13542	10987	11928	11254	1404	0.12
125.0	30646	31654	29875	30725	30646	892	0.03
111.1	84158	81254	79857	81756	81254	2194	0.03
97.2	158214	157235	165214	160221	158214	4352	0.03
90.3	378785	331356	301256	337132	331356	39086	0.12
83.3	758654	698789	712859	723434	712859	31302	0.04

Fatigue properties of as-supplied 6061-T651 in air.

Air	*Number of cycles to failure, N_f*						
S_a [MPa]	*Test 1*	*Test 2*	*Test 3*	*Mean*	*Median*	*Stdv*	*CV*
138.9	47365	45239	49025	47210	47365	1898	0.04
125.0	94923	98725	96712	96787	96712	1902	0.02
111.1	165815	170267	162893	166325	165815	3714	0.02
97.2	401542	398256	388286	396028	398256	6903	0.02
90.3	908400	911142	889252	902931	908400	11926	0.01
83.3	1796000	176987	1829821	1267603	1796000	944652	0.75

Fatigue properties of as-supplied 6061-T651 in 3.5% NaCl.

NaCl	*Number of cycles to failure, N_f*						
S_a [MPa]	*Test 1*	*Test 2*	*Test 3*	*Mean*	*Median*	*Stdv*	*CV*
138.9	2154	1965	2054	2058	2054	95	21.76
125.0	8411	8192	7887	8163	8192	263	31.02
111.1	21164	19879	20069	20371	20069	694	29.37
97.2	59356	53458	57325	56713	57325	2996	18.93
90.3	151795	149368	142958	148040	149368	4566	32.42
83.3	395801	341231	379872	372301	379872	28062	13.27

Fatigue properties of semi-automatic 5083-H111/ER5356 dressed welds in air.

Air	*Number of cycles to failure, N_f*						
S_a [MPa]	*Test 1*	*Test 2*	*Test 3*	*Mean*	*Median*	*Stdv*	*CV*
125.0	285	356	209	283	285	74	0.26
111.1	1241	1463	1005	1236	1241	229	0.19
97.2	3968	5268	4325	4520	4325	672	0.15
90.3	13046	10846	14223	12705	13046	1714	0.13
83.3	35400	27984	30245	31210	30245	3801	0.12
79.2	43132	49353	39245	43910	43132	5099	0.12
76.4	70658	69658	102012	80776	70658	18398	0.23
69.4	270524	362035	335807	322789	335807	47124	0.15

Fatigue properties of as-welded semi-automatic 5083-H111/ER5356 welds in air.

Air	*Number of cycles to failure, N_f*						
S_a [MPa]	*Test 1*	*Test 2*	*Test 3*	*Mean*	*Median*	*Stdv*	*CV*
125.0	41	28	19	29	28	11	0.38
111.1	148	104	97	116	104	28	0.24
97.2	346	286	310	314	310	30	0.10
90.3	1257	1131	1098	1162	1131	84	0.07
83.3	4039	3987	3791	3939	3987	131	0.03
79.2	12858	14515	11578	12983	12858	1473	0.11
76.4	46221	41523	5928	31224	41523	22033	0.71
69.4	131235	165035	148928	148399	148928	16906	0.11

Fatigue properties of fully automatic 5083-H111/ER5356 dressed welds in air.

Air	*Number of cycles to failure, N_f*						
S_a [MPa]	*Test 1*	*Test 2*	*Test 3*	*Mean*	*Median*	*Std*	*CV*
138.9	276	298	301	292	298	14	0.05
125.0	1108	987	969	1021	987	76	0.07
111.1	3105	2908	2879	2964	2908	123	0.04
97.2	11072	10985	9701	10586	10985	768	0.07
90.3	32945	29254	30945	31048	30945	1848	0.06
83.3	109826	121653	119826	117102	119826	6367	0.05
79.2	281230	316337	331230	309599	316337	25672	0.08
76.4	758550	659268	798524	738781	758550	71702	0.10
69.4	1823501	1725809	1995487	1848266	1823501	136534	0.07

Fatigue properties of as-welded fully automatic 5083-H111/ER5356 welds in air.

Air	*Number of cycles to failure, N_f*						
S_a [MPa]	*Test 1*	*Test 2*	*Test 3*	*Mean*	*Median*	*Stdv*	*CV*
125.0	102	79	92	9	92	12	0.13
111.1	329	297	289	305	297	21	0.07
97.2	1265	1014	958	1079	1014	164	0.15
90.3	3621	3264	2815	3233	3264	404	0.12
83.3	10075	9896	8923	9631	9896	620	0.06
79.2	31091	30985	29187	30421	30985	1070	0.04
76.4	106657	98102	112587	105782	106657	7282	0.07
69.4	198254	201423	251034	216904	201423	29600	0.14

Fatigue properties of semi-automatic 5083-H111/ER5356 dressed welds in 3.5% NaCl.

NaCl	*Number of cycles to failure, N_f*						
S_a [MPa]	*Test 1*	*Test 2*	*Test 3*	*Mean*	*Median*	*Stdv*	*CV*
97.2	289	261	252	267	261	19.30	0.07
90.3	816	744	851	804	816	54.56	0.07
83.3	2689	1976	1897	2187	1976	436.25	0.20
79.2	6785	5298	5729	5937	5729	765.08	0.13
76.4	18675	15723	17685	17361	17685	1502.43	0.09
69.4	46289	42963	40678	43310	42963	2821.55	0.07

Fatigue properties of fully automatic 5083-H111/ER5356 dressed welds in 3.5% NaCl.

NaCl	*Number of cycles to failure, N_f*						
S_a [MPa]	*Test 1*	*Test 2*	*Test 3*	*Mean*	*Median*	*Stdv*	*CV*
111.1	159	174	147	160	159	14	0.08
97.2	485	398	429	437	429	44	0.10
90.3	1298	1302	1219	1273	1298	47	0.04
83.3	4189	3996	3498	3894	3996	357	0.09
79.2	14876	12989	16226	14697	14876	1626	0.11
76.4	52139	49879	56193	52737	52139	3199	0.06
69.4	147653	139879	151029	146187	147653	5718	0.04

Fatigue properties of semi-automatic 6061-H111/ER5356 dressed welds in air.

Air	*Number of cycles to failure, N_f*						
S_a [MPa]	*Test 1*	*Test 2*	*Test 3*	*Mean*	*Median*	*Stdv*	*CV*
111.1	1524	717	1029	1090	1029	407	0.37
97.2	3292	3430	1958	2893	3292	813	0.28
90.3	14237	10927	9121	11428	10927	2595	0.23
83.3	45195	31244	34895	37111	34895	7235	0.19
79.2	95789	72498	61634	76640	72498	17450	0.23
76.4	172997	123568	141365	145977	141365	25035	0.17
69.4	243563	287915	348858	293445	287915	52865	0.18

Fatigue properties of as-welded semi-automatic 6061-H111/ER5356 welds in air.

Air	*Number of cycles to failure, N_f*						
S_a [MPa]	*Test 1*	*Test 2*	*Test 3*	*Mean*	*Median*	*Stdv*	*CV*
111.1	1442	719	921	1027	921	373	0.36
97.2	3712	2012	3129	2951	3129	864	0.29
90.3	14765	11534	8936	11745	11534	2920	0.25
83.3	42987	28763	33786	35179	33786	7214	0.21
79.2	71920	58468	87329	72572	71920	14442	0.20
76.4	169265	113582	147119	143322	147119	28035	0.20
69.4	351122	239187	312654	300988	312654	56872	0.19

Fatigue properties of fully automatic 6061-H111/ER5356 dressed welds in air.

Air	*Number of cycles to failure, N_f*						
S_a [MPa]	*Test 1*	*Test 2*	*Test 3*	*Mean*	*Median*	*Stdv*	*CV*
111.1	1354	1107	735	1065	1107	312	0.29
97.2	3298	4132	2265	3232	3298	935	0.29
90.3	16211	9015	12764	12663	12764	3599	0.28
83.3	29875	49120	35654	38216	35654	9875	0.26
79.2	98987	63389	78395	80257	78395	17872	0.22
76.4	187254	131675	166438	161789	166438	28080	0.17
69.4	255383	361438	294156	303659	294156	53662	0.18

Fatigue properties of as-welded fully automatic 6061-H111/ER5356 welds in air.

Air	*Number of cycles to failure, N_f*						
S_a [MPa]	*Test 1*	*Test 2*	*Test 3*	*Mean*	*Median*	*Stdv*	*CV*
111.1	1312	892	632	945	892	343	0.36
97.2	3764	2113	2974	2950	2974	826	0.28
90.3	15976	9045	12193	12405	12193	3470	0.28
83.3	28981	48076	32112	36390	32112	10241	0.28
79.2	96093	61372	76112	77859	76112	17426	0.22
76.4	181876	121654	167354	156961	167354	31427	0.20
69.4	239176	351983	287465	292875	287465	56598	0.19

Fatigue properties of as-welded semi-automatic 6061-H111/ER5356 welds in 3.5% NaCl.

NaCl	*Number of cycles to failure, N_f*						
S_a [MPa]	*Test 1*	*Test 2*	*Test 3*	*Mean*	*Median*	*Stdv*	*CV*
111.1	211	419	195	275	211	125	0.45
97.2	1396	717	687	933	717	401	0.43
90.3	2043	3711	2365	2706	2365	885	0.33
83.3	4377	8531	7931	6946	7931	2245	0.32
79.2	16519	9626	19519	15221	16519	5073	0.33
76.4	41754	51134	31154	41347	41754	9996	0.24
69.4	112263	81445	103986	99231	103986	15950	0.16

Fatigue properties of as-welded fully automatic 6061-H111/ER5356 welds in 3.5% NaCl.

NaCl	*Number of cycles to failure, N_f*						
S_a [MPa]	*Test 1*	*Test 2*	*Test 3*	*Mean*	*Median*	*Stdv*	*CV*
111.1	233	437	197	289	233	129	0.45
97.2	697	1341	742	927	742	360	0.39
90.3	2017	3619	2904	2847	2904	803	0.28
83.3	9174	5297	8189	7553	8189	2015	0.27
79.2	19945	18943	11724	16871	18943	4485	0.27
76.4	32654	42775	52197	42542	42775	9774	0.23
69.4	119678	108456	82436	103523	108456	19105	0.18

Fatigue properties of semi-automatic 5083/ER5356/6061 dissimilar dressed welds in air.

Air	*Number of cycles to failure, N_f*						
S_a [MPa]	*Test 1*	*Test 2*	*Test 3*	*Mean*	*Median*	*Stdv*	*CV*
111.1	1498	645	1004	1049	1004	428	0.41
97.2	3364	1774	2987	2708	2987	831	0.31
90.3	10786	15112	8763	11554	10786	3243	0.28
83.3	44987	27176	33879	35347	33879	8996	0.25
79.2	96117	71027	59834	75659	71027	18580	0.25
76.4	171098	109098	129879	136692	129879	31556	0.23
69.4	338956	227856	277896	281569	277896	55641	0.20

Fatigue properties of as-welded semi-automatic 5083/ER5356/6061 dissimilar welds in air.

Air	*Number of cycles to failure, N_f*						
S_a [MPa]	*Test 1*	*Test 2*	*Test 3*	*Mean*	*Median*	*Stdv*	*CV*
111.1	1398	593	878	956	878	408	0.43
97.2	3687	1628	2987	2767	2987	1047	0.38
90.3	14422	7165	10903	10830	10903	3629	0.34
83.3	39987	21176	31879	31014	31879	9435	0.30
79.2	84117	70627	47834	67526	70627	18339	0.27
76.4	166098	102098	131879	133358	131879	32026	0.24
69.4	338956	217856	277896	278236	277896	60551	0.22

Fatigue properties of as-welded semi-automatic 5083/ER5356/6061 dissimilar welds in 3.5% NaCl.

NaCl	*Number of cycles to failure, N_f*						
S_a [MPa]	*Test 1*	*Test 2*	*Test 3*	*Mean*	*Median*	*Stdv*	*CV*
111.1	431	189	178	266	189	143	0.54
97.2	1218	611	518	782	611	380	0.49
90.3	3587	1773	2118	2493	2118	963	0.39
83.3	8112	3787	6907	6269	6907	2232	0.36
79.2	18079	8677	15073	13943	15073	4802	0.34
76.4	25975	49107	39801	38294	39801	11639	0.30
69.4	107933	63234	99456	90208	99456	23741	0.26

Fatigue properties of semi-automatic 5083/ER5183 dressed welds in air.

Air	*Number of cycles to failure, N_f*						
S_a [MPA]	*Test 1*	*Test 2*	*Test 3*	*Mean*	*Median*	*Stdv*	*CV*
138.9	1634	612	1265	1170	1265	518	0.44
125.0	5742	2389	4105	4079	4105	1677	0.41
111.1	14801	8331	17987	13706	14801	4920	0.36
97.2	45981	37763	22487	35410	37763	11922	0.34
90.3	102995	81125	54123	79414	81125	24481	0.31
83.3	236867	171456	139758	182694	171456	49520	0.27
79.2	323637	254526	432812	336992	323637	89890	0.27
76.4	488239	662134	805149	651841	662134	158706	0.24
69.4	1225984	1898759	1765820	1630188	1765820	356306	0.22

Fatigue properties of fully automatic 5083/ER5183 dressed welds in air.

Air	*Number of cycles to failure, N_f*						
S_a [MPA]	*Test 1*	*Test 2*	*Test 3*	*Mean*	*Median*	*Stdv*	*CV*
138.9	925	2418	1225	1523	1225	790	0.52
125.0	5058	9302	4124	6161	5058	2760	0.45
111.1	28487	16287	12658	19144	16287	8292	0.43
97.2	31281	42786	67954	47340	42786	18756	0.40
90.3	90395	160734	86231	112453	90395	41864	0.37
83.3	285812	187012	148456	207093	187012	70846	0.34
79.2	243289	461432	370125	358282	370125	109553	0.31
76.4	868738	711842	482548	687709	711842	194223	0.28
69.4	1638573	989268	1701238	1443026	1638573	394213	0.27

Fatigue properties of semi-automatic 5083/ER5183 dressed welds in 3.5% NaCl.

NaCl	*Number of cycles to failure, N_f*						
S_a [MPa]	*Test 1*	*Test 2*	*Test 3*	*Mean*	*Median*	*Stdv*	*CV*
125.0	195	133	333	220	195	102	0.46
111.1	884	589	371	615	589	257	0.42
97.2	2525	1891	1054	1823	1891	738	0.40
90.3	7945	4985	3885	5605	4985	2100	0.37
83.3	16354	8112	11914	12127	11914	4125	0.34
79.2	24856	16587	31523	24322	24856	7482	0.31
76.4	48147	81965	53124	61079	53124	18258	0.30
69.4	157453	98568	172584	142868	157453	39104	0.27

Fatigue properties of fully automatic 5083/ER5183 dressed welds in 3.5% NaCl.

NaCl	*Number of cycles to failure, N_f*						
S_a [MPa]	*Test 1*	*Test 2*	*Test 3*	*Mean*	*Median*	*Stdv*	*CV*
125.0	201	186	401	263	201	120	0.46
111.1	806	1323	585	905	806	379	0.42
97.2	3956	1865	2435	2752	2435	1081	0.39
90.3	8668	4125	6197	6330	6197	2274	0.36
83.3	17456	12456	9285	13066	12456	4119	0.32
79.2	33458	18485	26456	26133	26456	7492	0.29
76.4	43563	75126	57145	58611	57145	15833	0.27
69.4	206231	129453	168526	168070	168526	38391	0.23

Fatigue properties of semi-automatic 6061/ER5183 dressed welds in air.

Air	*Number of cycles to failure, N_f*						
S_a [MPa]	*Test 1*	*Test 2*	*Test 3*	*Mean*	*Median*	*Stdv*	*CV*
111.1	489	314	167	323	314	161	0.50
97.2	1512	598	1081	1064	1081	457	0.43
90.3	3453	2209	1802	2488	2209	860	0.35
83.3	6902	5446	3567	5305	5446	1672	0.32
79.2	9830	12987	17520	13446	12987	3865	0.29
76.4	30288	43874	26897	33686	30288	8984	0.27
69.4	145123	89125	111012	115087	111012	28220	0.25
55.6	509635	374659	324321	402872	374659	95824	0.24

Fatigue properties of fully automatic 6061/ER5183 dressed welds in air.

Air	*Number of cycles to failure, N_f*						
S_a [MPa]	*Test 1*	*Test 2*	*Test 3*	*Mean*	*Median*	*Stdv*	*CV*
138.9	2556	889	1821	1755	1821	835	0.48
125.0	8154	6012	3121	5762	6012	2526	0.44
111.1	19035	16974	7875	14628	16974	5938	0.41
97.2	38427	40987	19978	33131	38427	11462	0.35
90.3	97357	77357	54235	76316	77357	21580	0.28
83.3	214365	148598	128879	163947	148598	44762	0.27
79.2	334623	298123	198923	277223	298123	70223	0.25
76.4	493514	560123	776215	609951	560123	147791	0.24
69.4	1723587	1502149	1078945	1434894	1502149	327541	0.23

Fatigue properties of semi-automatic 6061/ER5183 dressed welds in 3.5% NaCl.

NaCl	*Number of cycles to failure, N_f*						
S_a [MPa]	*Test 1*	*Test 2*	*Test 3*	*Mean*	*Median*	*Stdv*	*CV*
97.2	474	211	189	291	211	159	0.54
90.3	675	342	271	429	342	216	0.50
83.3	1225	571	708	835	708	345	0.41
79.2	1486	985	2153	1541	1486	586	0.38
76.4	3186	2601	4954	3580	3186	1225	0.34
69.4	15325	11035	8554	11638	11035	3426	0.29
55.6	25673	37124	48679	37159	37124	11503	0.31

Fatigue properties of fully automatic 6061/ER5183 dressed welds in 3.5% NaCl.

NaCl	*Number of cycles to failure, N_f*						
S_a [MPa]	*Test 1*	*Test 2*	*Test 3*	*Mean*	*Median*	*Stdv*	*CV*
125.0	93	167	279	180	167	94	0.52
111.1	502	392	189	361	392	159	0.44
97.2	1825	1298	762	1295	1298	532	0.41
90.3	5412	2945	3498	3952	3498	1295	0.33
83.3	9453	7825	14198	10492	9453	3311	0.32
79.2	33254	22253	19425	24977	22253	7306	0.29
76.4	70132	43254	48563	53983	48563	14235	0.26
69.4	162342	236501	156531	185125	162342	44588	0.24

Fatigue properties of semi-automatic 5083/ER5183/6061 dressed welds in air.

Air	*Number of cycles to failure, N_f*						
S_a [MPa]	*Test 1*	*Test 2*	*Test 3*	*Mean*	*Median*	*Stdv*	*CV*
111.1	581	301	247	376	301	179	0.48
97.2	1412	598	951	987	951	408	0.41
90.3	1553	3309	2102	2321	2102	898	0.39
83.3	6502	4746	3087	4778	4746	1708	0.36
79.2	8267	11758	16430	12152	11758	4096	0.34
76.4	38157	20563	26897	28539	26897	8911	0.31
69.4	84124	69368	119125	90872	84124	25556	0.28
55.6	301456	265104	179875	2488127	265104	62406	0.25

Fatigue properties of fully automatic 5083/ER5183/6061 dressed welds in air.

Air	*Number of cycles to failure, N_f*						
S_a [MPa]	*Test 1*	*Test 2*	*Test 3*	*Mean*	*Median*	*Stdv*	*CV*
138.9	791	321	532	548	532	235	0.43
125.0	2981	1392	1736	2036	1736	836	0.41
111.1	9625	4572	6256	6818	6256	2573	0.38
97.2	19153	27124	13145	19807	19153	7012	0.35
90.3	61259	46895	29124	45759	46895	16098	0.35
83.3	153561	89254	101456	114757	101456	34155	0.30
79.2	305130	172997	228256	235461	228256	66361	0.28
76.4	515795	392140	680425	529453	515795	144627	0.27
69.4	1641356	1501238	987897	1376830	1501238	344035	0.25

Fatigue properties of semi-automatic 5083/ER5183/6061 dressed welds in 3.5% NaCl.

NaCl	*Number of cycles to failure, N_f*						
S_a [MPa]	*Test 1*	*Test 2*	*Test 3*	*Mean*	*Median*	*Stdv*	*CV*
97.2	452	202	177	277	202	152	0.55
90.3	589	324	239	384	324	183	0.48
83.3	985	652	415	684	652	286	0.42
79.2	955	2097	1372	1475	1372	578	0.39
76.4	4479	2956	2148	3194	2956	1184	0.37
69.4	14896	9856	7524	10759	9856	3768	0.35
55.6	48975	33248	27356	36526	33248	11176	0.31

Fatigue properties of fully automatic 5083/ER5183/6061 dressed welds in 3.5% NaCl.

NaCl	*Number of cycles to failure, N_f*						
S_a [MPa]	*Test 1*	*Test 2*	*Test 3*	*Mean*	*Median*	*Stdv*	*CV*
111.1	622	279	315	405	315	189	0.47
97.2	896	1101	1965	1321	1101	567	0.43
90.3	3124	2212	4915	3417	3124	1375	0.40
83.3	8649	13298	6925	9624	8649	3296	0.34
79.2	27256	18014	14987	20086	18014	6391	0.32
76.4	52256	41456	28523	40745	41456	11882	0.29
69.4	165268	146234	101356	137619	146234	32815	0.24

Fatigue properties of semi-automatic 5083/ER4043 dressed welds in air.

Air	*Number of cycles to failure, N_f*						
S_a [MPa]	*Test 1*	*Test 2*	*Test 3*	*Mean*	*Median*	*Stdv*	*CV*
125.0	987	615	1698	11000	987	550	0.50
111.1	1789	3101	4625	3172	3101	1419	0.45
97.2	7059	14921	10365	10782	10365	3945	0.37
90.3	35175	17821	21798	24931	21798	9091	0.36
83.3	95593	47821	71712	71709	71712	23886	0.33
79.2	138789	94987	81986	105254	94987	29761	0.28
76.4	272097	194420	162987	209835	194420	56165	0.27
69.4	718692	514012	855356	696020	718692	171798	0.25

Fatigue properties of fully automatic 5083/ER4043 dressed welds in air.

Air	*Number of cycles to failure, N_f*						
S_a [MPa]	*Test 1*	*Test 2*	*Test 3*	*Mean*	*Median*	*Stdv*	*CV*
125.0	2853	1923	872	1883	1923	991	0.53
111.1	7897	2581	5989	5489	5989	2693	0.49
97.2	12491	29879	19879	20750	19879	8727	0.42
90.3	31601	42157	68954	47571	42157	19256	0.40
83.3	76263	98987	158978	111409	98987	42734	0.38
79.2	312456	216898	174015	234456	216898	70871	0.30
76.4	530419	441452	298965	423612	441452	116754	0.28
69.4	1507095	1128265	949987	1195116	1128265	284507	0.24

Fatigue properties of semi-automatic 5083/ER4043 dressed welds in 3.5% NaCl.

NaCl	*Number of cycles to failure, N_f*						
S_a [MPa]	*Test 1*	*Test 2*	*Test 3*	*Mean*	*Median*	*Stdv*	*CV*
125.0	203	315	108	209	203	104	0.50
111.1	989	401	625	672	625	297	0.44
97.2	3359	2021	1365	2248	2021	1016	0.45
90.3	4202	2921	6698	4607	4202	1921	0.42
83.3	6193	8987	13612	9597	8987	3747	0.39
79.2	15263	19125	29886	21425	19125	7578	0.35
76.4	60097	31420	42987	44835	42987	14428	0.32
69.4	138692	214012	128356	160353	138692	46756	0.29

Fatigue properties of fully automatic 5083/ER4043 dressed welds in 3.5% NaCl.

NaCl	*Number of cycles to failure, N_f*						
S_a [MPa]	*Test 1*	*Test 2*	*Test 3*	*Mean*	*Median*	*Stdv*	*CV*
125.0	353	192	124	223	192	118	0.53
111.1	377	614	989	660	614	309	0.47
97.2	3491	2179	1579	2416	2179	978	0.40
90.3	2601	4657	5954	4404	4657	1691	0.38
83.3	17263	10912	8978	12384	10912	4334	0.35
79.2	19456	34898	22015	25456	22015	8276	0.33
76.4	67819	48632	36865	51105	48632	15625	0.31
69.4	184509	152387	101987	146294	152387	41597	0.28

Fatigue properties of semi-automatic 6061/ER4043 dressed welds in air.

Air	*Number of cycles to failure, N_f*						
S_a [MPa]	*Test 1*	*Test 2*	*Test 3*	*Mean*	*Median*	*Stdv*	*CV*
125.0	925	504	1449	959	925	473	0.49
111.1	2156	4986	3348	3497	3348	1421	0.41
97.2	14015	9151	19700	14289	14015	5280	0.37
90.3	31054	27254	50175	36161	31054	12284	0.34
83.3	93213	50125	68214	70517	68214	21636	0.31
79.2	95789	172103	141258	136383	141258	38390	0.28
76.4	202486	289318	357356	283053	289318	77625	0.27
69.4	952592	862013	1301598	1038734	952592	232108	0.22

Fatigue properties of fully automatic 6061/ER4043 dressed welds in air.

Air	*Number of cycles to failure, N_f*						
S_a [MPa]	*Test 1*	*Test 2*	*Test 3*	*Mean*	*Median*	*Stdv*	*CV*
125.0	1695	813	1209	1239	1209	442	0.36
111.1	2978	4156	6011	4382	4156	1529	0.35
97.2	19046	16002	9985	15011	16002	4611	0.31
90.3	53573	28920	43968	42154	43968	12426	0.29
83.3	98987	74546	128869	100801	98987	27207	0.27
79.2	310035	211548	191002	237528	211548	63627	0.27
76.4	378078	496201	599201	491160	496201	110648	0.23
69.4	1415383	897123	1255383	1189296	1255383	265375	0.22

Fatigue properties of semi-automatic 6061/ER4043 dressed welds in 3.5% NaCl.

NaCl	*Number of cycles to failure, N_f*						
S_a [MPa]	*Test 1*	*Test 2*	*Test 3*	*Mean*	*Median*	*Stdv*	*CV*
125.0	145	274	97	172	145	92	0.53
111.1	285	166	488	313	285	163	0.52
97.2	1415	511	872	933	872	455	0.49
90.3	954	1754	2675	1794	1754	861	0.48
83.3	5213	1825	3836	3625	3836	1704	0.47
79.2	8178	12503	19928	13536	12503	5943	0.44
76.4	25234	19318	44356	29636	25234	13087	0.44
69.4	82592	70268	31598	61486	70268	26607	0.43

Fatigue properties of fully automatic 6061/ER4043 dressed welds in 3.5% NaCl.

NaCl	*Number of cycles to failure, N_f*						
S_a [MPa]	*Test 1*	*Test 2*	*Test 3*	*Mean*	*Median*	*Std*	*CV*
125.0	345	223	589	386	345	186	0.48
111.1	748	1156	501	802	748	331	0.41
97.2	2246	1902	3786	2645	2246	1003	0.38
90.3	6157	4890	2868	4638	4890	1659	0.36
83.3	7887	15246	10188	11107	10188	3765	0.34
79.2	32203	22605	17105	23971	22605	7641	0.32
76.4	37812	46862	66923	50532	46862	14899	0.29
69.4	167894	148763	98123	138260	148763	36052	0.26

Fatigue properties of semi-automatic 5083/ER4043/6061 dressed welds in air.

Air	*Number of cycles to failure, N_f*						
S_a [MPa]	*Test 1*	*Test 2*	*Test 3*	*Mean*	*Median*	*Stdv*	*CV*
125.0	611	401	1356	789	611	502	0.64
111.1	1095	3875	2017	2329	2017	1416	0.61
97.2	4021	6342	12837	7733	6342	4570	0.59
90.3	18265	38098	12645	23003	18265	13372	0.58
83.3	27076	39538	78098	48237	39538	26600	0.55
79.2	45439	141653	81231	89441	81231	48630	0.54
76.4	149284	275354	98235	174291	149284	91169	0.52
69.4	243563	348858	631264	407895	348858	20080	0.49

Fatigue properties of fully automatic 5083/ER4043/6061 dressed welds in air.

Air	*Number of cycles to failure, N_f*						
S_a [MPa]	*Test 1*	*Test 2*	*Test 3*	*Mean*	*Median*	*Std*	*CV*
125.0	1775	735	968	1159	968	546	0.47
111.1	1978	3129	4982	3363	3129	1516	0.45
97.2	19046	10875	8735	12885	10875	5442	0.42
90.3	33632	14238	22534	23468	22534	9731	0.41
83.3	58124	49639	25356	44373	49639	17007	0.38
79.2	119264	93172	191002	134479	119264	50659	0.38
76.4	152876	258721	323875	245157	258721	86303	0.35
69.4	762098	423987	876498	687528	762098	235292	0.34

Fatigue properties of semi-automatic 5083/ER4043/6061 dressed welds in 3.5% NaCl.

NaCl	*Number of cycles to failure, N_f*						
S_a [MPa]	*Test 1*	*Test 2*	*Test 3*	*Mean*	*Median*	*Stdv*	*CV*
125.0	71	98	201	123	98	69	0.56
111.1	385	247	108	247	247	139	0.56
97.2	1315	471	626	804	626	449	0.56
90.3	954	1454	2775	1728	1454	941	0.54
83.3	6813	3016	2836	4222	3016	2246	0.53
79.2	9138	6589	2693	6140	6589	3246	0.53
76.4	10876	14188	27836	17633	14188	8990	0.51
69.4	64026	41024	21686	42245	41024	21196	0.50

Fatigue properties of fully automatic 5083/ER4043/6061 dressed welds in 3.5% NaCl.

NaCl	*Number of cycles to failure, N_f*						
S_a [MPA]	*Test 1*	*Test 2*	*Test 3*	*Mean*	*Median*	*Stdv*	*CV*
125.0	345	223	589	386	345	186	0.48
111.1	748	1156	501	802	748	331	0.41
97.2	2246	1902	3786	2645	2246	1003	0.38
90.3	6157	4890	2868	4638	4890	1659	0.36
83.3	7887	15246	10188	11107	10188	3765	0.34
79.2	32203	22605	17105	23971	22605	7641	0.32
76.4	37812	46862	66923	50532	46862	14899	0.29
69.4	167894	148763	98123	138260	148763	36052	0.26

APPENDIX III. Fatigue damage ratio values.

Fatigue damage ratio of as-received 5083-H111 in 3.5% NaCl.

Fatigue damage ratio ($N_{f\ NaCl}/N_{f\ air}$)			
S_a [MPa]	$N_{f\ Air}$	$N_{f\ NaCl}$	$N_{f\ NaCl}/N_{f\ Air}$
138.9	91123	11254	0.12
125.0	188484	30646	0.16
111.1	387529	81254	0.21
97.2	585725	158214	0.27
90.3	930235	331356	0.36
83.3	1923548	712859	0.37

Fatigue damage ratio of as-received 6061-T651 in 3.5% NaCl.

Fatigue damage ratio ($N_{f\ NaCl}/N_{f\ air}$)			
S_a [MPa]	$N_{f\ Air}$	$N_{f\ NaCl}$	$N_{f\ NaCl}/N_{f\ Air}$
138.9	47365	2054	0.04
125.0	96712	7887	0.08
111.1	165815	20069	0.12
97.2	398256	57325	0.14
90.3	908400	142958	0.16
83.3	1796000	379872	0.21

Fatigue damage ratio of semi-automatic 5083/ER5356 dressed welds in 3.5% NaCl.

Fatigue damage ratio ($N_{f\ NaCl}/N_{f\ air}$)			
S_a [MPa]	$N_{f\ Air}$	$N_{f\ NaCl}$	$N_{f\ NaCl}/N_{f\ Air}$
111.1	1241	411	0.33
97.2	4325	1127	0.26
90.3	9846	2184	0.22
83.3	20984	4576	0.22
79.2	61132	9729	0.16
76.4	129658	21685	0.17
69.4	335807	84296	0.25

Fatigue damage ratio of fully automatic 5083/ER5356 dressed welds in 3.5% NaCl.

Fatigue damage ratio ($N_{f\ NaCl}/N_{f\ air}$)			
S_a [MPa]	$N_{f\ Air}$	$N_{f\ NaCl}$	$N_{f\ NaCl}/N_{f\ Air}$
111.1	2908	604	0.21
97.2	10985	1985	0.18
90.3	30945	4602	0.15
83.3	119826	16996	0.14
79.2	316337	34876	0.11
76.4	658550	72139	0.11
69.4	1823501	229879	0.13

Fatigue damage ratio of semi-automatic 6061/ER5356 dressed welds in 3.5% NaCl.

Fatigue damage ratio ($N_{f\ NaCl}/N_{f\ air}$)			
S_a [MPa]	$N_{f\ Air}$	$N_{f\ NaCl}$	$N_{f\ NaCl}/N_{f\ Air}$
111.1	1029	311	0.30
97.2	3292	817	0.25
90.3	10927	2365	0.22
83.3	34895	7931	0.23
79.2	72498	16519	0.23
76.4	141365	31754	0.22
69.4	287915	103986	0.36

Fatigue damage ratio of fully automatic 6061/ER5356 dressed welds in 3.5% NaCl.

Fatigue damage ratio ($N_{f\ NaCl}/N_{f\ air}$)			
S_a *[MPa]*	$N_{f\ Air}$	$N_{f\ NaCl}$	$N_{f\ NaCl}/N_{f\ Air}$
111.11	1107	333	0.30
97.22	3298	942	0.29
90.28	12764	2904	0.23
83.33	35654	8189	0.23
79.17	78395	18943	0.24
76.39	166438	42775	0.26
69.44	294156	108456	0.37

Fatigue damage ratio of semi-automatic 5083/ER5356/6061 dressed welds in 3.5% NaCl.

Fatigue damage ratio ($N_{f\ NaCl}/N_{f\ air}$)			
S_a *[MPa]*	$N_{f\ Air}$	$N_{f\ NaCl}$	$N_{f\ NaCl}/N_{f\ Air}$
111.1	1498	351	0.23
97.2	5174	996	0.19
90.3	10786	2018	0.19
83.3	22176	4407	0.20
79.2	46117	9173	0.20
76.4	97879	22801	0.23
69.4	277896	89456	0.32

Fatigue damage ratio of fully automatic 5083/ER5356/6061 dressed welds in 3.5% NaCl.

Fatigue damage ratio ($N_{f\ NaCl}/N_{f\ air}$)			
S_a *[MPa]*	$N_{f\ Air}$	$N_{f\ NaCl}$	$N_{f\ NaCl}/N_{f\ Air}$
111.1	2189	746	0.34
97.2	6853	2181	0.32
90.3	14022	5018	0.36
83.3	29874	11337	0.38
79.2	65621	24879	0.38
76.4	134879	52801	0.39
69.4	434786	168364	0.39

Fatigue damage ratio of semi-automatic 5083/ER5183 dressed welds in 3.5% NaCl.

Fatigue damage ratio ($N_{f\ NaCl}/N_{f\ air}$)			
S_a *[MPa]*	$N_{f\ Air}$	$N_{f\ NaCl}$	$N_{f\ NaCl}/N_{f\ Air}$
125.0	4105	195	0.05
111.1	14801	589	0.04
97.2	37763	1891	0.05
90.3	81125	4985	0.06
83.3	171456	11914	0.07
79.2	323637	24856	0.08
76.4	662134	53124	0.08
69.4	1765820	157453	0.09

Fatigue damage ratio of fully automatic 5083/ER5183 dressed welds in 3.5% NaCl.

Fatigue damage ratio ($N_{f\ NaCl}/N_{f\ air}$)			
S_a *[MPa]*	$N_{f\ Air}$	$N_{f\ NaCl}$	$N_{f\ NaCl}/N_{f\ Air}$
125.0	5058	201	0.04
111.1	16287	806	0.05
97.2	42786	2435	0.06
90.3	90395	6197	0.07
83.3	187012	12456	0.07
79.2	370125	26456	0.07
76.4	711842	57145	0.08
69.4	1638573	168526	0.10

Fatigue damage ratio of semi-automatic 6061/ER5183 dressed welds in 3.5% NaCl.

Fatigue damage ratio ($N_{f\ NaCl}/N_{f\ air}$)			
S_a *[MPa]*	$N_{f\ Air}$	$N_{f\ NaCl}$	$N_{f\ NaCl}/N_{f\ Air}$
97.2	1081	211	0.20
90.3	2209	342	0.15
83.3	5446	708	0.13
79.2	12987	1486	0.11
76.4	30288	3186	0.11
69.4	111012	11035	0.10
55.6	374659	37124	0.10

Fatigue damage ratio of fully automatic 6061/ER5183 dressed welds in 3.5% NaCl.

Fatigue damage ratio ($N_{f\ NaCl}/N_{f\ air}$)			
S_a *[MPa]*	$N_{f\ Air}$	$N_{f\ NaCl}$	$N_{f\ NaCl}/N_{f\ Air}$
125.0	6012	167	0.03
111.1	16974	392	0.02
97.2	38427	1298	0.03
90.3	77357	3498	0.05
83.3	148598	9453	0.06
79.2	298123	22253	0.07
76.4	560123	48563	0.09
69.4	1502149	162342	0.11

Fatigue damage ratio of semi-automatic 5083/ER5183/6061 dressed welds in 3.5% NaCl.

Fatigue damage ratio ($N_{f\ NaCl}/N_{f\ air}$)			
S_a *[MPa]*	$N_{f\ Air}$	$N_{f\ NaCl}$	$N_{f\ NaCl}/N_{f\ Air}$
97.2	951	202	0.21
90.3	2102	324	0.15
83.3	4746	652	0.14
79.2	11758	1372	0.12
76.4	26897	2956	0.11
69.4	84124	9856	0.12
55.6	265104	33248	0.13

Fatigue damage ratio of fully automatic 5083/ER5183/6061 dressed welds in 3.5% NaCl.

Fatigue damage ratio ($N_{f\ NaCl}/N_{f\ air}$)			
S_a *[MPa]*	$N_{f\ Air}$	$N_{f\ NaCl}$	$N_{f\ NaCl}/N_{f\ Air}$
111.1	6256	315	0.05
97.2	19153	1101	0.06
90.3	46895	3124	0.07
83.3	101456	8649	0.09
79.2	228256	18014	0.08
76.4	515795	41456	0.08
69.4	1501238	146234	0.10

Fatigue damage ratio of semi-automatic 5083/ER4043 dressed welds in 3.5% NaCl.

Fatigue damage ratio ($N_{f\ NaCl}/N_{f\ air}$)			
S_a *[MPa]*	$N_{f\ Air}$	$N_{f\ NaCl}$	$N_{f\ NaCl}/N_{f\ Air}$
125.0	987	203	0.21
111.1	3101	625	0.20
97.2	10365	2021	0.19
90.3	21798	4202	0.19
83.3	71712	8987	0.13
79.2	94987	19125	0.20
76.4	194420	42987	0.22
69.4	718692	138692	0.19

Fatigue damage ratio of fully automatic 5083/ER4043 dressed welds in 3.5% NaCl.

Fatigue damage ratio ($N_{f\ NaCl}/N_{f\ air}$)			
S_a *[MPa]*	$N_{f\ Air}$	$N_{f\ NaCl}$	$N_{f\ NaCl}/N_{f\ Air}$
125.0	1923	192	0.10
111.1	5989	614	0.10
97.2	19879	2179	0.11
90.3	42157	4657	0.11
83.3	98987	10912	0.11
79.2	216898	22015	0.10
76.4	441452	48632	0.11
69.4	1128265	152387	0.14

Fatigue damage ratio of semi-automatic 6061/ER4043 dressed welds in 3.5% NaCl.

Fatigue damage ratio ($N_{f\ NaCl}/N_{f\ air}$)			
S_a *[MPa]*	$N_{f\ Air}$	$N_{f\ NaCl}$	$N_{f\ NaCl}/N_{f\ Air}$
125.0	925	145	0.16
111.1	3348	285	0.09
97.2	14015	872	0.06
90.3	31054	1754	0.06
83.3	68214	3836	0.06
79.2	141258	12503	0.09
76.4	289318	25234	0.09
69.4	952592	70268	0.07

Fatigue damage ratio of fully automatic 6061/ER4043 dressed welds in 3.5% NaCl.

Fatigue damage ratio ($N_{f\ NaCl}/N_{f\ air}$)			
S_a [MPa]	*$N_{f\ Air}$*	*$N_{f\ NaCl}$*	*$N_{f\ NaCl}/N_{f\ Air}$*
125.0	1209	345	0.29
111.1	4156	748	0.18
97.2	16002	2246	0.14
90.3	43968	4890	0.11
83.3	98987	10188	0.10
79.2	211548	22605	0.11
76.4	496201	46862	0.09
69.4	1255383	148763	0.12

Fatigue damage ratio of semi-automatic 5083/ER4043/6061 dressed welds in 3.5% NaCl.

Fatigue damage ratio ($N_{f\ NaCl}/N_{f\ air}$)			
S_a [MPa]	*$N_{f\ Air}$*	*$N_{f\ NaCl}$*	*$N_{f\ NaCl}/N_{f\ Air}$*
125.0	611	98	0.16
111.1	2017	247	0.12
97.2	6342	626	0.10
90.3	18265	1454	0.08
83.3	39538	3016	0.08
79.2	81231	6589	0.08
76.4	149284	14188	0.10
69.4	348858	41024	0.12

Fatigue damage ratio of fully automatic 5083/ER4043/6061 dressed welds in 3.5% NaCl.

Fatigue damage ratio ($N_{f\ NaCl}/N_{f\ air}$)			
S_a [MPa]	*$N_{f\ Air}$*	*$N_{f\ NaCl}$*	*$N_{f\ NaCl}/N_{f\ Air}$*
125.00	1209	345	0.29
111.11	4156	748	0.18
97.22	16002	2246	0.14
90.28	43968	4890	0.11
83.33	98987	10188	0.10
79.17	211548	22605	0.11
76.39	496201	46862	0.09
69.44	1255383	148763	0.12